Using Antiferromagnetic Co_3O_4 Shapes and Ferrimagnetic $Cu_xCo_{3-x}O_4$ to Quantify Broken and Modified Exchange Interactions at the Surface and Core of Nanoparticles

by

Michael Melvin Joseph Shepit

A thesis submitted to
The Faculty of Graduate Studies of
The University of Manitoba
in partial fulfillment of the requirements
of the degree of

Master of Science

Department of Department of Physics and Astronomy
The University of Manitoba
Winnipeg, Manitoba, Canada
June 2020

Thesis advisor

Dr. Johan van Lierop

Author

Michael Melvin Joseph Shepit

Using Antiferromagnetic Co_3O_4 Shapes and Ferrimagnetic $Cu_xCo_{3-x}O_4$ to Quantify Broken and Modified Exchange Interactions at the Surface and Core of Nanoparticles

Abstract

Nanoparticles are widely studied systems for a variety of applications; however, as the surface plays the major role in deciding the overall properties, characterization of the surface becomes as important as the characterization of the structure itself. The underlying physics regarding exchange interactions and bonding can be elucidated by studying the structure of the surface and core. Doping allows us to change the overall spin arrangement, and investigate the competition between ferro- and antiferromagnetic interactions.

To undertake a rigorous characterization of exchange interactions at the surface and in the core of nanoparticles, I utilize different shapes of Co_3O_4 and dopings of $Cu_xCo_{3-x}O_4$ nanoparticles. The antiferromagnetic arrangement of Co_3O_4 is ideal for studying changes in the magnetism. Due to the competition of ferro- and antiferromagnetic interactions small changes in the exchange can result in large changes in the magnetism.

By studying the shapes in the context of the exposed surface planes, differences in the structure of the surface terminations can be correlated to the exchange in-

teractions leading to quantification of the surface exchange and magnetism. On the other hand, by doping Cu into the structure of Co_3O_4 we can examine the affects that modify the exchange interactions in the core of the particle. The role of Cu becomes extremely important to the exchange interactions creating ligand holes between magnetic ions, facilitating ferromagnetic exchange between the ions. The different shapes, and Cu-doping, allow us to explore the relations between the exchange interactions and the overall magnetism in nanoparticles, where the surface is shown to be directly responsible for differences to the bulk magnetism.

Contents

List of Figures

List of Tables

Acknowledgments

First, I would like to thank my supervisor, Dr. Johan van Lierop, for his support throughout this work. His guidance has been paramount to my growth as a researcher, and the success of this project. It has been very rewarding to have the opportunity to work and participate in many different fields of research under such an esteemed researcher in the condensed matter field.

I would like to give a special thanks to Dr. Vinod Paidi for the invaluable discussions we've had, and who has endured my many questions as a student. Without you I would not be here today (I'd be with the other students, stuffed in a beamline). I would also like to give a special thanks to Dr. Peiqing Wang for his continued assistance and patience with anything and everything inside our lab. I would like to thank all present (and past) members of the nanomagnetism research group (NRG) for the discussions, good times, and doing measurements for me, as well as the support staff for the Department of Physics and Astronomy; Wanda Klassen, Susan Beshta, Robyn Beaulieu, Aymsley Bishop-Mahon, and Maiko Langelaar.

Thanks to the folks at Toyota, Dr. Charles Roberts and Dr. Gunugunuri Reddy for supplying the copper doped nanoparticles that were used for characterization. I would like to thank both Dr. Abdul Kahn from Manitoba Institute for Materials (MIM) and colleague Rachel Nickel from NRG for electron microscopy measurements. Many thanks to APS beamline staff for technical support in XAS measurements; Dr. John Freeland, Dr. David Keavney, and Dr. Dale Brewe.

Finally I would like to thank my girlfriend Gabrielle Fontaine and the rest of my friends and family, who have been incredibly supportive and patient with me in completing this degree.

To my father,
A man with no education but much to teach.

Chapter 1

Introduction

In general, magnetic nanoparticles are a much more complicated system compared to their bulk counterparts. Due to the small size of nanoparicles, the surface plays a very important role in the resulting behaviour. Finite size effects including broken symmetry, vacancies, and disorder result in changes to the exchange interactions and bonding properties thus affecting behaviour such as the magnetism[4; 5]. Nanoparticles of materials such as Co_3O_4 and $Cu_xCo_{3-x}O_4$ have been exploited for many applications in areas including sensors[6; 7], anode material in LiO_2 batteries[8–10], and many catalytic reactions with NO_x and N_2O decomposition[11; 12] and oxidation of methanol[13].

The first row transition metal ions can form oxide compounds that present a range of magnetic behaviour due to the intrinsic nature of the $3d$ orbitals which are not screened by other orbitals such as the $4f$ series where the electrons are highly localized[14]. Transition metal oxides such as cobalt oxide (Co_3O_4) are readily available and can produce a wide range of distinct magnetic order due to the large sponta-

neous magnetic moments created as a result of the exchange interactions. Exchange interactions occur through pairing and hopping of electrons between electron orbitals causing a correlation between the magnetic moments. Further, for oxide compounds magnetism is usually a result of magnetic exchange interactions that occur through intermediate oxygen ions (superexchange), allowing for complex magnetic behaviour.

In this work, the magnetic properties that result from the surface will be examined in the context of the possible surface exchange interactions of different shapes of Co_3O_4 nanoparticles. The shapes expose different surface terminations and by characterizing the structural properties of the terminations we can gain insight into the overall magnetic properties. We can show that the differences in the magnetic properties for the samples are a direct result of the exchange interactions present at the surface. This fundamental result proves the importance of the surface and allows for quantification of the surface properties when considering nanoparticles.

Further, we also examine the affect of doping Cu into the structure of Co_3O_4 and revisit the exchange interactions. Cu provides a great way to examine the dominant ferromagnetic interactions that occur in $Cu_xCo_{3-x}O_4$ that result in strange ferromagnetic order for certain Cu sites. Non-magnetic Co^{3+} ions inhabit all the octahedral (O_h) sites in Co_3O_4. This results in a magnetic structure that relies heavily on exchange interactions through many ions and this makes it an ideal candidate to study the magnetic order of spinel structures and extended exchange interactions at the nanoscale. From this research we gain new insight into the interactions that result in different surface magnetism for nanoparticles along with the resultant magnetic properties that occur from doping.

1.1 Bulk Magnetism

1.1.1 Paramagnetism

Paramagnetism occurs in materials with non-interacting or isolated magnetic moments. In an applied magnetic field the magnetic moments of a paramagnet align with the field as shown in figure 1.1. Without an applied magnetic field the overall magnetization M of a paramagnet is zero due to the average of the spins across the material. The magnetic moment of an ion is represented using the total angular momentum $\mathbf{j} = \mathbf{l} + \mathbf{s}$ where $\mathbf{j}$ can be represented as $\mathbf{j} = j\hbar$, with $\mathbf{l}$ and $\mathbf{s}$ as the orbital and spin angular momenta, respectively. For a spin-$\frac{1}{2}$ system with $\mathbf{l} = 0$, $\mathbf{j} = \frac{1}{2}\hbar$ and the associated magnetic moment m is related to the z-component of the allowed j values $m_j = \pm\frac{1}{2}$:

$$m = g_j \mu_B m_j = \pm\mu_B \tag{1.1}$$

where $\mu_B = \frac{e\hbar}{2m_e}$ is the Bohr magneton ($\hbar$ has been absorbed into μ_B by convention) and g_j is the Landé g-factor related to the magnetic moment of the ion under consideration ($g_j = g = 2$ for spin-$\frac{1}{2}$). For an isolated ($s = 1/2$) magnetic moment inside a magnetic field $\mathbf{B}$, the energy is obtained as a scalar product between the moment and field:

$$E_m = \mathbf{B} \cdot \mathbf{m} = \pm\mu_B B \tag{1.2}$$

where + (-) signifies the spin pointing in the same (opposite) direction as the magnetic field. We are concerned with the thermal average of the magnetic moments $\langle m \rangle$ in a magnetic field. For a large collection (10^{23}) of moments the average can be obtained using statistical mechanics. Assuming the non-interacting nature of a paramagnetic

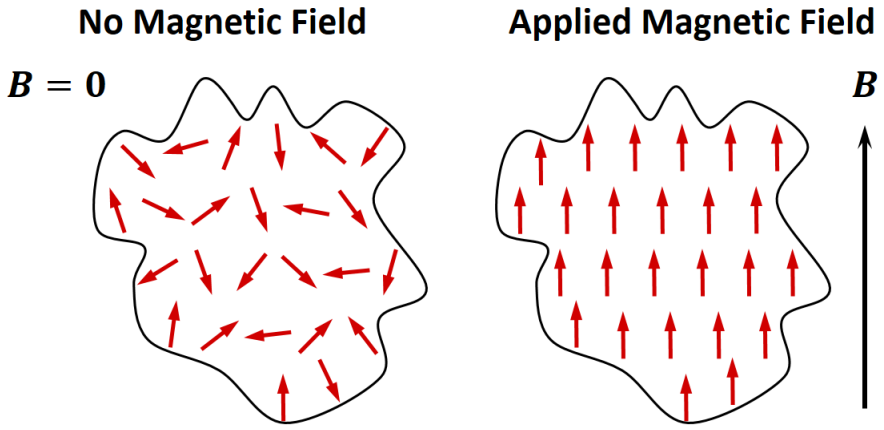

Figure 1.1: Illustration of a paramagnetic compound inside and outside of an applied magnetic field.

solid with the ions trapped in a lattice, we can begin with the partition function for the canonical ensemble given by:

$$Z = \sum_i \exp\left(\frac{-E_i}{k_B T}\right) \tag{1.3}$$

Where k_B is the Boltzmann constant, T is temperature, and E_i is the energy of state i. E_i is directly related to the energy (E_{m_j}) of a magnetic moment in angular momentum state j and the sum in equation 1.3 is over the possible values of j-states (m_j):

$$Z = \sum_j \exp\left(\frac{-E_{m_j}}{k_B T}\right) = \sum_{m_j=-j}^{j} \exp\left(\frac{m_j g_j \mu_B B}{k_B T}\right) \tag{1.4}$$

If we write $x = g_j \mu_B B / k_B T$ the thermal average of $\langle m_j \rangle$ can be written as:

$$\langle m_j \rangle = \frac{\sum_{-j}^{j} m_j e^{m_j x}}{\sum_{-j}^{j} e^{m_j x}} = \frac{1}{Z}\frac{\partial Z}{\partial x} \tag{1.5}$$

The overall magnetization is then obtained by $M = n \langle m \rangle$ where $n = N/V$ is the number of magnetic moments per unit volume V:

$$M = \frac{n g_j \mu_B}{Z}\frac{\partial Z}{\partial B}\frac{\partial B}{\partial x} = n k_B T \frac{\partial \ln Z}{\partial B} \tag{1.6}$$

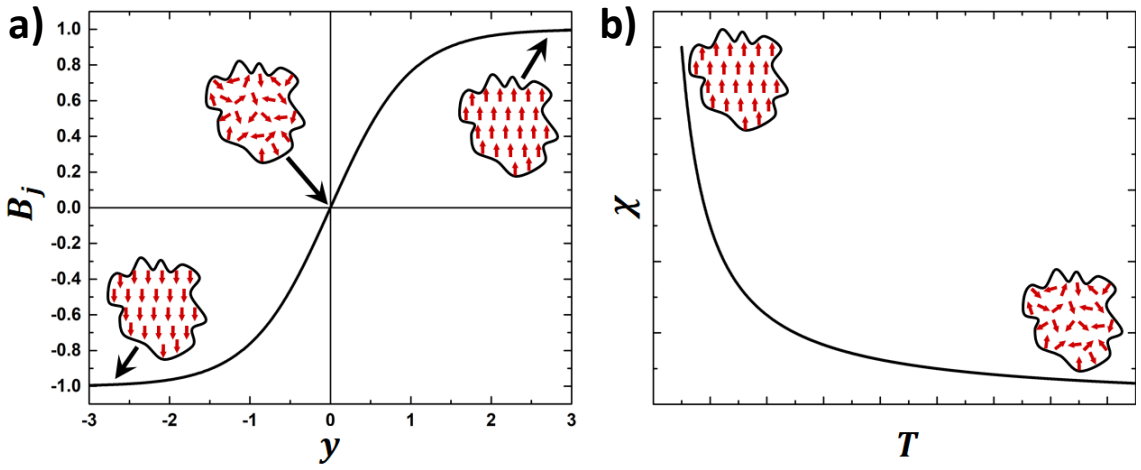

Figure 1.2: a) Plot of the Brillouin function $B_j(y)$, showing the spin alignment as the field changes. b) Susceptibility $\chi(T)$ of a paramagnet.

From above, the partition function is written in terms of a geometric progression series with a known solution:

$$Z = e^{-jx} + e^{-jx}e^{x} + e^{-jx}e^{2x} + \cdots + e^{-jx}e^{(2j+1)x} = \frac{e^{-jx}(1 - e^{(2j+1)x})}{1 - e^{x}} \tag{1.7}$$

Which is easily expressed using hyperbolic sine functions:

$$Z = \frac{\sinh\left[(2j+1)\frac{x}{2}\right]}{\sinh\left[\frac{x}{2}\right]} \tag{1.8}$$

Finally, we can express the overall magnetization M using the well known Brillouin function $B_j(y)$:

$$\frac{M}{M_s} = B_j(y) = \frac{2j+1}{2j}\coth\left(\frac{2j+1}{2J}y\right) - \frac{1}{2j}\coth\frac{y}{2j} \tag{1.9}$$

with substitutions $M_s = ng_j\mu_B j$ and $y = xj = g_j\mu_B jB/k_BT$. With no applied magnetic field ($y = 0$) the magnetic moments are disordered (figure 1.2). As the applied field increases, saturation occurs when all of the moments are aligned with the field $M = M_s$. A linear region can be identified in the region of $|y| \leq 0.5$. Typical

values for y at room temperature are in the range of 2×10^{-3}. Thus, except for the cases of very low temperature and very large magnetic fields $y \ll 1$ and we can expand equation 1.9 using a Taylor series about $y = 0$ so that equation 1.9 becomes:

$$\frac{M}{M_s} \approx \frac{(j+1)y}{3j} = \frac{g_j \mu_B (j+1) B}{3 k_B T} \tag{1.10}$$

and the susceptibility χ is given by:

$$\chi = \frac{M}{H} \approx \frac{\mu_0 M}{B} = \frac{C}{T} \tag{1.11}$$

where $C = n\mu_0 \mu_{eff}^2 / 3k_B$ is known as the Curie constant, μ_{eff} is the effective magnetic moment, and the approximation $B = \mu_0(H+M) \approx \mu_0 H$ was used relating to the small magnetization present in paramagnetic compounds[15]. Equation 1.11 describes the temperature dependence of the susceptibility $\chi(T)$ of a paramagnetic compound and is known as Curie's law. The susceptibility of a paramagnet are shown in figure 1.2. Inside a magnetic field the magnetic moments at high temperature are disordered, but as temperature is decreased they begin to align with the magnetic field causing the large increase in χ at low temperatures. This equation has the typical $1/T$ dependence of paramagnetic ions and is the background for the more useful Curie-Weiss law used to describe magnetic order such as ferromagnetism, antiferromagnetism, and ferrimagnetism in section 1.1.2.

The effective magnetic moment describes the overall magnetic moment per formula unit in the sample:

$$\mu_{eff} = g_j \mu_B \sqrt{j(j+1)} \tag{1.12}$$

and g_j is given by:

$$g_j = \frac{3}{2} + \frac{s(s+1) - l(l+1)}{2j(j+1)} \tag{1.13}$$

A second paramagnetic susceptibility term can arise under the case of a non-degenerate ground state $|0\rangle$ i.e. singlet state with energy E_0 that occurs with excited states $\langle n|$ with energy E_n that lie above the ground state energy such that the energy difference $(E_n - E_0 > 0)$ is positive. This susceptibility is known as van Vleck paramagnetism χ_0 described by[16]:

$$\chi_0 = \frac{2\mu_0\mu_B^2}{V}\sum_n \frac{\left|\langle 0|\left(\mathbf{l}_z + g\mathbf{s}_z\right)|n\rangle\right|^2}{E_n - E_0} \tag{1.14}$$

where the $\mathbf{l}_z$ ($\mathbf{s}_z$) are the orbital (spin) angular momentum z operators. χ_0 is a positive, typically temperature independent, quantity with values in the range of 6×10^{-5} m^3/mol-T for most individual $3d^n$ ion per unit cell[17–19]. Crystal fields in magnetic solids tend to form degenerate ground states for the $3d^n$ ions, and since only a non-degenerate ground state applies, only a few of the $3d$ electronic structures ($3d^n$ configurations) can give a van Vleck paramagnetism.

1.1.2 Magnetic Order

With the foundation of the paramagnetic susceptibilities in the previous section we can review the bulk magnetic order that occur in some solids as a result of local magnetic interactions between spins. Magnetic interactions can form three different structures: i) a ferromagnet, in which all the spins are aligned below the Curie temperature T_C; ii) an antiferromagnet, which contains two magnetic sublattices oppositely oriented to provide cancellation of the net magnetic moment below the Néel temperature T_N; and iii) ferrimagnetic, which usually results from ferro- and antiferromagnetic interactions in two oppositely oriented magnetic lattices, that do not fully compensate one another (in magnitude or number of spins). All three structures

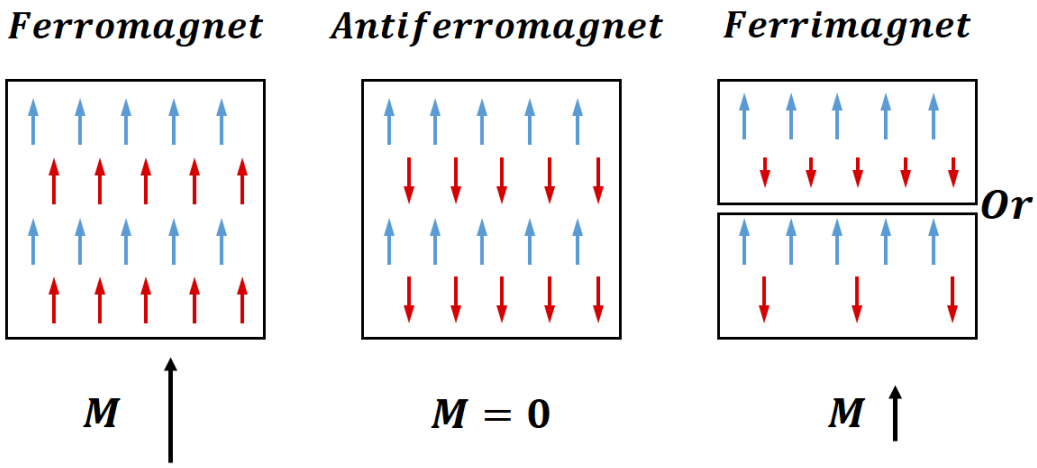

Figure 1.3: Representation of ferro-, antiferro-, and ferrimagnetic structures, showing their overall magnetization M.

are shown schematically in figure 1.3. The temperatures T_C and T_N define the maximum temperature with which the magnetic order occurs in the material. Above this temperature a material loses magnetic order and become paramagnetic.

Magnetic interactions can form different behaviour based on the intrinsic properties of the crystal structure, symmetry, and occupation of the electron orbitals. For a ferromagnetic material inside an applied magnetic field B we can write the Hamiltonian as:

$$\mathcal{H} = \mathcal{H}_{ex} + \mathcal{H}_{mag} = -\frac{1}{2}\sum_{ij} J_{ij}\mathbf{s}_i \cdot \mathbf{s}_j + g\mu_B \sum_i \mathbf{s}_i \cdot \mathbf{B} \tag{1.15}$$

where i and j are integers of individual spins throughout the material and $\mathcal{H}_{mag} = g\mu_B \sum_i \mathbf{s}_i \cdot \mathbf{B}$ is the Hamiltonian for the paramagnetic material that leads to Curie's law, where we have set $\mathbf{l} = 0$ so that $\mathbf{j} = \mathbf{s}$. The term $\mathcal{H}_{ex} = -\frac{1}{2}\sum_{ij} J_{ij}\mathbf{s}_i \cdot \mathbf{s}_j$ is known as Heisenberg's exchange Hamiltonian[15]. The exchange constant J_{ij} (or exchange integral) describes the type of magnetic interactions occurring between spins $\mathbf{s}_i$ and

$\mathbf{s}_j$. For a given site i we can rewrite $\mathcal{H}_{ex}$ as:

$$\mathcal{H}_{ex,i} = -\mathbf{s}_i \cdot \sum_j J_{ij}\mathbf{s}_j = g\mu_B \mathbf{s}_i \cdot \mathbf{B}_{mf} \tag{1.16}$$

where we have introduced the effective molecular field $\mathbf{B}_{mf} = -\frac{1}{g\mu_B}\sum_j J_{ij}\mathbf{s}_j$ caused by all of the interactions between $\mathbf{s}_i$ and neighbouring $\mathbf{s}_j$ spins. Thus we can write the Hamiltonian of equation 1.15 as:

$$\mathcal{H} = g\mu_B \sum_i \mathbf{s}_i \cdot (\mathbf{B} + \mathbf{B}_{mf}) \tag{1.17}$$

This resembles $\mathcal{H}_{mag}$ of the paramagnetic case, but with a combined effective magnetic field $\mathbf{B}+\mathbf{B}_{mf}$. Returning to the Brillouin function, $B_j(y)$, of equation 1.9 and defining a new y given by:

$$\frac{M}{M_s} = B_j(y) \ , \quad y = \frac{g_j\mu_B j(B + \lambda M)}{k_B T} \tag{1.18}$$

where $\mathbf{B}_{mf} = \lambda\mathbf{M}$ and λ parameterizes the strength of the molecular field as a function of the magnetization, and we have returned to $l \neq 0$ (with $s \to j$ and $g \to g_j$). The above theory is known as the Weiss model of ferromagnetism. For a ferromagnetic exchange J_{ij} , $\lambda > 0$ tend to align the neighbouring moments parallel to one another. An illustration of the molecular field caused by the neighbouring spins is shown in figure 1.4. Including only z nearest neighbour ions in the summation over j for the molecular field (each with equal exchange strength J_{ij}) we find a relation between J_{ij} and λ:

$$\lambda = \frac{2zJ_{ij}}{ng_j^2\mu_B^2} \tag{1.19}$$

since J_{ij} is the origin of the molecular field λM.

Examining equation 1.18 when $T < T_C$, we find there are three solutions; the same trivial $M = 0$ solution and two solutions $M = \pm M_s$. Thus an induced spontaneous

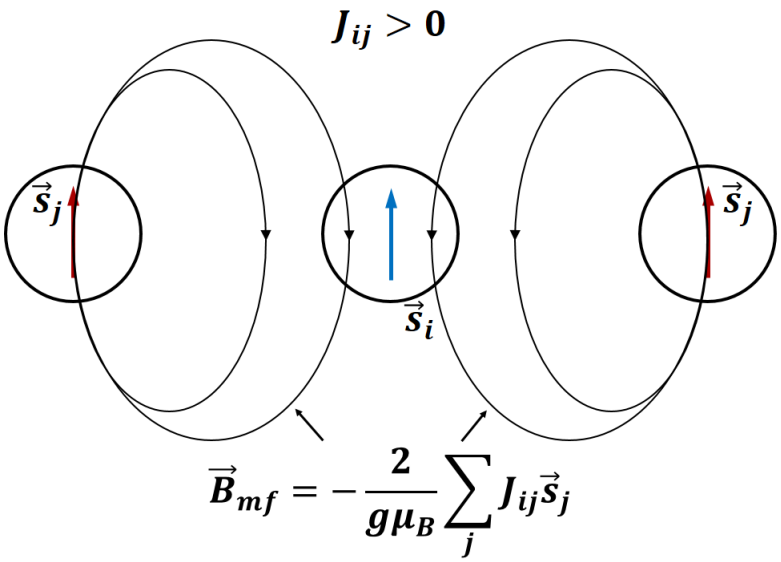

Figure 1.4: Illustration of the Weiss molecular field $\mathbf{B}_{mf}$ caused by neighbouring spins $\mathbf{s}_j$.

magnetization occurs at temperatures below the critical temperature T_C. For $T = T_C$ the transition temperature can be found as:

$$T_C = \frac{n\lambda\mu_{eff}^2}{3k_B} \tag{1.20}$$

If $B \neq 0$ in equation 1.18, an equation for the susceptibility χ is found to be[15]:

$$\chi = \frac{C}{T - T_C} \tag{1.21}$$

where equation 1.21 is the Curie-Weiss Law for a ferromagnetic compound, and C is Curie's constant as obtained from the paramagnetic case. Typical behaviour for all three magnetic structures are shown in figure 1.5. The main overall difference between ferro- and ferrimagnetic behaviour is the magnitude of the magnetization or susceptibility.

For an antiferromagnet we must consider two separate components to explain the non-zero behaviour below T_N. Consider an antiferromagnet ($T < T_N$) with the

ordered spins perpendicular to the magnetic field. The magnetic moment of each sublattice in the antiferromagnet cants slightly as a result of the applied field. This is known as the perpendicular susceptibility that has a non-zero value equal to $\chi_{\perp}(T < T_N) = \chi(T_N)$[15]. If instead the magnetic order in the antiferromagnet forms parallel to the magnetic field – with the spins ordering in the same direction as the applied field, no canting occurs and the susceptibility $\chi_{||} \to 0$ as $T \to 0$. This holds for bulk crystals. If we consider the random distribution of particles in a powder sample, the susceptibility is than a combination of the parallel and perpendicular components of the susceptibility. If the magnetic field is in the z direction, only the z direction is parallel to the magnetic field resulting in 2/3 of the susceptibility arising from the perpendicular (x and y) components. And so, for particles we find:

$$\chi(T < T_N) = \frac{1}{3}\chi_{||}(T) + \frac{2}{3}\chi_{\perp}(T_N) \tag{1.22}$$

Returning to equation 1.21 for the purposes of fitting the paramagnetic portion of the susceptibility above T_N the Curie-Weiss law is recast as:

$$\chi = \frac{C}{T - \theta} \tag{1.23}$$

Overall, $\theta > 0$ indicates the sample is ferro- or ferrimagnetic, and $\theta < 0$ indicates that the sample is antiferromagnetic. The case of $\theta = T_C$ is part of the assumption we made when simply regarding nearest neighbour z interactions in the calculation of χ. For an antiferromagnet, λ , $J_{ij} < 0$, and experimentally θ can be much larger than T_N. θ is then not a useful estimate of the ordering temperature unless interactions are weak. But, it does provide us with another quantification of the overall exchange in the sample. Using equations 1.19 and 1.20 we can express the exchange constant

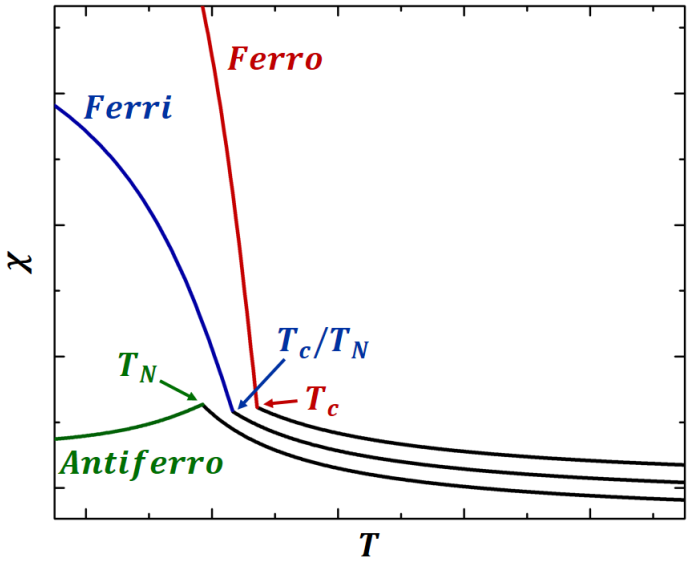

Figure 1.5: Susceptibility $\chi(T)$ for a ferro-, antiferro-, and ferrimagnet. Below the ordering temperature (T_N or T_C) we can see the behaviour of a typical magnetically ordered system. Above the ordering temperature each system becomes paramagnetic.

J_{ij} using measurable quantities:

$$J_{ij} = \frac{3k_B T_N}{2zj(j+1)} \quad \text{(Antiferro)} \tag{1.24}$$

T_N can be obtained directly from the susceptibility χ of a material, while $j(j+1)$ is obtained from the equation of μ_{eff}, where the effective magnetic moment is obtained from a fit of the susceptibility χ.

For Co_3O_4 van Vleck paramagnetism χ_0 must be taken into account for the Co^{2+} and Co^{3+} ions[17; 20], leading to the modified Curie-Weiss law:

$$\chi = \chi_0 + \frac{C}{T-\theta} \tag{1.25}$$

1.1.3 Exchange Interactions

Magnetic order results from magnetic exchange between two ions with unpaired spins leading to interactions that either align the respective magnetic moments parallel or anti-parallel. Unpaired electrons in a solid ($3d^n$ metal) locate themselves inside orbitals which can extend far enough away from the ion to interact with other electrons in orbitals belonging to neighbouring ions. The exchange Hamiltonian given by $\mathcal{H}_{ex} = -\frac{1}{2}\sum_{ij} J_{ij}\mathbf{s}_i \cdot \mathbf{s}_j$ determines, through Coulomb interactions and the Pauli exclusion principle, the sign of J_{ij}. For two magnetic ions separated by a distance R the sign of J_{ij} is determined by the amount of orbital overlap of the two orbitals containing unpaired electrons (figure 1.6). When R is large the overlap of the interacting orbitals is small and Coulomb repulsion between the electrons dominates forcing the spins to remain parallel with one another. This is analogous to Hund's first rule, where, given orthogonal orbitals, the maximum spin provides the ground state. For a very small separation between ions the overlap is large, and the electron from ion 1 can be found inside the orbital of ion 2. In this case, the electron-electron repulsion term is negligible and the Pauli exclusion principle initiates anti-parallel alignment of the electron spins. The interaction between two neighbouring ions with unpaired electrons is known as direct exchange and is due to the direct overlap between orbitals containing a magnetic moment. Heitler and London first proposed a form of direct exchange illustrating this concept for the H_2 hydrogen molecule[21].

The situation is more complicated in oxide compounds, where nearest neighbouring ions are oxygen, minimizing the direct overlap between cationic $3d$ orbitals. The magnetic ordering of $3d$ transition metal oxides cannot be explained with simple

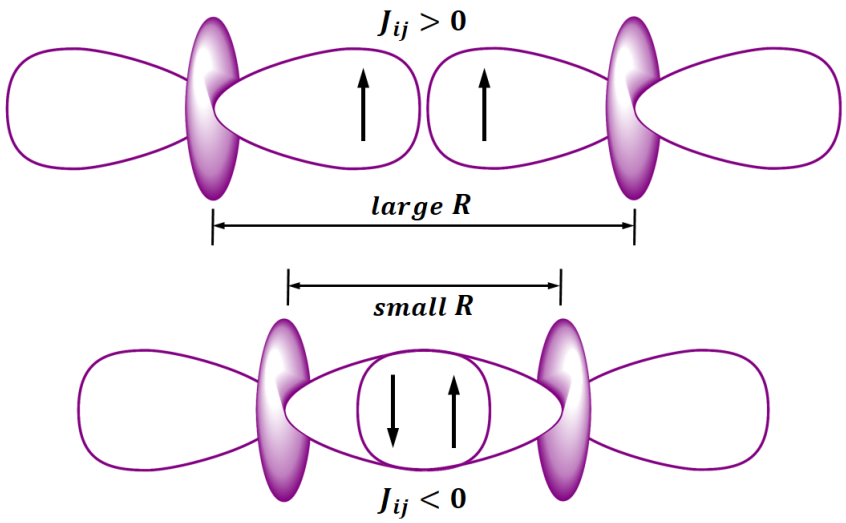

Figure 1.6: Top: A large seperation between ions leads to ferromagnetic alignment of the spins (Coulomb repulsion and Hund's first rule). Bottom: When overlap between the d-orbitals occurs the spins align antiferromagnetically (Pauli exclusion).

direct exchange between the cations. An additional indirect exchange mechanism known as superexchange was first realized by Kramer[22] and further developed by Anderson[23; 24], Goodenough[25; 26], and Kanamori[27]. Superexchange involves a coupling between cationic unpaired spins through intermediary O $2p$ orbitals that overlap with the $3d$ orbitals of the respective cations. These exchange interactions takes the form of M-O-M (with M indicating a metal site), and is described physically by the Goodenough-Kanamori-Anderson (GKA) rules that dictate the sign of J_{ij} under the situation of 180° and 90° superexchange interactions[24; 25; 27]. For an interaction angle of 180° the superexchange interaction promotes antiferromagnetic order between the cations, where the 90° interaction results in weaker ferromagnetic ordering between the cations ($2p_x$ and $2p_y$ orbitals are orthogonal, thus both can be spin up; figure 1.7).

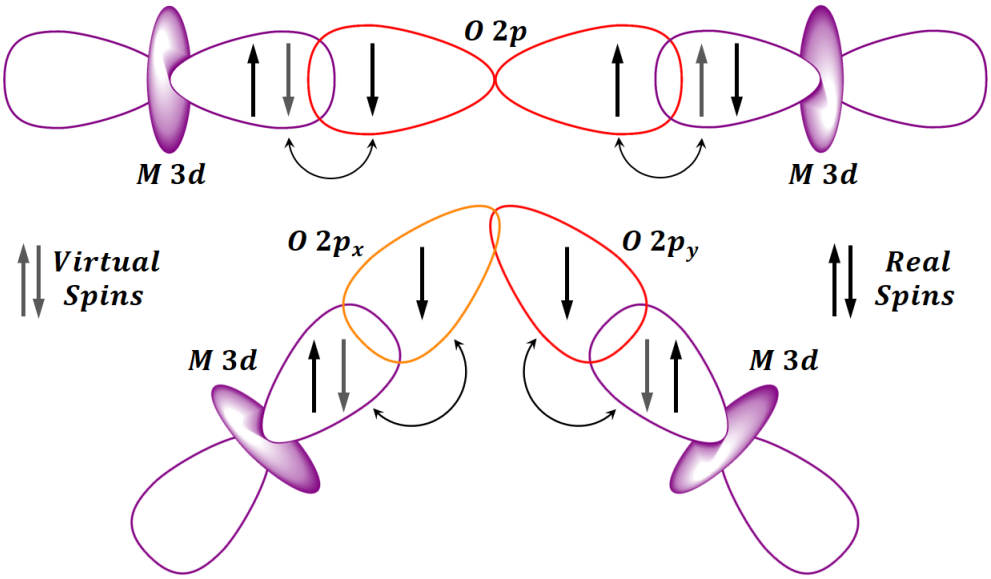

Figure 1.7: Diagram of the superexchange interaction occurring with bond angles of top: 180°, and bottom: 90°, producing antiferromagnetic and ferromagnetic alignment, respectively.

Superexchange occurs through a virtual transfer of electrons where the electrons located in the filled $2p$ O orbitals interact oppositely with each of the $3d$ electrons of the M sites. A quantitative treatment of the superexchange interaction can be found using the Hubbard model[28] for exchange interactions, which invokes the use of a hopping parameter t and Coulomb site repulsion U. The magnetic ground state of the Hubbard Hamiltonian is obtained by minimization of the two energies which can be seen as competitive behaviour. The hopping energy involves a delocalization of the electrons of the same spin between atoms, while the Coulomb energy favours localized electrons keeping the moments confined to different atoms[29]. This balance comes from a value t that is incurred from an electron hopping from atom to atom, and U, the energy incurred when an electron hops onto the same atom (due to Coulomb repulsion). This leads to the relation between the exchange in the Hubbard model

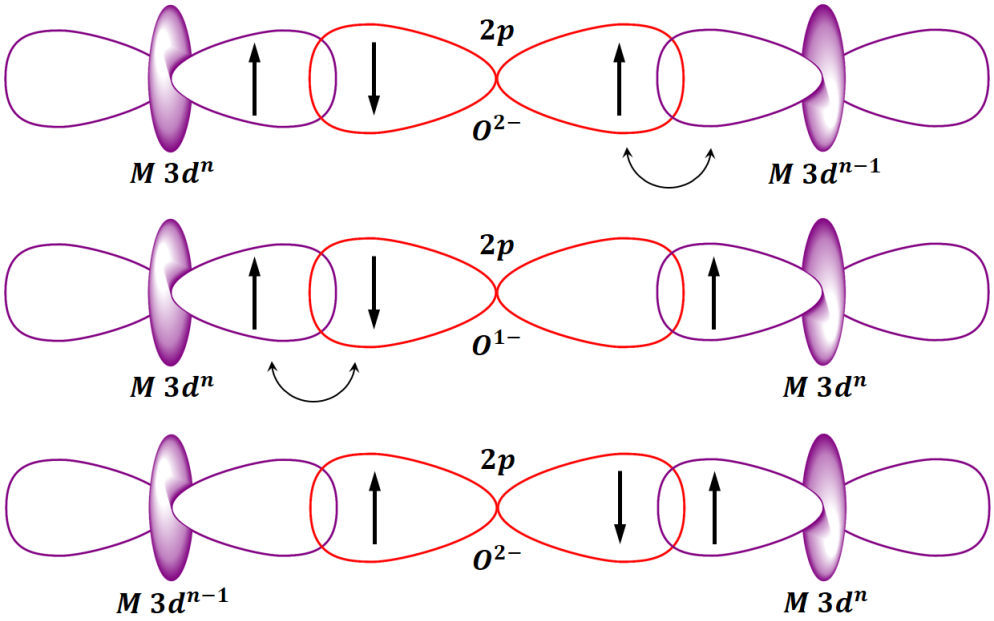

Figure 1.8: Illustration of double exchange interaction between two similar ions differing by a valency of one, e.g. Mn^{4+} and Mn^{3+}. An electron with spin up hops from the oxygen ion onto a vacant d orbital on ion 2. To fill the vacancy on the oxygen, a spin up electron from ion 1 must be transferred, causing delocalization.

and the exchange from the Heisenberg model[14]:

$$J_{ij} = -\frac{2t^2}{U} \tag{1.26}$$

where the negative sign arises due to the convention of defining $\mathcal{H}_{ex}$ as in equation 1.15 and t^2 arises because the electron is considered to hop twice. This situation is depicted in figure 1.7. The electrons of the O $2p$ ion interact with the metal $3d$ unpaired spins, propagating the exchange interactions through the O orbitals. It must be stated that this is a virtual process. O $2p$ spins do not participate in real charge transfer which can alter the overall spin on the metal ion, i.e. the magnetic moments of all the participating ions remain the same throughout the interactions.

On the other hand, transition metal oxides can also undergo another form of ferro-

magnetic exchange, known as double exchange. First characterized by Zener[30] who explained the properties of mixed valence Mn perovskites, double exchange is shown in figure 1.8 and it occurs between two identical ions differing only by a valence of one, e.g. Mn^{3+} and Mn^{4+} in octahedral symmetry undergo double exchange. Double exchange produces a real charge transfer effect leading to a change in the magnetic moments of the involved cations. The exchange proceeds by an electron transfer from the oxygen to an empty orbital of cation B and transfer of an electron from cation A to the vacant orbital on the oxygen (figure 1.8). Utilizing the same Hubbard model for exchange interaction we find a ferromagnetic ground state between the ions. Electron conduction in many oxides can be explained using double exchange[14; 29]. The electron from one metal hops back and forth between the other metal ion, and the electron is thus delocalized throughout the entire M-O-M configuration.

1.2 Nanoparticle Magnetism

At the surface of a material, the atomic environment is altered by the broken coordination caused by the lack of symmetry at the surface. This can be exploited by utilizing nanoparticles effectively increasing the surface to volume ratio such that the surface becomes a measurable contribution of the magnetic properties[4; 31; 32]. Broken coordination and finite size effects can result in very different behaviour at the surface[4; 5; 32; 33].

1.2.1 Anisotropy

Anisotropy of a magnetic system is generally described by two factors. Intrinsic to the crystal and magnetic structure is the magnetocrystalline anisotropy K_u, while shape anisotropy, K_s, is due to dipole-dipole interactions between ions that are long range (demagnetization field). When a material is exposed to a magnetic field, the anisotropy affects the direction of the net magnetization. This manifests itself in the crystal structure as an axis in which the spins preferably align, known as the 'easy' axis. Spin-orbit interactions couple to the spin orientation of the lattice, leading to both the hard, and easy axes (figure 1.9). The energy E_a to rotate the magnetization M an angle θ away from the easy axis is given by[14; 15]:

$$E_a = K_{u,1} \sin^2 \theta + K_{u,2} \sin^4 \theta + \cdots \tag{1.27}$$

where $K_{u,i}$ are the anisotropy constants. The equation 1.27 is representative of a uniaxial anisotropy where there is no distinction between 0 and 180°.

Another form of anisotropy results from the demagnetization field $\mathcal{N}$. For an prolate ellipsoid with magnetic saturation M_s the shape anisotropy K_s is described as[34]:

$$K_s = \frac{1}{4}\mu_0 M_s^2 (1 - 3\mathcal{N}) \tag{1.28}$$

The demagnetization field is itself dependent on the shape of the particle. For a sphere, $\mathcal{N} = 1/3$, resulting in no shape anisotropy. For thin films or large flat particles, the shape anisotropy can be expressed as a function of the angle θ relative to the normal of the surface[15; 35]:

$$K_s^{flat} = \frac{1}{2}\mu_0 M_s \cos^2 \theta \tag{1.29}$$

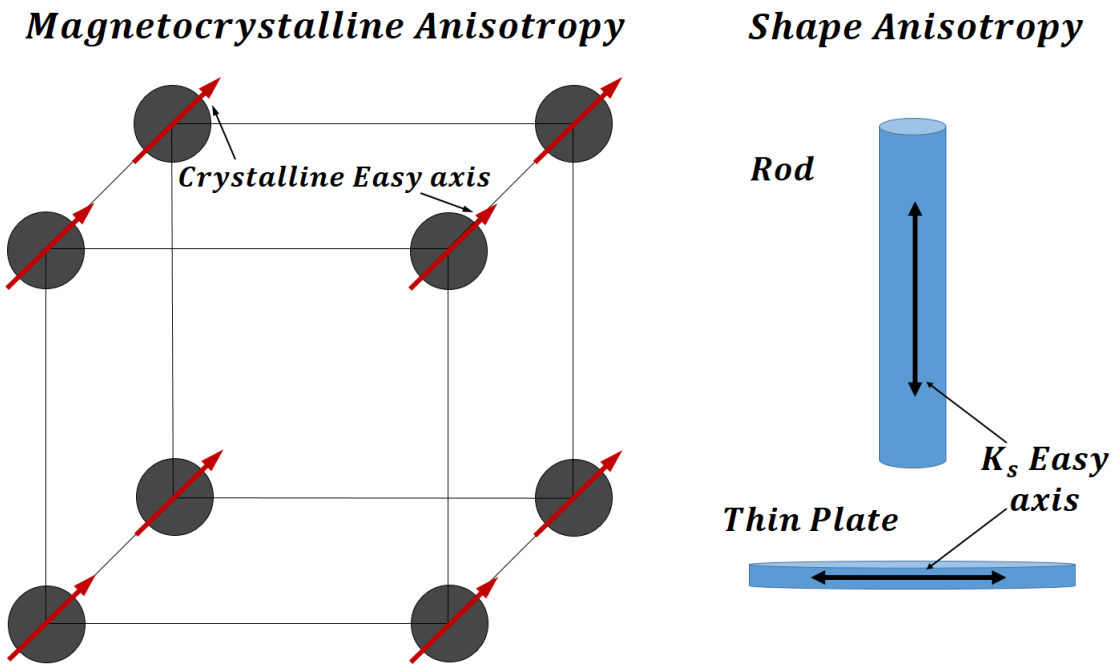

Figure 1.9: Left: Representation of magnetocrystalline anisotropy illustrating the crystalline easy axis. Right: Shape anisotropy for a long thin rod and flat disk shaped particles.

which minimizes K_s^{flat} if the direction of **M** is parallel to the plane (figure 1.9)[15].

1.2.2 Domains and Single Domain Particles

In large particles or bulk materials magnetic domains form as a way to minimize the overall energy by reducing the demagnetization field and thus the overall magnetization of the sample[15]. In a multi domain structure, each domain contributes its own demagnetization field and, in addition, between the domains the magnetic moments of the spins rotate to accommodate the change in direction. These are known as domain walls, with the most common type known as a Bloch wall. Domains can move, create, and destroy one another to minimize the overall magnetic energy with respect to the

field direction and magnitude. If the dimensions of the particle are small enough (e.g. nanoscale, where the demagnetization energy is roughly equal to the energy of the domains) single domain particles can form, where it becomes more energetically favourable to eliminate any domain walls in the small structure[36]. Multi-domain and single domain particles are shown in figure 1.10, with no applied magnetic fields larger particles can minimize M (soft ferromagnet, low K).

In single domain nanoparticles the magnetic moments act together as an individual coherently rotating super-magnetic moment where magnetization reversal can be achieved spontaneously by overcoming a barrier activated by thermal energy. This is described by the Stoner-Wohlfarth model[37]. A representation of the Stoner model is shown in figure 1.11. In the absence of an applied magnetic field the energy associated with spontaneous magnetization reversal for a single domain nanoparticle is

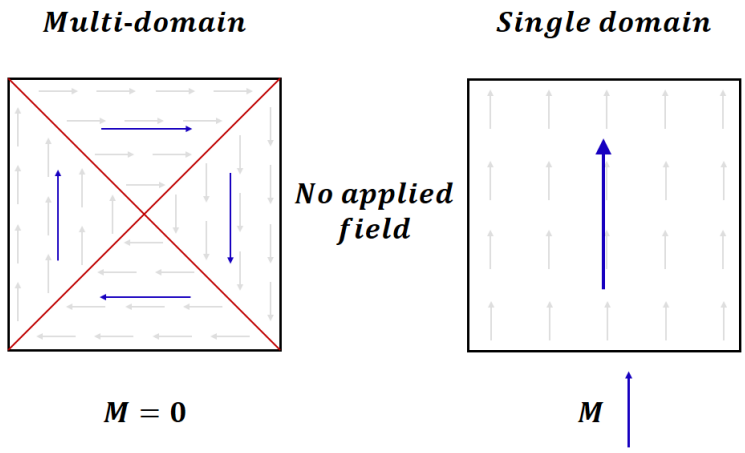

Figure 1.10: Without an applied magnetic field, materials such as soft ferromagnets tend to form domains that minimize the overall magnetization. All the spins in a single domain particle contain the same easy axis and the magnetization of the particle can be represented by a single vector.

given by:

$$E = KV \sin^2 \theta \tag{1.30}$$

where K is the overall anisotropy described by magnetocrystalline and shape effects and V is the volume of the nanoparticle. The nanoparticle contains two easy axes, shown in figure 1.11 as the energy minima at 0 and 180°. The energy barrier to reverse the spins is then $\Delta E = KV$, with thermal energy greater than this barrier $k_B T \geq \Delta E$ spins can easily fluctuate between the two spins states. The behaviour associated with the spontaneous reversal results in paramagnetic behaviour, but with an enhanced magnetization leading to the designation *superparamagnetism*. As temperature decreases, the ability to spontaneously reverse decreases, where at $T \leq T_B^{sp}$ the spins are locked in one configuration. The threshold temperature T_B^{sp} at which spontaneous reversal ceases with cooling is known as the superparamagnetic blocking

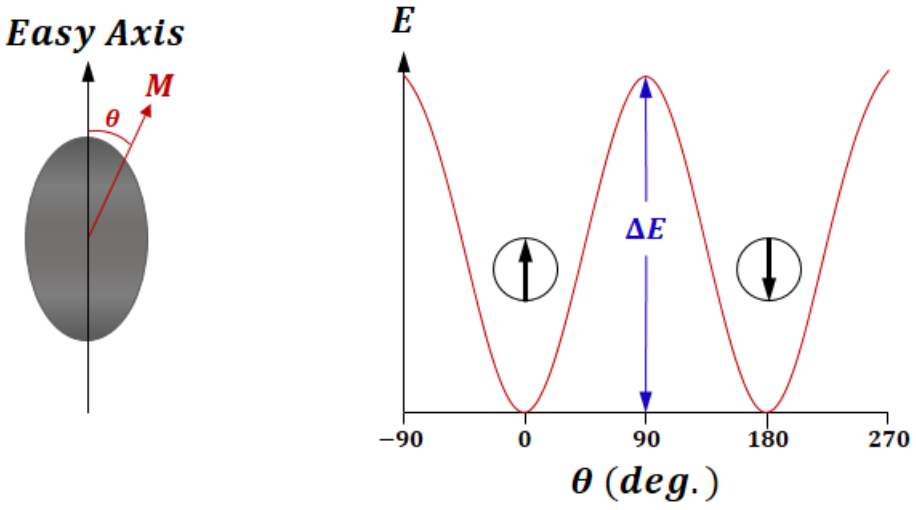

Figure 1.11: Left: Illustration of a single domain nanoparticle with the magnetization M at some angle θ to the easy axis. Right: Dependence of the energy E on the angle θ of M, showing two minima at $\theta = 0°$ and $\theta = 180°$ seperated by an energy barrier ΔE.

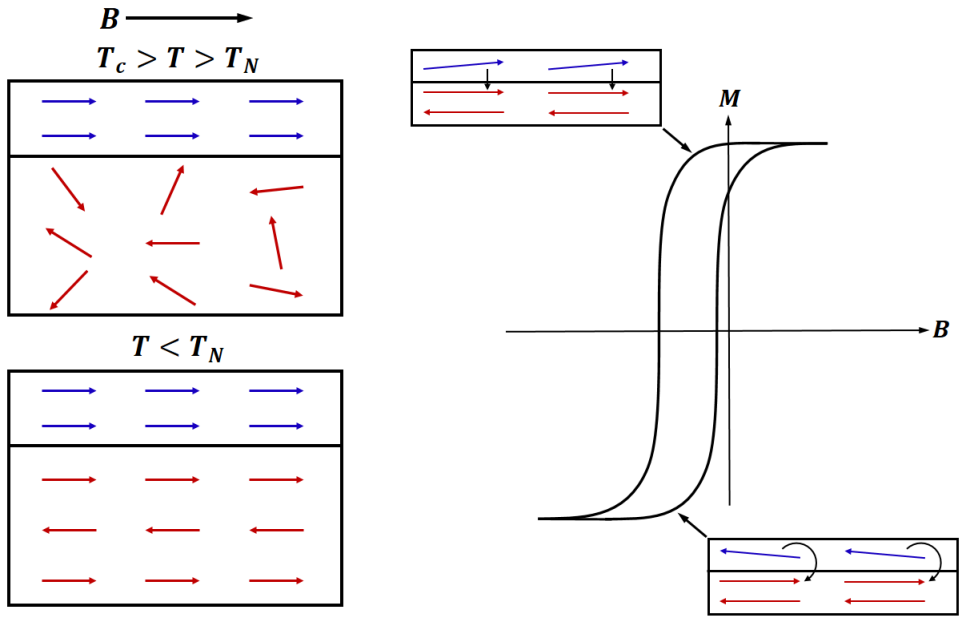

Figure 1.12: Representation of exchange bias caused by interfacial coupling between a ferromagnetic and antiferromagnetic material. Exchange bias causes a horizontal shift in the magnetization M of a hysteresis loop.

temperature.

1.2.3 Exchange Bias

There can exist a special exchange coupling between two different magnetically ordered systems including any combination of ferro, ferri, or antiferromagnetic materials. The phenomenon is known as exchange bias, first characterized by Meiklejohn and Bean[38]. Core-shell nanoparticles and multi-layered thin films display an interfacial coupling between magnetic materials, e.g. ferromagnetic and antiferromagnetic layers[38–43].

Consider if the ordering temperatures of the ferromagnetic and antiferromagnetic materials are T_C and T_N, respectively, with $T_C > T_N$. If the system is cooled below

$T < T_C$ with an applied magnetic field, the magnetization direction of the ferromagnetic material is then set by the field. Subsequent cooling below $T < T_N$ then forces the spin configuration for the antiferromagnetic material due to the interfacial exchange interactions between the layers (figure 1.12). The interfacial exchange further influences the magnetic alignment as the magnetic field changes. By reducing the magnetic field the magnetization begins to return to zero, but it is found that when interfacial exchange between ferro- and antiferromagnetic layers are present a horizontal loop shift occurs in the magnetization vs. field ($M(\mu_0 H)$) hysteresis loops. The system is considered to have a unidirectional anisotropy, where the exchange coupling between layers pins the ferromagnetic state in a given direction requiring a much larger reversal field to overcome the exchange energy. This can be represented by a torque on the rotating ferromagnetic spins from the antiferromagnetic layer. On returning the field to its original value the ferromagnetic magnetization flips much easier, as if the exchange from the antiferromagnetic spins and field were cooperative, exerting a torque (figure 1.12). This idea shows that exchange bias forces a single anisotropic direction in the ferromagnetic layer, as opposed to general anisotropic considerations that contain uniaxial terms, e.g. $\sin^2\theta$ in figure 1.11 where 0 and 180° are favoured equally.

1.3 Crystal Fields

Crystal fields are generated by nearby neighbouring atoms forming a potential experienced by the cations in the structure. This leads to a break in symmetry operations, in turn responsible for the loss of degeneracy in the system. As well, we find that

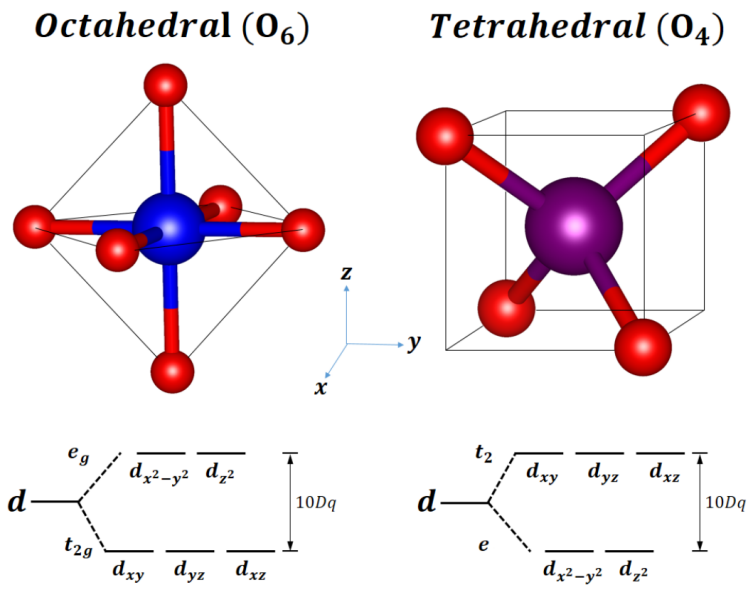

Figure 1.13: Illustration of common crystal field environments. a) Octahedral (O_6) interstices contains a center cation surrounded by six oxygen ions. The position of the oxygen ions causes the e_g orbitals to be pushed higher in energy. b) For tetrahedral coordination (O_4), the four oxygen ions lie at opposite corners of a cube lying closer to the t_2 orbitals.

the magnetocrystalline anisotropy discussed above is a result of the coupling between the orbit and lattice through the spin-orbit interaction and partial quenching of the angular momenta[15].

1.3.1 Ligand Field Theory

Positive cations such as $3d^n$ transition metal ions inside a crystal structure can be bonded to neighbouring negative anions through ligands. The relationship between cations and ligands is very important and leads to the discussion of ligand field theory which focuses on the field created by the neighbouring electronic (usually $2p$) orbitals and their orientation with respect to the cation d-orbitals. There are five degenerate

d-orbitals which can split in energy inside a crystal field. For a cubic system, oxygen surrounds the cation in one of four configurations: Tetrahedral (T_d), octahedral (O_h), simple cubic, and dodecahedral. For a cubic unit cell the crystallographic a, b, and c directions are all 90° apart with equal dimensions $a = b = c$. The tetrahedral and octahedral configurations are shown in figure 1.13 where four oxygen ions are located at the opposite corners of a cube for T_d sites, and O_h sites contain six oxygen ions at the corners of an octahedron. The octahedral (tetrahedral) crystal field causes a splitting of the *d*-orbitals into the e_g (e) and t_{2g} (t_2) orbitals, where the subscript g indicates an inversion symmetry present for the octahedral sites. The e_g (e) orbital contains the d_{z^2} and the $d_{x^2-y^2}$ orbitals that point in the positive and negative directions of the Cartesian x, y, z-axes. The t_{2g} (t_2) orbital contains the d_{xy}, d_{xz}, and d_{yz} orbitals which direct themselves in the x-y, x-z, and y-z planes (figure 1.14).

A cursory description of ligand field theory is as follows: For cation orbitals that are degenerate, such as the *d*-orbitals of $3d^n$ ions, the *d*-orbitals that lie closer to ligand orbitals are pushed higher in energy relative to those farther away. Since the e_g orbitals lie directly along the Cartesian axes (x, y, z) for the octahedral (O_6) oxygen coordination, we find that the electron configurations lie very close to the neighbouring O $2p$ orbitals pushing them higher in energy due to electron-electron repulsion. In the tetrahedral (O_4) coordination the t_2 orbitals are in close proximity to the O $2p$ orbitals and thus higher in energy relative to the e orbitals. The crystal field plays an important role in determining the overall spin configuration. The strength of the crystal field can result in different spin configurations for the same ion.

Consider Co^{3+} with a d^6 electron configuration in an octahedral crystal field.

With a small magnitude of the crystal field, Co^{3+} orbitals split to accommodate four unpaired spins ($s = 2$). If the crystal field is large enough all six electrons occupy the lower t_{2g} orbitals in a paired (spin up - spin down) configuration with no net spin ($s = 0$). The first situation arises as a direct result of Hund's rules which state: 1) The state with the maximum spin (s) is lowest in energy i.e. fill each orbital with spin up then subsequently add spin down; 2) Within the construct of maximum spin, the state with maximum angular momentum (l) is the ground state, i.e. start filling with the $m_l = +l$ state down to $m_l = -l$; 3) if the d shell is less then half full ($3d^5$), the total angular momentum is $j = l - s$ while if the shell is more then half full the ground state is given by $j = l + s$. This state is represented in the notation ${}^{2s+1}l_j$. Returning to the second (low spin) configuration for Co^{3+}, we find it violates Hund's first rule

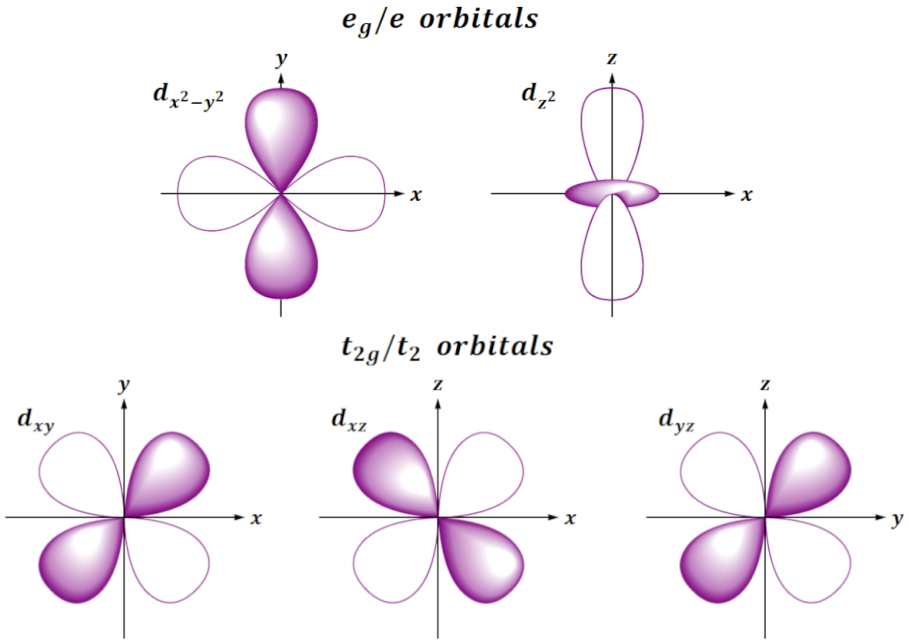

Figure 1.14: Illustration of the five d-orbitals. e_g orbitals all lie along the Cartesian axes.

of maximum spin. Thus, when the crystal field is larger then the Hund coupling ($\mathcal{H}_{CF} > \mathcal{H}_{Hund}$) this results in very strong electron-electron interactions between the metal $3d$ and O $2p$ electrons pushing the e_g orbital much higher in energy. This makes it more energetically favourable to enter a low-spin state as opposed to the usual high-spin state prescribed from Hund's rules.

1.3.2 Jahn-Teller Effect

By altering the cubic crystal field some of the remaining degeneracies of the d-orbitals can be lifted. Jahn and Teller originally noted that the normally cubic crystal field for Cu $3d^9$ contained a tetragonal component when the Cu occupied octahedral coordinations[14]. The Jahn-Teller (J-T) effect produces a singlet ground state

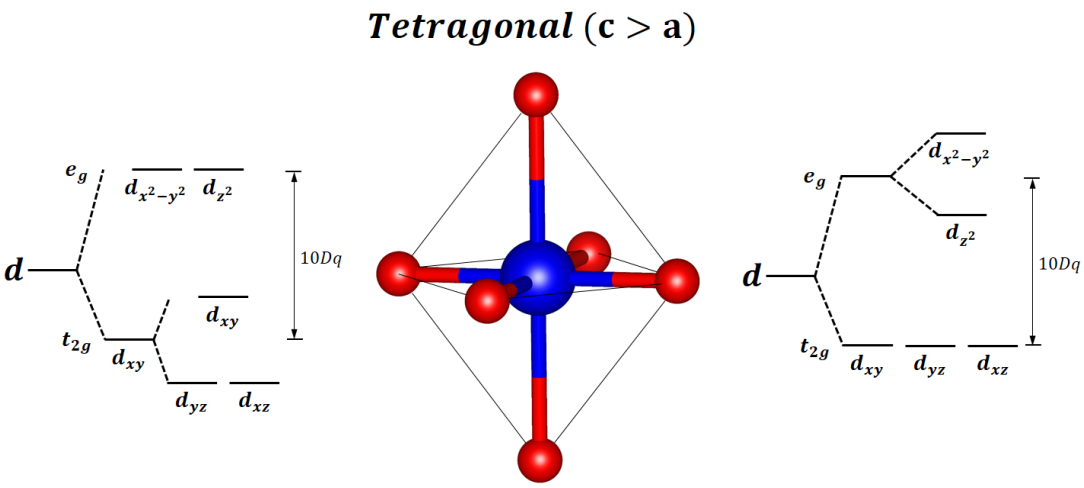

Figure 1.15: Representation of the Jahn-Teller effect for a tetragonal distortion (extension) along the z-direction of the octahedral site. Based on the magnetic ground state of the ion, the e_g or t_{2g} orbitals can split in energy. Orbitals that lie in the $x-y$ plane are higher in energy due to the closer proximity to the ligands.

which may still contain spin degeneracies. For octahedral coordination a distortion along the $\langle 001 \rangle$ z-axis caused by extension or contraction of c axis ($c > a$ or $c < a$) induces a tetragonal crystal field component that splits the degenerate states accordingly. For an extension in the z direction the $d_{x^2-y^2}$ orbital gets pushed higher in energy relative to the d_{z^2} since the oxygen ions that lie in the x-y plane are closer in proximity to the metal ion than oxygen ions along the z (c) direction (figure 1.15). Depending on the magnetic ground state of the $3d^n$ ion in question, splitting can also occur for the t_{2g} degenerate orbitals where d_{xy} is now closer to the O $2p$ orbitals than the d_{xz} and d_{yz}.

The J-T effect can only occur in certain $3d^n$ configurations when the magnetic ground state is a doublet E or triplet T (Mulliken irreducible representation symbols signify the degeneracies involved for a given state). A singlet (A) ground state does not undergo a splitting of the d-orbitals under a distortion of the octahedron. For the case of Cu^{2+} ($3d^9$) in an octahedral site the t_{2g} orbitals contain paired spins while the e_g orbital contains one unpaired electron (^2E, where superscript denotes the number of unpaired spins plus one) thus resulting in a splitting of the e_g orbitals. For Cu^{2+} ($3d^9$) in a tetrahedral site all spins in the e orbital are paired and one unpaired spin resides in the three degenerate t_2 orbitals. Thus $Cu^{2+}(T_d)$ contains a triplet ground state ^2T resulting in a splitting of the t_2 orbitals. There is also a temperature dependence to the J-T effect. By increasing the temperature, vibronic states can reinstate the degeneracy between the two split orbitals[14]. For doped ions that undergo the J-T effect the distortion is local to the doped ion, but at a certain occupancy the bulk structure can change symmetry, e.g. from cubic to tetragonal[14].

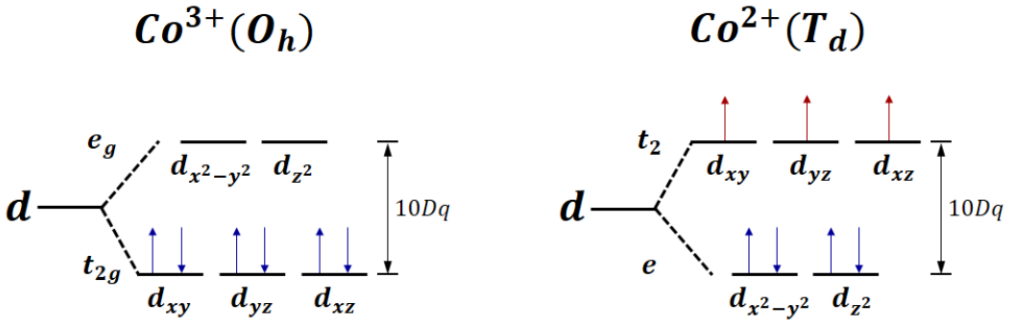

Figure 1.16: Spin occupation of the d-orbitals for Co^{2+} and Co^{3+} ions in the Co_3O_4 structure. Co^{3+} is in the low-spin state with all spins paired in the lower t_{2g} orbital, while Co^{2+} contains three unpaired spins in the upper t_2 orbitals.

1.4 Co_3O_4 Crystal and Magnetic Structure

Co_3O_4 is a normal spinel with the ionic configuration (A) $[B]_2O_4$. Normal spinels contain 2+ ions in tetrahedral (A) sites and ions with a 3+ oxidation state in octahedral [B] sites. Co^{2+} resides in the weak cubic crystal field of a tetrahedral site with a d^7 electronic configuration. This results in three unpaired spins ($s = 3/2$) in the higher energy t_2 orbital, while Co^{3+} is in the d^6 electronic configuration with all spins paired in the lower energy t_{2g} orbitals arising from the strong crystal field of the octahedral site (figure 1.16). Thus Co^{3+} is non-magnetic and does not participate in traditional superexchange interactions. Additionally, because the electron occupation in Co^{3+} contains only paired spins, electron transfer from double exchange is forbidden. In a spinel lattice the cations form in an octahedral and tetrahedral configuration with a ratio of the sites equal to (O_h:T_d) 2:1. Thus for every tetrahedral site there are two octahedral sites. For spinels there are many exchange interactions possible because of the distribution of cations.

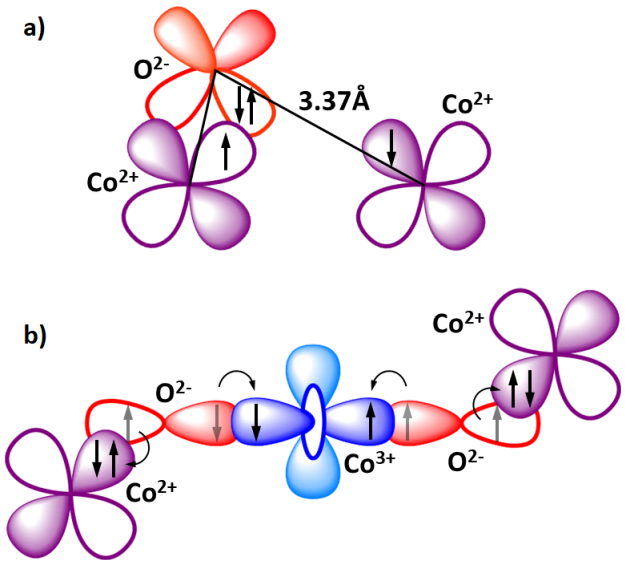

Figure 1.17: (a) Shows the interaction path of the Co^{2+} - O - Co^{2+} configuration. O^{2-} orbitals are shown in red and orange; Co^{2+} and Co^{3+} orbitals are shown in purple and blue, respectively. The large distance (3.37 Å) associated with the exchange leads to the small interaction energy. b) Shows one of the possible configurations for the Co^{2+}- O - Co^{3+}- O - Co^{2+} pathway. The distances between the interacting ions are much smaller allowing antiferromagnetic interactions to propagate through Co^{3+} orbitals.

Direct exchange interactions typically account for a very low portion of the exchange energy in a transition metal spinel oxide. This is due to the large distances associated with magnetic cations (figure 1.17). Typically superexchange and double exchange interactions are the mechanisms responsible for the magnetic order observed in these oxides. The dominant interactions arise from superexchange (or double exchange) between the octahedral B sites (B-O-B) and from superexchange between tetrahedral A and B sites (A-O-B). For Co_3O_4, the configuration of Co^{2+} and Co^{3+} in the spinel structure of Co_3O_4 does not provide a means for conventional superexchange (figure 1.17).

The magnetic ordering of Co_3O_4 is still explained via superexchange interactions

by including Co^{3+} in the exchange in a way that the interactions can propagate *through* the non-magnetic ion[20; 44]. This is also made possible by the unoccupied higher energy e_g orbitals that allow the spins from the neighbouring O ions to interact with each other through the Co^{3+} (figure 1.17 b)[20]. The exchange interactions then occur between two magnetic Co^{2+} ions, through two oxygen atoms, and a Co^{3+} ion in the form Co^{2+}- O - Co^{3+}- O - Co^{2+}. This process involves a virtual transfer of electrons through the Co^{3+} and thus resembles the superexchange interaction that occurs through an oxygen ion. This is referred to as the extended superexchange interaction. In Co_3O_4 this interaction can occur through three different exchange pathways, shown in figure 1.18, with two antiferromagnetic exchange pathways and one ferromagnetic exchange pathway ($\uparrow\uparrow_{90}$, $\uparrow\downarrow_{90}$, and $\uparrow\downarrow_{180}$). The notation indicates whether the path is ferro- ($\uparrow\uparrow$) or antiferromagnetic ($\uparrow\downarrow$) and the subscript denotes the angle of the O - Co^{3+}- O bond. This was first characterized by Roth using a range of spinel oxides[20; 44]. For instance, a bulk structural analogue of Co_3O_4, $CoAl_2O_4$, has a much smaller exchange strength $J_{ij}/k_B = 0.4$ K, compared to that of bulk Co_3O_4 at $J_{ij}/k_B = 4.0$ K[44]. This is a result of replacing the Co^{3+} ions with Al^{3+} at the intermediate octahedral sites. The intervening Al^{3+} ion p-orbitals get repelled to higher energy by the p-orbitals of the O ions, and the exchange pathway through Al^{3+} becomes unavailable. By comparison to $CoAl_2O_4$, the Co^{2+}- O - Co^{3+}- O - Co^{2+} exchange paths account for roughly 90% of the exchange strength in Co_3O_4.

The orientation of the Co^{2+} and Co^{3+} ions in the spinel structure allow for a large multiplicity of these three interaction paths. Where the multiplicity indicates the number of possible interaction pathways occurring from a given Co^{2+} to all of

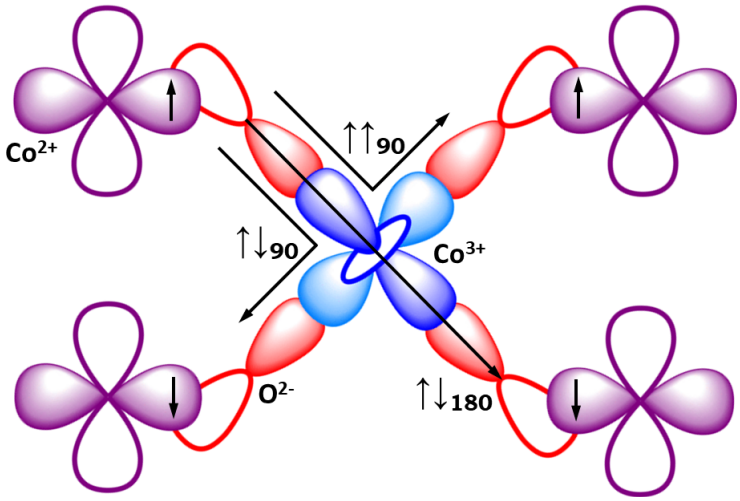

Figure 1.18: Different possible exchange pathways between Co^{2+} ions (purple) through an intervening Co^{3+} ion (blue) and two oxygen ions (red). In the $\uparrow\downarrow_{180}$ Co^{2+} ions are connected through the same d-orbital on Co^{3+} producing an antiferromagnetic interaction. $\uparrow\uparrow_{90}$ and $\uparrow\downarrow_{90}$ are connected through the same d-orbital resulting in one ferromagnetic and one antiferromagnetic interaction, due to the Pauli exclusion principle.

its respective neighbours, e.g. there are four nearest neighbouring Co^{2+} ions and each neighbour has six possible pathways involving the extended exchange interaction ($6 \times 4 = 24$). The paths $\uparrow\downarrow_{90}$ and $\uparrow\uparrow_{90}$ occur with a multiplicity of 24, while the antiferromagnetic $\uparrow\downarrow_{90}$ path occurs between nearest neighbouring Co^{2+} ions, and the ferromagnetic $\uparrow\uparrow_{90}$ path occurs between next-nearest neighbours. The $\uparrow\downarrow_{180}$ path occurs with a multiplicity of 12 between *next-next-nearest* neighbouring ions. Examining the exchange pathways in figure 1.18 we note that all of the Co^{2+}- O - Co^{3+} paths are identical with the only possible difference arising from the O - Co^{3+}- O bond angle, and virtual hopping through different Co^{3+} *d*-orbitals. The exchange pathways $\uparrow\downarrow_{90}$ and $\uparrow\uparrow_{90}$ have the same bond angle and multiplicity, but opposite interactions, thus to first order their interactions strengths cancel[20; 44]. In the bulk, cancella-

tion of these exchange paths indicate that the magnetic order originates from the exchange between next-next-nearest neighbouring Co^{2+} ions ($\uparrow\downarrow_{180}$). At the surface of nanoparticles this perfect cancellation does not occur and competition between ferro- and antiferromagnetic exchange leaves the possibility of dominant surface ferromagnetism.

Chapter 2

Experimental Methods

The synthesis and techniques used for characterization of the samples are described in this chapter. Techniques used include Scanning Electron Microscopy and Tunneling Electron Microscopy, X-ray diffraction, SQUID magnetometry and susceptometry, and X-ray Absorption Spectroscopy and Magnetic Circular Dichroism.

2.1 Nanoparticle Synthesis

2.1.1 Co_3O_4 Nanoshapes

I have synthesized three different shapes of Co_3O_4 nanoparticles; 1) cubes of side lengths 15 nm, 2) spheres of diameter 10 nm, and 3) hexagonal plates with a thickness of 8 nm and side-to-side length of 70 nm.

For the spheres, ϵ-Co was synthesized by first dissolving 0.1 g of trioctylphosphine oxide (TOPO) into 12 ml of o-dichlorobenzene and 0.2 ml of 99% oleic acid. The solution was then heated to 180°C under an argon atmosphere. In a separate solution, 0.54 g of dicobalt octacarbonyl ($Co_2(CO)_8$) was dissolved into 3 ml of o-

dichlorobenzene (DCB) and injected into the heated (180°C) solution of TOPO, oleic acid, and DCB. The obtained Co was washed using ethanol. The precipitate was dried in a furnace at 60°C for 12 hours in air. To obtain Co_3O_4 the ϵ-Co was placed in a tube furnace with a initial heating rate of 5°C/min until 350°C was reached, and the temperature was held for 3 hours. Subsequently, the temperature was ramped down at a rate of 2°C/min. Oxidation of Co causes transformations to first CoO then finally Co_3O_4[45].

For the cubes, a blue/green precipitate of cobalt hydroxide (α-$Co(OH)_2$) was synthesized by dissolving 9.52 g of cobalt chloride $CoCl_2{\cdot}6H_2O$ into 100 ml of distilled (DI) water. 25 ml of ammonium hydroxide NH_4OH was added and the solution was stirred for two hours[46]. Drying and calcination procedures were the same as the spheres.

For the plates, β-$Co(OH)_2$ was similarly synthesized by dissolving 4.76 g of $CoCl_2$ $\cdot 6H_2O$ 100 ml of DI water, while 3 g of sodium hydroxide (NaOH) was dissolved in 25 ml of DI water. The hydroxide solution was added into the $CoCl_2$ solution heated to 80°C and was stirred for two hours[47]. Drying and calcination procedures were the same as the cubes and spheres above. β-$Co(OH)_2$ contains divalent Co ions octahedrally coordinated to hydroxyl ions in a layered hexagonal brucite structure[48]. α-$Co(OH)_2$ forms a layered hexagonal hydrotalcite-like structure, but with Co ions in both tetrahedral and octahedral sites[48]. During the synthesis of the plates, the initial colour of the precipitate started blue/green as an α-$Co(OH)_2$ but immediately changed to the characteristic pink colour of β-$Co(OH)_2$. This occurred as the β phase is the more thermodynamically stable of the two forms[49]. Over the course of the

two hour synthesis the colour gradually changed from pink to a light brown. This indicated a transformation at the surface of the plates from β-$Co(OH)_2$ to CoOOH (cobalt oxyhydroxide) which contains trivalent Co ions[50]. The plate shape is formed at the β-$Co(OH)_2$ stage, after calcination the shape is retained with crystallites that form to compensate for the structural change.

The α-$Co(OH)_2$ (cubes) contains both octahedrally and tetrahedrally coordinated Co^{2+} ions at the surface of the as-synthesized particles, while the β-$Co(OH)_2$ (plates) contain only Co^{3+} octahedrally coordinated at the surface of the particles (due to the oxyhydroxide surface). It is for these reasons that we end up with the surface terminations and shapes in Co_3O_4, *i.e.* the cubes have a higher Co^{2+}:Co^{3+} ratio (1:2) at the surface with highly coordinated ions, and the plates have Co^{3+} ions with a very low coordination and a lower Co^{2+}:Co^{3+} ratio (1:1).

2.1.2 $\mathbf{Cu_xCo_{3-x}O_4}$

The $Cu_xCo_{3-x}O_4$ ($0 \leq x \leq 0.5$) spinels were synthesized via co-precipitation at Toyota Motor Engineering and Manufacturing North America. The appropriate amounts of $Co(NO)_3{\cdot}6H_2O$ and $Cu(NO)_3{\cdot}2.5H_2O$ were dissolved separately in deionized (DI) water and subsequently mixed together. A 2 M NaOH solution was then added dropwise to the stirred solution, and monitored until a pH of 9-10 was reached. The precipitate was washed with DI water, filtered, and dried at 120°C overnight. The samples were then calcined at 500°C for 1 hour with a heating rate of 2°C/min to obtain the $Cu_xCo_{3-x}O_4$ particles.

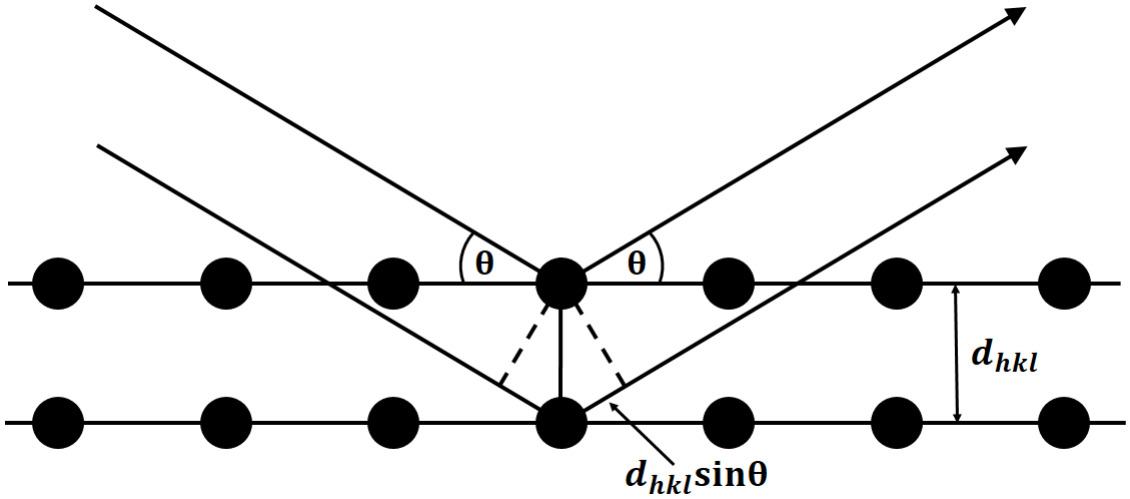

Figure 2.1: Schematic representation of Bragg diffraction occurring between two identical planes spaced d_{hkl} apart. Interference occurs when the difference in path length is an integer multiple of the wavelength.

2.2 X-ray Diffraction

Incoming x-rays interact and scatter off the electron densities surrounding the respective nuclei of a material. For a crystal structure that contains lattice symmetry, a diffraction pattern results due to the coherent superposition of x-rays. Constructive interference occurs when the difference in path length between incoming x-rays are integer multiples of the wavelength $n\lambda$ and follow the well-known Bragg equation describing x-ray diffraction:

$$n\lambda = 2d_{hkl}\sin\theta \tag{2.1}$$

where n is an integer, λ is the wavelength of the incoming x-rays, θ is the angle of the incoming x-rays, and d_{hkl} is the spacing between planes labelled by the Miller indices hkl. This is illustrated in figure 2.1.

For powder samples the width of a given reflection is largely determined by the size of the crystallites, with smaller crystallites broadening the reflection. This is intuitive from the picture of diffraction, as the number of "slits" through which light scatters is increased, the width of the resulting maxima after the slits are decreased. The broadening of the x-ray reflections due to crystallite size is described by the Scherrer formula[51; 52]:

$$\tau = \frac{K\lambda}{\beta \cos\theta} \tag{2.2}$$

where τ is the crystallite size of the material, K is the shape factor (0.9 for spherical particles), and β is the line broadening of the reflection.

For x-ray diffraction patterns of highly ordered materials, it is possible to obtain differences in reflection intensity based on the orientation of the material under consideration. Preferred orientation typically occurs in bulk single crystal diffraction but can also occur for non-random distributions of crystallites at the nanoscale. Specifically, for extreme oblate geometries such as thin plates, particles tend to stack horizontally[53]. For a particle with crystallites exposing a given *hkl* plane there is an increased diffraction intensity associated with that reflection[53]; a texture.

X-ray diffraction (XRD) was performed on all samples to obtain the structure, composition, crystallite sizes, and texture. Patterns were collected using the rotation stage of a Bruker D8 DaVinci diffractometer with Cu-K_α ($\lambda = 1.5406$ nm) radiation in Bragg-Brentano geometry (figure 2.2). The x-ray tube generates electrons from an electrically heated tungsten cathode which are accelerated through a potential difference (40 kV) and strike the Cu anode. With a tube current of 40 mA, characteristic Cu x-rays are generated alongside typical Bremsstrahlung radiation. The

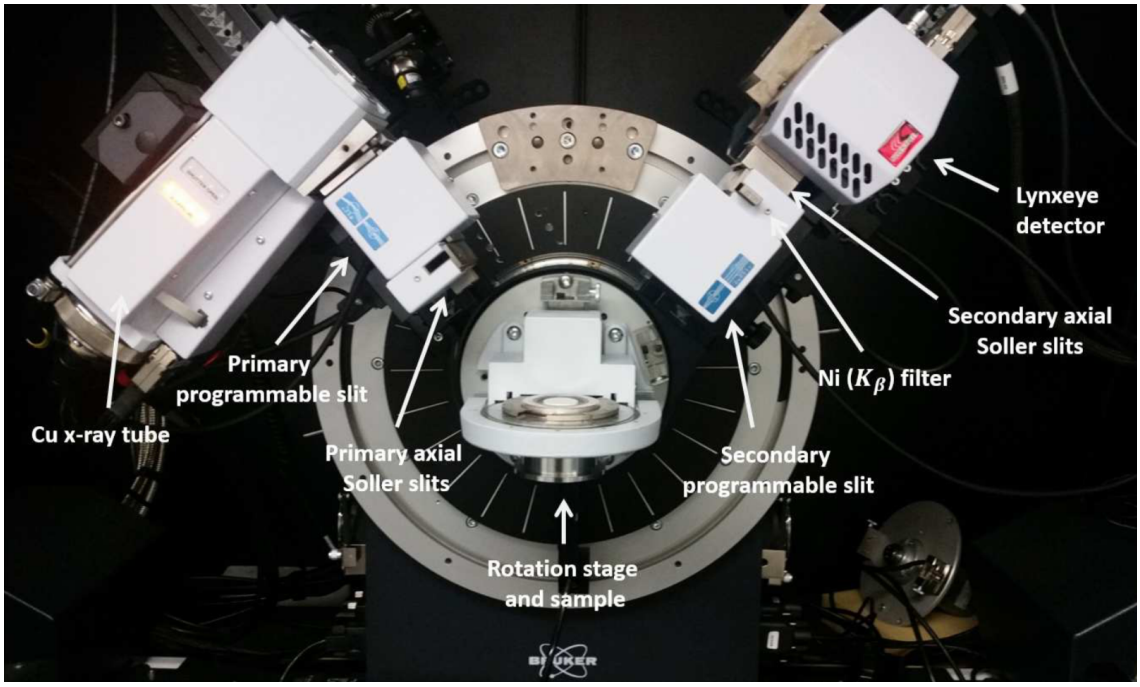

Figure 2.2: Bruker D8 DaVinci diffractometer with rotation stage.

x-rays are then focused on the sample using the primary set of optics consisting of axial Soller and programmable slits. The Soller slits minimize the axial divergence through collimation of the x-ray beam, while the programmable slits control the equatorial divergence of the beam across the sample length. A secondary set of optics then refocus the diffracted x-rays into the Lynxeye 1D detector. A Ni-K_β filter is used to attenuate the Cu-K_β and Bremsstrahlung radiation.

2.3 Electron Microscopy

Electron microscopy techniques can provide very high-magnification images by utilizing the wave-like properties of electrons through the de Broglie relation:

$$\lambda = \frac{h}{p} = \frac{h}{m_e v} \tag{2.3}$$

where h is Planck's constant, p is the momentum of the electrons, m_e is the mass of the electron, and where the wavelength λ influenced by the velocity v of the electrons. Transmission electron microscopy (TEM) is a technique involving the transmission and diffraction of electrons within an associated material. With an accelerating potential of $\geq$ 50 keV the wavelength of the electrons shrink to 5 pm with a penetration depth on the order of several microns[54]. Due to the transmission of electrons through the sample, the contrast of a TEM image is related to the thickness and atomic number Z of the ions in the material. The electron beam is focused by electric and magnetic fields onto a sample enabling imaging into the low nanoscale regime (several nm). Figure 2.3 a) shows a schematic of the principle behind TEM. The anode accelerates the electrons, while the condenser lens focuses the electrons onto the sample. The transmitted electrons then pass through multiple lenses focusing the sample onto the viewing screen or CCD. Using high-magnification TEM it is possible to obtain the spacing of the crystal planes where the lattice fringes are visible as equally spaced, recurring, dark fringes in the TEM image. Due to the contrast of the TEM image, one can also perform a fast Fourier transform (FFT) of the image that contains lattice fringes to extract information about the lattice symmetry of the material. The points in the FFT of an image are related to the plane separation,

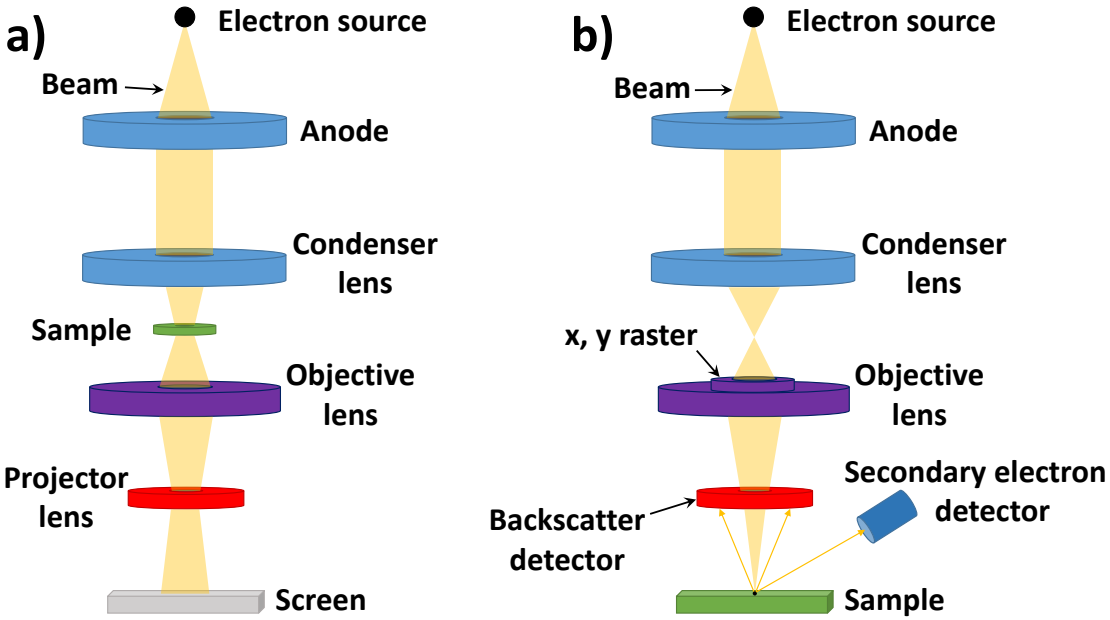

Figure 2.3: Diagram showing a) transmission electron microscopy (TEM) and b) scanning electron microscopy (SEM).

allowing us to extract the Miller indices of the visible planes.

Scanning electron microscopy (SEM) differs from TEM by using the secondary electrons that are emitted as a result of interactions with the atomic electrons within the sample. By using a raster technique (scanning in two perpendicular directions) with a highly focused electron beam, secondary (and back-scattered) electrons can be used to create an image of the sample (these features are illustrated in figure 2.3 b). The raster technique is required due to the wide range in energies of the emitted secondary electrons[54]. This technique allows imaging of thicker samples, but does not provide the atomic Z or thickness contrast that is present from the primary electrons in TEM.

TEM samples were prepared by suspending the nanoparticles in methanol and

dropped onto a 200-mesh carbon-coated copper grid. For SEM measurements the nanoparticles are dropped on carbon tape. TEM images were collected on a FEI Talos F200X S/TEM while the SEM images were obtained using a FEI Nova NanoSEM 450 at the Manitoba Institute for Materials (MIM). The TEM and SEM were operated with accelerating voltages of 200 keV and 5 keV, respectively. ImageJ[55] was used for particle analysis including the shape and size distribution, lattice spacing, and FFTs of the images.

2.4 X-ray Spectroscopy

X-ray spectroscopy techniques such as L- and K-edge x-ray absorption spectroscopy (XAS) can provide element specific information about the local crystal structure including coordination, oxidation state, and hybridization with neighbouring ligands and cations. Techniques such as x-ray magnetic circular dichroism (XMCD) are invaluable in determining the local magnetic structure, aiding in identifying the prevailing magnetic interactions present between the cations, i.e. intermixing of the orbitals that give rise to different magnetic behaviour. The high energy monochromatic x-rays required for XAS and XMCD techniques demand the use of synchrotron sources. Still, these have proven vital in the determination of the crystal structure and its magnetic properties.

A photon that interacts with a material can either scatter off the associated electron densities or is directly absorbed by an individual core electron. For a given element the absorption process only occurs if the photon carries enough energy to promote the core electron to the continuum of states above the Fermi energy. This

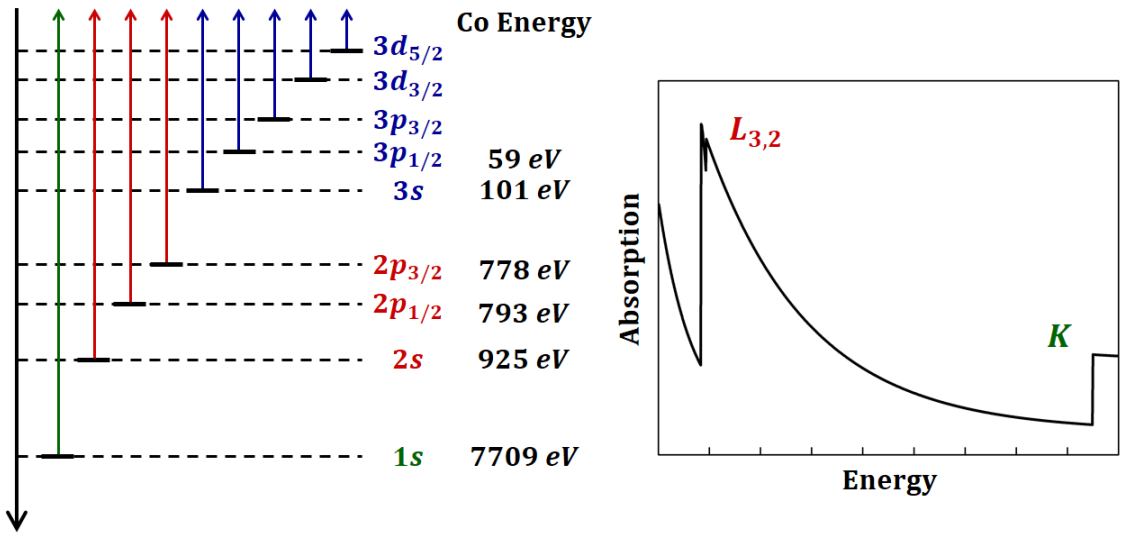

Figure 2.4: Diagram including labels and Co edge energies for various core-electron excitations. Also included is an illustration of the x-ray absorption, showing the L and K edges.

is shown in figure 2.4. The absorption coefficient ($\mu(E)$) is proportional to the initial and final states of the excited electron.

When the energy of the incoming photon is equal to the (edge) energy of a transition inside the material the absorption experiences a sharp rise where the process follows Fermi's Golden rule. For a transition from an initial state $|i\rangle$ with energy E_i to a final state $\langle f|$ with energy E_f, the transition probability W_{fi} is given by[56]:

$$W_{fi} = \frac{2\pi}{\hbar} |\langle f| T |i\rangle|^2 \delta(E_f - E_i - \hbar\omega) \tag{2.4}$$

where $\hbar\omega$ is the energy of the incoming x-ray and the transition matrix T can be expressed as:

$$T = \sum_q \hat{\epsilon}_q \cdot \mathbf{r} \tag{2.5}$$

which is known to be a familiar form of the x-ray absorption transition operator, where $\hat{\epsilon}_q$ denotes the polarization vector[57].

Soft (∼0.5 keV to 3 keV) and hard (∼3 keV to 50 keV) x-ray measurements were performed at beamline 4-ID-C and 20-BM-B at the Advanced Photon Source located within Argonne National Laboratory.

2.4.1 Soft X-ray Abosorption Spectroscopy

The absorption of the photon follows the dipole selection rules ($\Delta l = \pm 1$) thus in L-edge spectroscopy a core electron in the $2p$ state is excited into an available s or d state of higher energy, i.e. $4s$ and $3d$ for the first row of transition metal ions. XAS is an invaluable tool in studying the electronic structure of transition metal ions in oxide structures. The localized nature of the electrons implies both charge transfer effects and multiplet effects[56]. Charge transfer effects are described as the energy difference between occupations for the $3d$ states that result in large changes to the energies due to the core hole potential, while multiplet effects describe large $2p$-$3d$ two-electron integrals. Hybridization between the $3d$ transition metal and $2p$ oxygen orbitals leads to strong interactions for the final states that contain core holes. We gain the ability to describe the electronic structure using simulation techniques that encompass charge transfer multiplet theory[56; 57].

The x-ray absorption spectra can be simulated by using a model Hamiltonian that describes the perturbations to the atomic Hamiltonian $\mathcal{H}_{atom}$, with contributions from the crystal field $\mathcal{H}_{CF}$ affecting the degeneracy of the $3d$ orbitals and from the hybridization $\mathcal{H}_{Hyb}$ occurring between the O $2p$ and metal $3d$ and $4s$ orbitals[56; 57]:

$$\mathcal{H} = \mathcal{H}_{atom} + \mathcal{H}_{CF} + \mathcal{H}_{Hyb} \tag{2.6}$$

where the atomic Hamiltonian is given by[56; 57]:

$$\mathcal{H}_{atom} = \sum_i \frac{\mathbf{p}_i^2}{2m_e} - \sum_i \frac{Ze^2}{\mathbf{r}_i} + \sum_{pairs} \frac{e^2}{\mathbf{r}_{ij}} + \sum_i \zeta(\mathbf{r}_i)\mathbf{l}_i \cdot \mathbf{s}_i \tag{2.7}$$

and the indices i and j indicate the electrons in an ion, $\mathbf{p}_i$ is the momentum of the electrons, Z is the atomic number, $\mathbf{r}_i$ is the position vector of the electrons surrounding the nucleus, $\mathbf{r}_{ij} = |\mathbf{r}_i - \mathbf{r}_j|$ is the distance between electrons i and j and the sum is over pairs of electrons, $\zeta(\mathbf{r}_i)$ is proportional to the radial component of the potential related to the occupied orbitals, and $\mathbf{s}_i$ ($\mathbf{l}_i$) is the spin (orbital) momentum operator. The first term in $\mathcal{H}_{atom}$ represents the kinetic energy of the electrons, the subsequent two terms describe the Coulombic potential energies between the electrons and the nucleus and between electrons in the ion, and the last term is a result of the spin-orbit interaction.

The effect of the $2p$ spin-orbit interaction is very large for core holes and as a result it can be observed directly as a splitting of the L-edge XAS spectrum into the L_3 and L_2 edge, which represent the $2p_{3/2}$ and $2p_{1/2}$ transitions, respectively[56; 57]. The $3d$ spin-orbit interaction can reduce the symmetry of the ground state, but for the first row transition metal oxides the crystal field splitting dominates the spin-orbit interaction $\mathcal{H}_{CF} \gg \mathcal{H}_{SO}$ and thus certain transition metal compounds have a quenched orbital angular momentum ($\mathbf{l} = 0$)[14].

First-row transition metal ions contain five degenerate d-orbitals. Inside of a crystal field these orbitals split in energy. For an octahedral crystal field the d-orbitals are split into the lower t_{2g} orbital containing the off-axis d_{xy}, d_{yz}, d_{xz} orbitals while the e_g orbitals which lie along the coordination direction d_{z^2} and $d_{x^2-y^2}$ are pushed higher in energy. In tetrahedral coordination the opposite occurs due to the

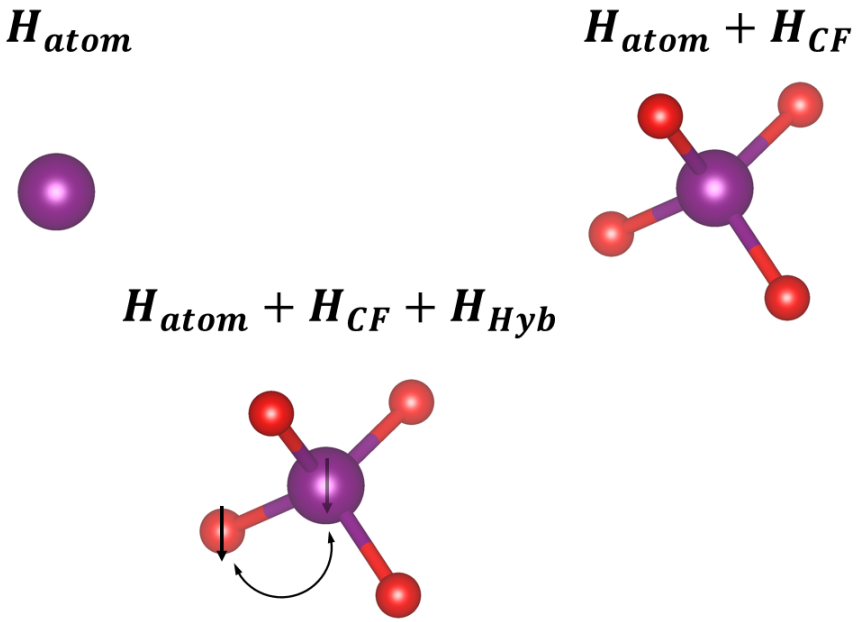

Figure 2.5: Illustration of the effect of each of the terms in the Hamiltonian described by equation 2.6.

off-axis bonding in the tetrahedral structure. The t_2 orbitals are pushed higher in energy. The loss of degeneracy is an important point when regarding XAS as this has an affect on the initial ground state and the final excited state of an electron in a $3d$ orbital. The crystal field Hamiltonian is simply a sum of the electron wavefunctions surrounding the $3d$ orbitals[57]:

$$\mathcal{H}_{CF} = -e\Phi(\mathbf{r}) = -e\sum_{l=0}^{\infty}\sum_{m=-l}^{l}\mathbf{r}^l A_{lm} Y_l^m(\theta,\ \phi) \tag{2.8}$$

where $\Phi(\mathbf{r})$ is the potential caused by the surrounding electrons and is given as a series written in terms of the spherical harmonics $Y_l^m(\theta,\ \phi)$ and a constant A_{lm}, where m is the magnetic quantum number.

For certain transition metal ions in the soft x-ray region the ligand $2p$ core orbitals interact very strongly with the $3d$ states due to covalency. It becomes necessary to

include the effects of hybridization and charge transfer that occur in the solid. The initial state of a $3d$ electron before the absorption can be represented by $|3d^n\rangle$, or for the initial state including charge transfer $|3d^{n+1}\underline{L}\rangle$ and the final states after absorption $|2p^5 3d^{n+1}\rangle$ including a charge transfer final state $|2p^5 3d^{n+2}\underline{L}\rangle$. The two initial and final states are coupled via hybridization (charge transfer)[56]:

$$M_I = \langle 3d^n | \, \mathcal{H}_{Hyb} \, |3d^{n+1}\underline{L}\rangle \tag{2.9}$$

$$M_F = \langle 2p^5 3d^{n+1} | \, \mathcal{H}_{Hyb} \, |2p^5 3d^{n+2}\underline{L}\rangle \tag{2.10}$$

where M_I and M_F are the contributions to the initial and final energy that arise due to hybridization between the ligand $2p$ and metal $3d$ states $\mathcal{H}_{Hyb}$ is given by[56]:

$$\mathcal{H}_{Hyb} = \sum_{\Gamma\sigma} V(\Gamma)(a^\dagger_{d\Gamma\sigma} a_{\Gamma\sigma} + a^\dagger_{\Gamma\sigma} a_{d\Gamma\sigma}) \tag{2.11}$$

where $V(\Gamma)$ is the hybridization between $3d$ metal and $2p$ ligand states. $a^\dagger_{\Gamma\sigma}$ ($a_{\Gamma\sigma}$) are the creation (annihilation) operators for electrons in a ligand molecular orbital Γ with spin σ and $a^\dagger_{d\Gamma\sigma}$ ($a_{d\Gamma\sigma}$) are the creation (annihilation) operators of a similar $3d$ state (Γ, σ), and the combination of $a^\dagger_{d\Gamma\sigma} a_{\Gamma\sigma}$ represents an electron hopping from a ligand (Γ, σ) orbital to a $3d$ (Γ, σ) orbital.

The three terms in equation 2.6 describe the atomic energy transitions with various perturbations that include splitting due to the crystal field, and multiplet effects from hybridization and charge transfer. An illustration of the effects of the perturbations to the Hamiltonian $\mathcal{H}_{atom}$ are represented in figure 2.5.

O K edge XAS ($1s \rightarrow 2p$) occurs at an energy of 530 eV, in the regime of soft x-ray spectroscopy, thus we have the ability probe the ligand ions. Intermediate oxygen ions are responsible for the magnetism and exchange interactions within the

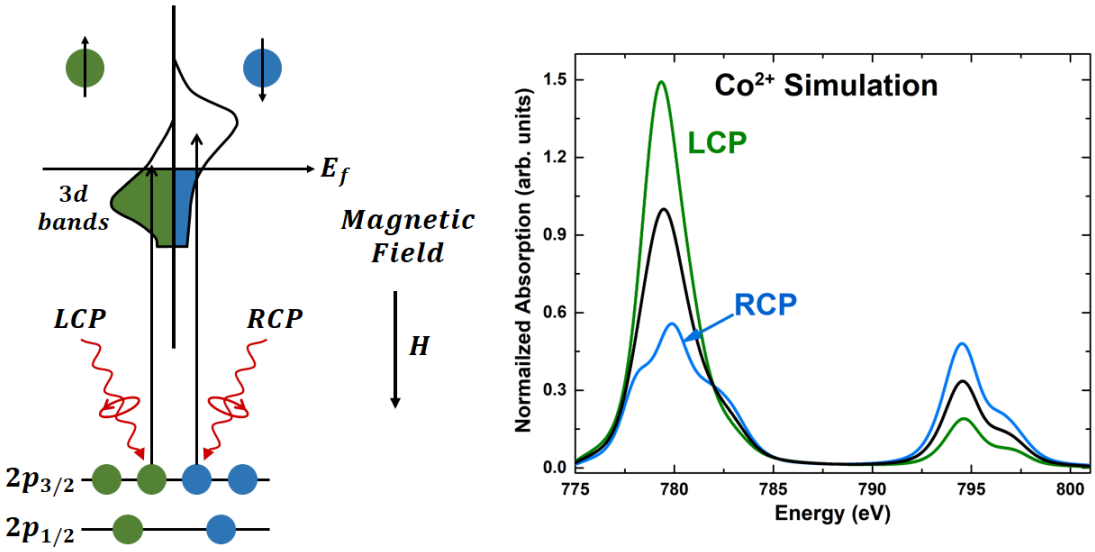

Figure 2.6: Illustration of the XMCD process with the resultant absorption for the right (RCP) and left (LCP) circular polarized x-rays showing the difference in spin occupation.

transition metal oxides. This is due to the partial delocalization of the $2p$ electrons that hybridize with the $3d$ orbitals. This hybridization of metal $3d$ states with the final $2p$ state of the oxygen ligand results in a splitting in the low energy peak arising from vacancies in the $3d$ e_g and t_{2g} orbitals[58]. At higher energy in the O K edge XAS the spectrum is dominated by contributions from p states on the oxygen ion hybridize with metal $4s$ and $4p$ states[58].

Circularly polarized x-rays can be used as an element specific probe into the magnetic structure of the material. X-rays can interact differently with electrons based on the polarization of the incoming photons. This was shown in equation 2.5 where the dipole transition operator T is dependent on the polarization vector of the incoming x-ray; this is shown in figure 2.6. For circularly polarized light the

polarization vector can be expressed as:

$$\hat{\epsilon}_R = \frac{1}{\sqrt{2}}(\hat{\epsilon}_x + i\hat{\epsilon}_y) \ , \quad \hat{\epsilon}_L = \frac{1}{\sqrt{2}}(\hat{\epsilon}_x - i\hat{\epsilon}_y) \tag{2.12}$$

where $\hat{\epsilon}_R$ ($\hat{\epsilon}_L$) identify right (left) circularly polarized x-rays that carry momentum $+\hbar$ ($-\hbar$). For light with right circular polarization (RCP) $\hat{\epsilon}$ rotates to the right when looking in the direction of propagation, and left circularly polarized (LCP) light has a polarization vector that rotates to the left. The dipole transition operator for RCP and LCP light can then be expressed as:

$$T_{\pm} = x \pm iy = \mp r\sqrt{\frac{4\pi}{3}}Y_1^{\pm 1} \tag{2.13}$$

where T_+ represents the transition operator for RCP x-rays and T_- indicates the transition for LCP x-rays. Equation 2.13 is obtained through the use of a vector $\mathbf{r} = x\hat{\epsilon}_x + y\hat{\epsilon}_y + z\hat{\epsilon}_z$ describing the position of the electron and introducing spherical harmonics. Equation 2.13 reflects the change in angular momentum ($\Delta\mathbf{l} = 1$) and the change in the magnetic quantum number ($\Delta m = \pm 1$) for the different polarizations of x-rays which affects the spin through the spin-orbit interaction. RCP and LCP x-rays show a difference in absorption for spin up and spin down electrons. This allows us to probe the magnetism of the $3d$ orbitals via the excitation-to-hole spin up and spin down states, i.e. the hole state magnetization is proportional to the actual magnetic moment determined by the unpaired electrons in the $3d$ orbital. The x-ray magnetic dichroic signal ($\Delta\mu$) is defined as the difference of the absorption coefficients obtained from RCP (μ_R) and LCP (μ_L) spectra obtained with equations 2.13 and 2.4 (Fermi's Golden rule) giving:

$$\Delta\mu = \frac{\mu_R - \mu_L}{\mu_R + \mu_L} \tag{2.14}$$

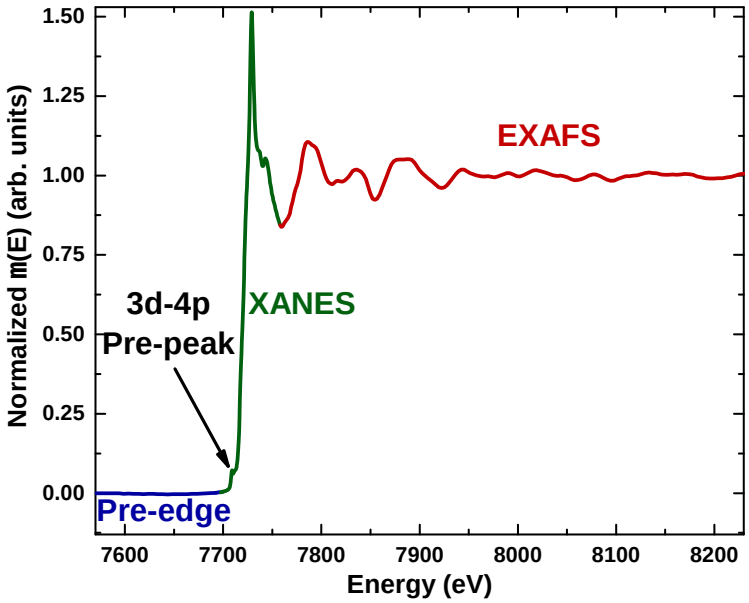

Figure 2.7: K edge XAS showing the different regions regions of a spectrum. Pre-edge and post-edge subtractions are performed, and the edge jump of the spectrum is normalized to one.

where by convention we normalized the XMCD to the XAS obtained from $\mu = \mu_R + \mu_L$.

To eliminate artefacts that arise from the saturation of the total electron yield (TEY) detector, XMCD is collected in both positive and negative applied fields. This ensures that the spin populations observed through XMCD flip with the reversal of the magnetic field. The resultant XMCD spectrum obtained by performing a subtraction of spectra obtained in both positive and negative fields is known as the artefact-free (AF) XMCD ($\Delta\mu_{AF}$):

$$\Delta\mu_{AF} = \frac{\Delta\mu_+ - \Delta\mu_-}{2} \tag{2.15}$$

where $\Delta\mu_+$ ($\Delta\mu_-$) is the XMCD obtained in positive (negative) applied fields.

2.4.2 Hard X-ray Abosorption Spectroscopy

Hard x-rays are used to probe the transition metal K-edge which excites a $1s$ core electron into an empty $4p$ state or a p state of higher energy. Because the life-time of a $1s$ core hole is very short, this broadening leads to intrinsically poor experimental resolution and this allows us to characterize transition metal K-edge spectra by single electron excitation models[56]. Small hybridization (multiplet) effects are only present for the $1s$ to $4p$ transition where hybridization between the $3d$ and $4p$ orbitals of the metal ion result in the small pre-peak in the XANES[59]. XAS spectra in the hard x-ray region contain two separate regions: 1) The x-ray absorption near-edge structure (XANES) which extends ∼50 eV above the edge energy, and 2) The extended x-ray absorption fine structure (EXAFS) extending up to ∼1 keV above the edge energy (figure 2.7). EXAFS describes a multi-scattering process between the absorbing atom, the photoelectron, and neighbouring atoms. These scattering processes undergo constructive and destructive interference with one another and this results in the fine structure observed above the K-edge for the transition metals.

K-edge XANES and EXAFS was performed on the Cu-doped Co_3O_4 over the Co and Cu edges which occur at 7709 eV and 8979 eV, respectively. EXAFS spectra were measured ∼1000 eV above the edge energy. Due to the large quantity of Co in the structure Co K-edge spectra were measured in transmission geometry, while Cu K-edge measurements were performed with florescence geometry due to the low amount of Cu within the materials. Spectra are analyzed using Athena and Artemis data analysis software[60]. Normalization includes a linear subtraction of the pre-edge background and a spline function is used to remove the post-edge background of

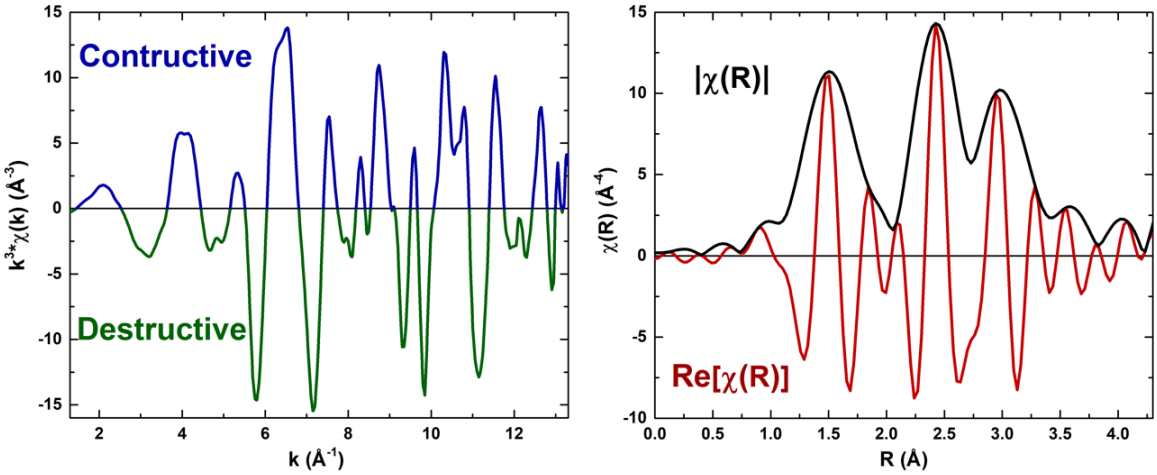

Figure 2.8: Left: The constructive and destructive interference of the scattered photo electrons weighted by the wave vector k^3. Right: Fourier transform of the k-weighted $\chi(k)$ spectrum showing the positions of the first three coordination shells.

$\mu(E)$. The edge jump of the spectrum is subsequently normalized (figure 2.7). The EXAFS equation describes the oscillations of the normalized absorption $\chi_i(k)$ for a given path i[57; 59]:

$$\chi_i(k) = \frac{\mu - \mu_0}{\mu_0} = \frac{N_i S_0^2 F_i(k)}{kR_i^2} e^{-2R_i/\Lambda} e^{-2k^2\sigma_i^2} \sin\left(2k_i R_i + \delta_i\right) \tag{2.16}$$

where the absorption coefficient of the material $\mu(E)$ is normalized to the absorption coefficient of an isolated absorber $\mu_0(E)$ and the wave vector k of the photo electron is obtained from the energy (E) of the incoming x-ray photon $k^2 = 2m_e(E - E_0)/\hbar$ with E_0 as the edge energy and m_e is the mass of the electron. R_i is the calculated path length obtained from $R_i = R_0 + \Delta R$. The parameters $F_i(k)$ are the effective scattering amplitude, Λ the mean free path length, $\delta(k)$ the effective scattering phase shift, and R_0 the initial path length are calculated by the FEFF software[61] utilized by Artemis[60] and generated from crystallography information files (CIF) obtained

from XRD. N_i the degeneracy of the paths, S_0 the scattering amplitude, ΔR the change in path length, and σ^2 the mean squared displacement (Debye-Waller effects) are all fit parameters in the Artemis program.

The left side of figure 2.8 shows the oscillations described by $\chi(k)$. After an electron is promoted out of the core state, constructive and destructive interference of the photo electrons can occur after undergoing multiple scattering processes with the neighbouring shells. For single scattering paths this describes the process of an electron scattering off of a neighbouring coordination shell and returning to the original absorbing atom. Typically, $\chi(k)$ is weighted by the wave vector k in the form k, k^2, or k^3 to amplify oscillations at different parts in the spectrum where a higher value of k-weight amplifies oscillations higher in k value. To relate the observed oscillations in the absorption, $\chi(k)$, to the associated crystal structure, a Fourier transform is applied to the normalized $\chi(k)$ to obtain the real and imaginary parts. The magnitude $|\chi(R)|$ describes the real-space distribution of coordination shells (figure 2.8) that results in the interference pattern of $\chi(k)$. To eliminate unphysical contributions, a rectangular window with tapered sides is used to fit only a specific region (roughly 1 - 3.5 Å).

2.5 Magnetometry and Susceptometry

The overall magnetic properties were determined using a superconducting quantum interference device (SQUID) magnetic property measurement system (MPMS-XL) from Quantum Design. The main components of the magnetometer are submerged in liquid helium and consist of a 5 T superconducting magnet, the superconduct-

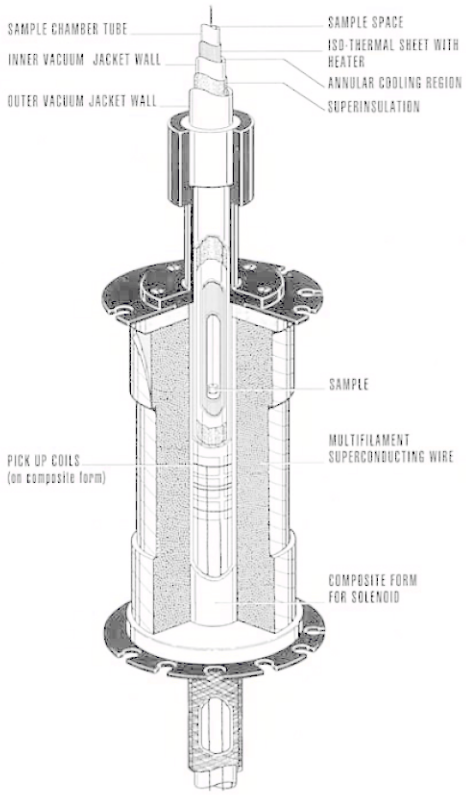

Figure 2.9: Schematic of the sample space housing, superconducting magnet, and detection coils[1].

ing detection coils, and the SQUID itself that includes a superconducting shield to ensure isolation from the large magnetic fields within the sample space of the dewar. A schematic diagram of the sample space housing, pick-up (detection) coils, and the superconducting magnet are shown in figure 2.9. The superconducting magnet is a solenoid capable of producing magnetic fields up to 5 T. The superconducting detection coils represent the configuration of a second-order (second-derivative) gradiometer to eliminate changes in the current under constant applied field and linear field gradients[1; 62]. As the sample is moved through the detection coils a change

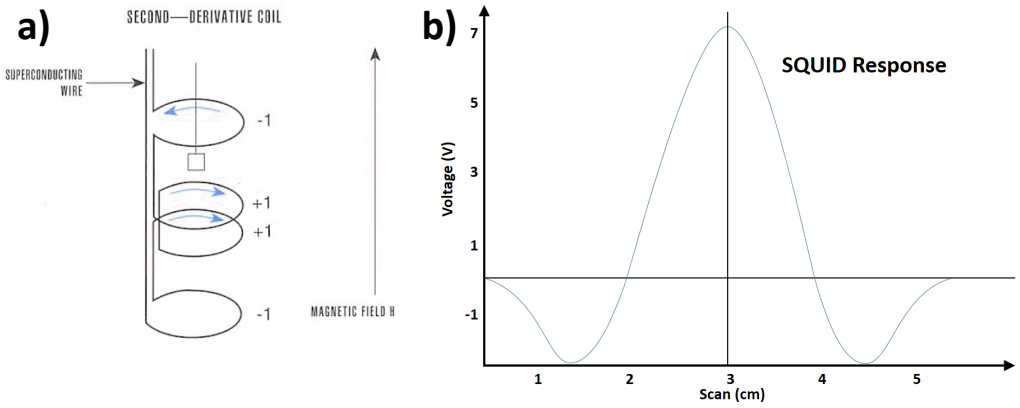

Figure 2.10: a) The superconducting detection coils are shown in the configuration of a second-order (derivative) gradiometer. b) The voltage response of the SQUID as the sample is moved through the coils[1].

in the magnetic field induces a change in the current flowing through the coils. The SQUID consists of two Josephson junctions that convert the change in current from the detection coils into an output voltage vs. sample position (z). A dipole is then fit to the output voltage, to obtain the associated magnetization. The detection coils and the response of the SQUID as the sample is moved through the gradiometer is shown in figure 2.10.

DC susceptibility χ_{DC} was obtained under zero field cooled (ZFC) and field cooled (FC) conditions from 2 - 300 K for all samples in a small applied field of 10 mT. To eliminate residual magnetic fields in the magnet from previous measurements a magnet reset and shield degauss are performed before the measurements.

ZFC hysteresis loops were obtained for all of the shapes while FC $M(\mu_0 H)$ loops were performed on the Cu-doped samples to investigate the effects of ferro- and antiferromagnetic couplings. The magnetization M is measured as a function of applied magnetic field, $\mu_0 H$, for temperatures between 2 - 300 K. From $M(\mu_0 H)$

measurements we can acquire characteristic magnetic properties of the samples such as the saturation magnetization (M_s), coercivity (H_c), and exchange bias (H_{ex}).

All measurements were performed using the RSO transport which moves the sample in the (z) direction through the magnetic field in a slowly oscillating manner to improve the signal-to-noise ratio. The sample space maintained at low pressure filled with helium gas. Temperature was controlled by varying the vapour pressure above the liquid helium and heater power adjacent to the sample, allowing for precise control of heating and cooling. Measurements were performed on powder samples mounted in a supracil quartz tube to ensure a uniform, near-zero background.

Chapter 3

Co_3O_4 Nanoshapes

3.1 Introduction

For nanoparticles the surface often plays a major role in deciding the overall magnetic properties. The exchange interactions that occur at the surface are exquisitely sensitive to the nature of the bonding and environment thus providing a quantitative measure of the surface interactions. The antiferromagnetic nature of Co_3O_4 results in the low magnetization from the core of the particles allowing us to obtain an accurate representation of the surface and revealing competition between ferro- and antiferromagnetic interactions.

As mentioned previously, the exchange interactions in Co_3O_4 occur between two magnetic Co^{2+} ions located at the T_d sites. The interactions responsible for the antiferromagnetic order result from exchange through the non-magnetic Co^{3+} ion. The different shapes of Co_3O_4 nanoparticles present different surface terminations that contain different bonding environments and numbers of cations. By characterizing the environments and exchange interactions for the different surface terminations, we

can obtain a direct correlation to the magnetic properties observed. The magnetism provides a novel method to aid in quantifying the exchange interactions at the surface. Competition between ferro- and antiferromagnetic order produce a wide range of magnetic behaviour, from an antiferromagnetic spin-flop to weak ferromagnetic behaviour at the surface.

3.2 Structure and Surface of the Nanoshapes

Transmission electron microscopy (TEM) and scanning electron microscopy (SEM) were performed to obtain the shape, size, and size distributions for the different particles. Typical TEM images for the different shapes are shown in Fig. 3.1, where the spheres have a diameter of 10 nm, the cubes have an average side length of 15 nm, and the hexagonal plates are 70 nm across with a thickness of 8 nm. The inset of Fig. 3.1 a) shows a cube with visible lattice planes (022) and $(0\bar{2}2)$ spaced a distance of 0.28 nm and occurring with an angle of 90° between them[8; 63–65]. The fast Fourier transform (FFT) is shown in the top-left corner of the inset where the lattice planes are reconstructed in the Fourier (frequency) domain i.e. reciprocal lattice planes. Bright spots in the FFT correspond to specific planes. For the cubes, there are two different four-fold symmetric rotations present in the FFT indicating a 90° degree angle between the visible planes[8; 63–65]. The (022) and $(0\bar{2}2)$ planes are perpendicular to the {100} family of planes exposed at the surface.

Fig 3.1 b) shows high magnification images of the plates, where we find that the plates are textured with domains of roughly 7-8 nm. The inset shows the $(2\bar{2}0)$ and $(\bar{2}02)$ planes with an angle of 60° between them[8; 9; 64; 65]. Successive planes occur

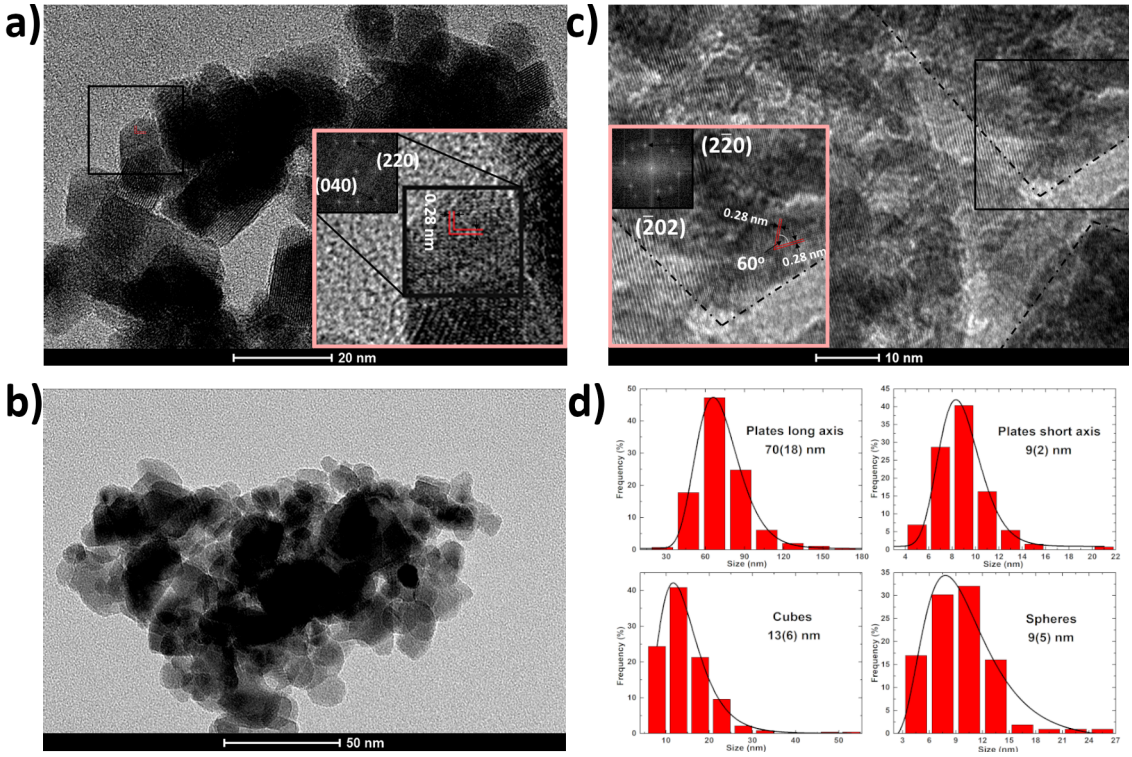

Figure 3.1: a) TEM image of the cubes. The inset shows planes at a 90° angle to one another, their separation distance, and the FFT. b) TEM image of the spheres is shown. c) TEM image of the plates. The inset shows planes with a 60° angle, distance between successive planes, and the FFT. d) Size distributions for each of the shapes from both TEM and SEM images.

with a distance of 0.28 nm. The planes (2$\bar{2}$0) and ($\bar{2}$02) are perpendicular to the (111) plane. The FFT displays a six-fold symmetry along with two different two-fold symmetric rotations, this is due to the different positions of the atoms nearby and representative of the (111) plane with hexagonal geometry (i.e. 60° rotation symmetry)[8; 9; 64; 65]. It has also been established from surveys that Co_3O_4 with the cubic spinel structure exposes the (100) plane for cubes, and the (111) plane for hexagonal plates[8; 64; 65]. Fig. 3.1 d) shows the size distributions for the different shapes were fit with a lognormal function with the mean size and standard deviations

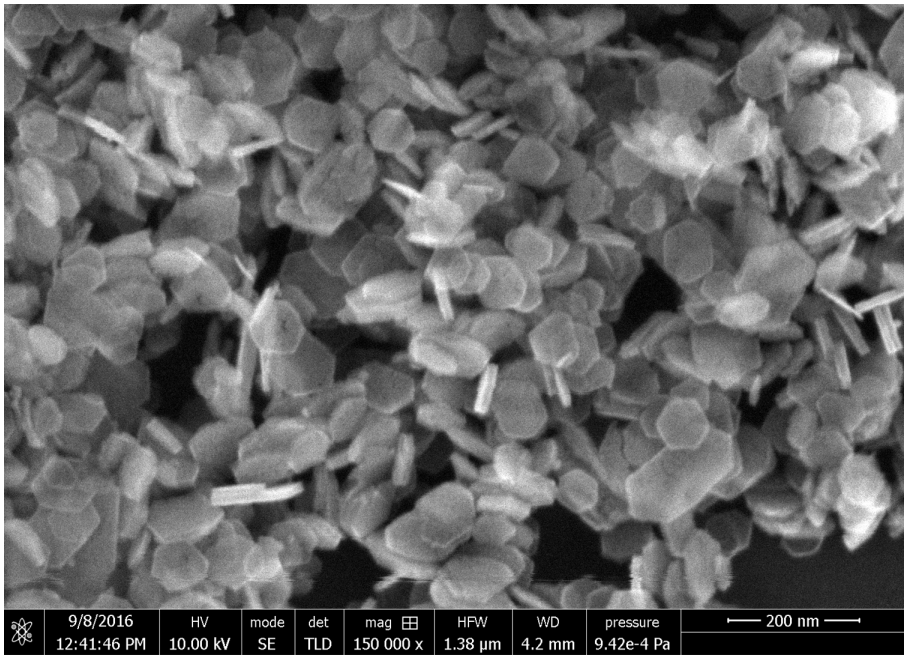

Figure 3.2: Typical SEM image for the plates, showing the small aspect ratio.

reported. Long and short axis characterizations for the hexagonal plates were done using lower magnification SEM images, shown in Fig. 3.2. The small aspect ratio of thickness to diameter is much more apparent, simplifying analysis of the particles.

X-ray diffraction (XRD) was used to characterize the crystal structure for each of the shapes, identifying the space group symmetry and occupancies of the cationic sites with characteristics of the unit cell and particle size. XRD was performed for all three shapes, presented in Fig. 3.3. Rietveld refinements were done in GSAS-II[66]. All patterns are phase pure Co_3O_4 with the expected space group $Fd\bar{3}m$. Occupancies were unchanged from the bulk values[20] indicating the usual normal spinel structure with 2+ ions located in tetrahedral and 3+ ions located in octahedral sites. From the refinements the crystallite size obtained for the spheres and cubes are 15(1) nm and

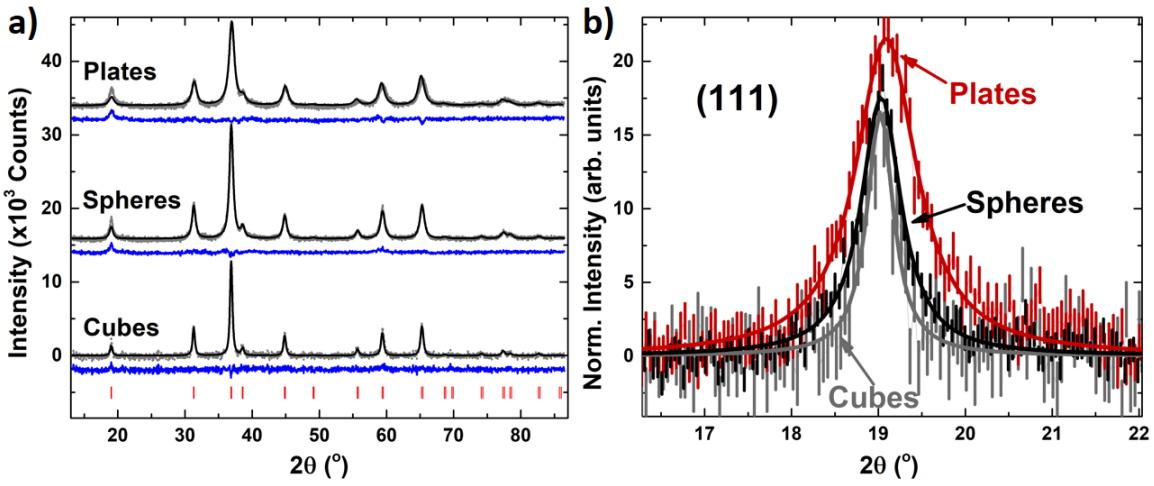

Figure 3.3: a) XRD patterns for the nanoshapes are shown along with fits (solid black lines), residuals (blue lines) and Bragg markers (red ticks) for the reflections obtained from Rietveld refinements. b) Normalized (111) reflection for the different shapes. Intensity difference for the plates results from preferred orientation.

25(1) nm, respectively. Both shapes have a crystallite size that matches the particle sizes obtained from TEM image analysis indicating the particles are composed of single crystallites. The plates are composed of many crystallites with a size of roughly 9(1) nm. The lattice constant for all the shapes obtained from refinement (spheres $a = 8.075$ Å, cubes $a = 8.078$ Å, and plates $a = 8.062$ Å) are close to the bulk value of 8.065(3) Å[20].

Preferred orientation was found for the plates along the (111) reflection. Since the preferred orientation is due to the surface planes of the hexagonal plates the magnitude is small and most easily seen through normalized XRD patterns. Normalizing all three XRD patterns to the largest peak (∼37°), we find only a differences for the reflections associated with the (111) direction (i.e. (111), (222), etc.). Normalized intensities for the (111) reflection are shown in Fig. 3.3 b) where the plates show an

Table 3.1: Co_3O_4 Surface Properties

Shape (Plane)	Surface area (m^2/g)	(111) Surface area (m^2/g)	Co^{2+}:Co^{3+} surface ratio
Spheres (100), (110), (111)	110.0	33.9	1.37:2
Cubes (100)	58.5	0.0	1:2
Plates (111)	25.0	20.2	1.75:2

increase in intensity relative to the other shapes. The increase of roughly 25% is due to preferred orientation. Solid lines are Lorentzian curves meant to guide the eye.

Using the software visualization for electronic and structural analysis (VESTA)[67], it is possible to simulate the different shapes with their respective surface planes to quantify the total surface area, the surface area of specific planes, and the Co^{2+}:Co^{3+} ratios of those planes. The Co^{2+}:Co^{3+} ratios obtained for the shapes are shown in Table 3.1 where the cubes display a Co^{2+}:Co^{3+} ratio that matches bulk Co_3O_4 (1:2). For the spherical particles there are no specific exposed planes, but consist of an average of three different families of planes: The {100}, {110}, and{111} planes. The {100} family contains six possible planes, while the {110} family has 12, and the {111} family incorporates eight planes into the average. Considering the Co^{2+}:Co^{3+} ratio for each of the planes, and assuming that each of the 26 total planes are exposed equally, we can formulate the average as follows:

$$\left[Co^{3+}\right]_{\text{sphere}} = \frac{1}{26}\left(6\left[Co^{3+}\right]_{100} + 12\left[Co^{3+}\right]_{110} + 8\left[Co^{3+}\right]_{111}\right) \tag{3.1}$$

where $\left[Co^{3+}\right]_{hkl}$ is the value of the Co^{3+}/Co^{2+} ratio that is normalized relative to the surface area of the different planes. For the cubes and plates, $\left[Co^{3+}\right]_{\text{cubes}} = \left[Co^{3+}\right]_{100}$

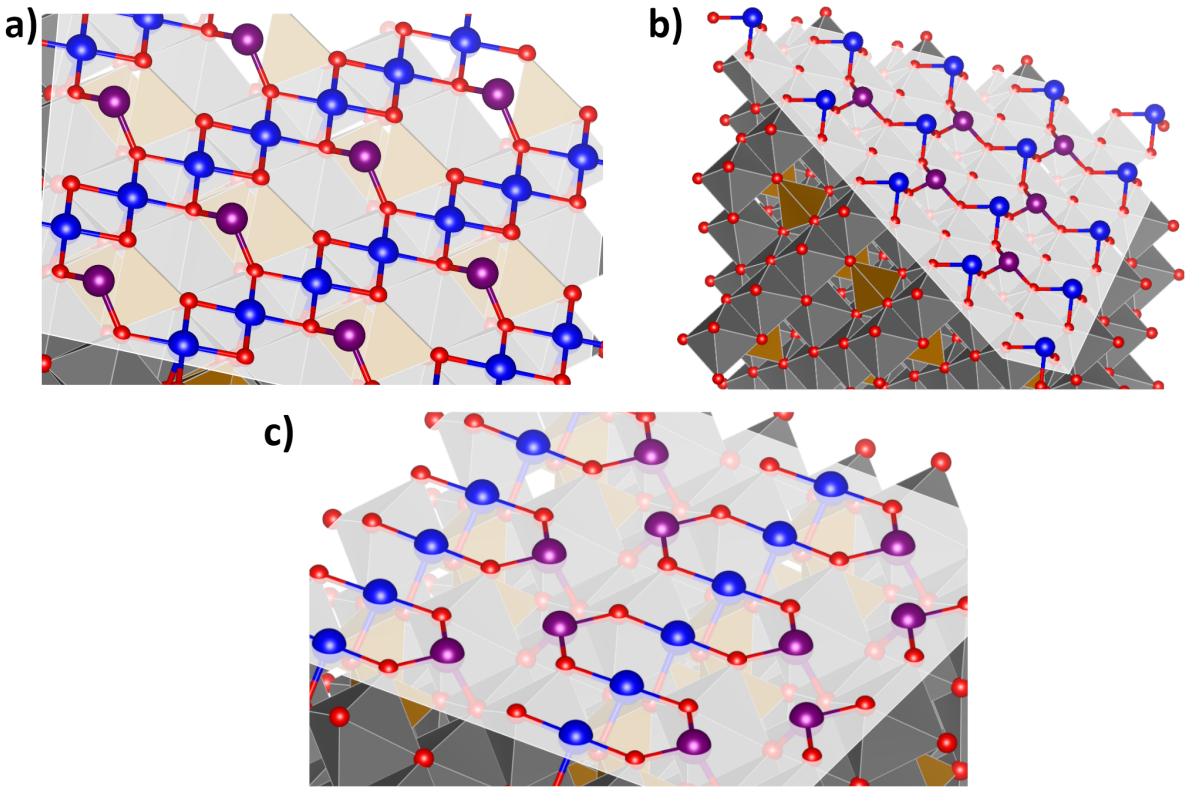

Figure 3.4: a) Illustration of the (100) surface plane of the cubes, b) (111) surface plane of the hexagonal plates, and c) (110) surface plane used in the average for the spheres. Co^{3+} ions are shown in blue (octahedral, gray), Co^{2+} ions are shown in purple (tetrahedral, gold), and oxygen ions are shown in red.

and $\left[Co^{3+}\right]_{\text{plates}} = \left[Co^{3+}\right]_{111}$ are the values found in Table 3.1.

The (100) surface of the cubes is shown in Fig. 3.4, where the Co^{2+} ions are two-fold coordinated and the Co^{3+} ions are five-fold coordinated in a planar structure. The (110) surface shown in Fig. 3.4 c) resembles the (100) plane, with Co^{2+} ions coordinated to three O ions, and Co^{3+} ions are coordinated with four O ions. Thus, the (100) and (110) contain higher overall coordinations for the surface ions. Examining the (111) surface in Fig. 3.4 we find the Co^{2+} and Co^{3+} ions are coordinated to O ions in a zig-zag like structure. Both Co^{2+} and Co^{3+} ions are three-fold coordinated

Table 3.2: Co_3O_4 Exposed Planes

Plane	Surface unit cell area (nm^2)	Co^{2+} in surface unit cell	Co^{3+} in surface unit cell	Co ions in probe depth volume
(100)	0.65	2	4	66
(110)	0.46	2	2	63
(111)	0.57	2	2	61

to the O ions.

As a way to correlate certain structural and magnetic properties, we look at the surface area for the (111) plane for the different shapes. The (111) plane is the primary exposed plane for the plates, while due to the nature of the spheres, a smaller (111) area is exposed per particle, but a larger overall area for the (111) plane. This is shown in Table 3.1, along with the total surface area (m^2/g) and the Co^{2+}:Co^{3+} ratio for the different surface terminations.

Information about the Co^{2+} and Co^{3+} environments are provided by x-ray absorption spectroscopy (XAS) across the Co $L_{3,2}$ edges (770-810 eV) and the O K edge (520-560 eV). XAS characterizes the partial density of states just above the occupied density of states (Fermi energy) that is influenced by hybridization due to the ligand orbitals. Thus, XAS allows us to identify the different ionic species, relative abundances, and their coordinations.

The Co $L_{3,2}$ edge were obtained at 10 K for each of the shapes using total electron yield (TEY) detection. Spectra are essentially the same for all three shapes and are typical of Co_3O_4 with a Co^{2+}:Co^{3+} ratio of 1:2 (Fig. 3.5)[68]. Although TEY mea-

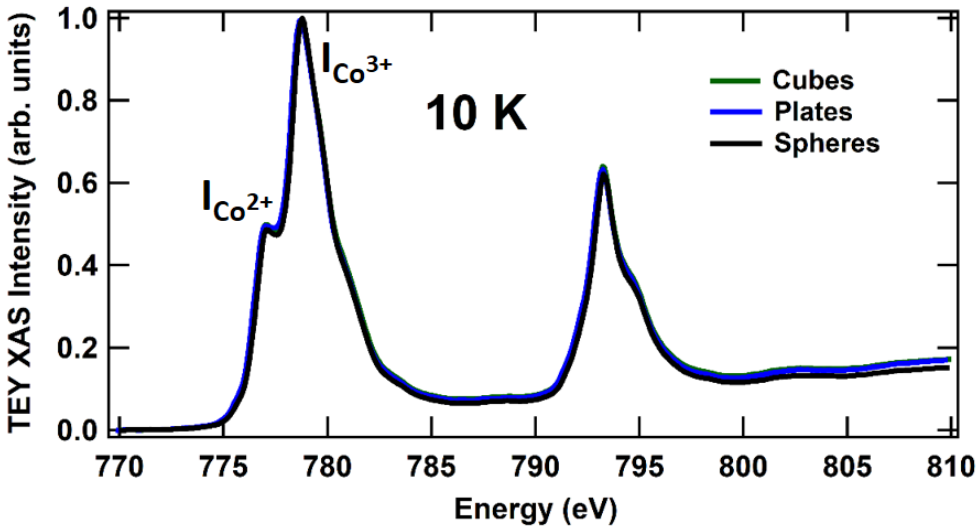

Figure 3.5: Co $L_{3,2}$ edge XAS spectra obtained at 10 K for all the shapes, where all three display the characteristic Co^{2+}:Co^{3+} ratio of 1:2.

surements are surface sensitive, the probe depth of only 2-3 nm for these $L_{3,2}$ energies results in, at most, a change in intensity of 2%[69]. The volume of a conventional unit cell in bulk Co_3O_4 is $V_{bulk} = (0.8065\ \text{nm})^3 = 0.53\ \text{nm}^3$. One unit cell contains 24 Co ions (16 Co^{3+} and 8 Co^{2+}) and taking the probe depth to be 2 nm we find, $\frac{2\ nm}{0.8065\ nm} \times 24$ Co ions = 60 Co ions in the volume of probe depth across a surface area of one unit cell. From VESTA we can obtain the surface unit cell area, the number of Co ions at the surface within the surface unit cell and the total number of ions for a probe depth of 2 nm for each of the three {100}, {110}, and {111} planes shown in Table 3.2. For the cubes we find that (6/66 = 0.09) 9% of the measurement is from surface Co ions, while for the plates with the (111) plane exposed we find 7% of the measurement originates from surface Co ions. Performing the same calculation for the (110) plane and using a weighted average to describe the spheres we determine the contribution to the measurement as 8.4%. Thus, between the shapes we only

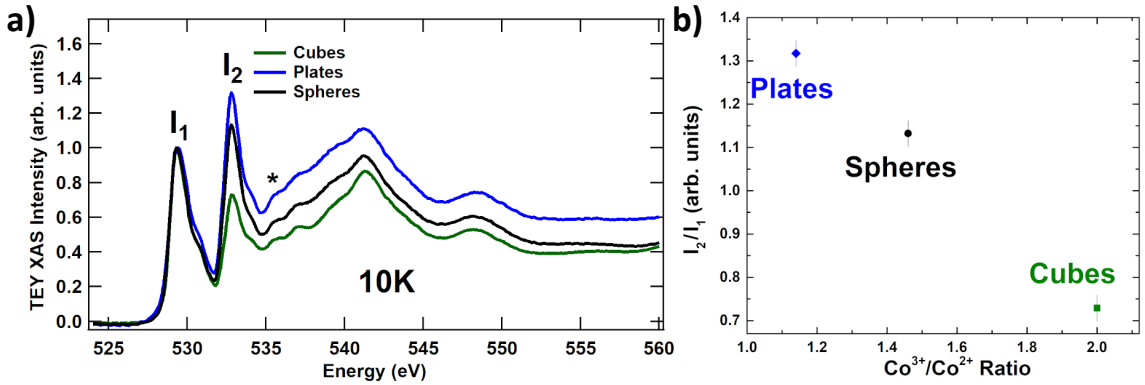

Figure 3.6: a) O K edge spectra taken at 10 K. The t_{2g} and e_g peaks are labelled I_1 and I_2, respectively. The asterisk marks the peak from oxygen on the carbon tape[2]. b) Variation of I_2/I_1 between the shapes, indicating the differences in Co^{3+} occupations at the surface.

expect an overall difference of ∼2%. A 3 nm probe depth would further decrease the overall surface contributions.

Consider a small but finite sized x-ray beam incident on powder samples, the beam must first interact with the surface of the particles and this means the same amount of surface is exposed for each sample; i.e. the XAS measurements cannot probe differences based on overall surface area (or particle size) in the samples. Thus differences must be specific to a given plane.

O K edge XAS probes the density of states for the ligand orbitals, quantifying hybridization with the metal $3d$ and $4s$ electronic states. K edge XAS for the different shapes is presented in Fig. 3.6 a). The region below 535 eV characterizes hybridization with the metal Co^{3+} $3d$ orbitals, via splitting of the major (spin up) and minor (spin down) e_g and t_{2g} states, in addition to present crystal fields[58]. The observed changes in the peak intensities at 530 eV and 533 eV quantify the number of $3d$ hole states (vacancies) available on the Co ion hybridized with the O ion. Thus, quantitatively,

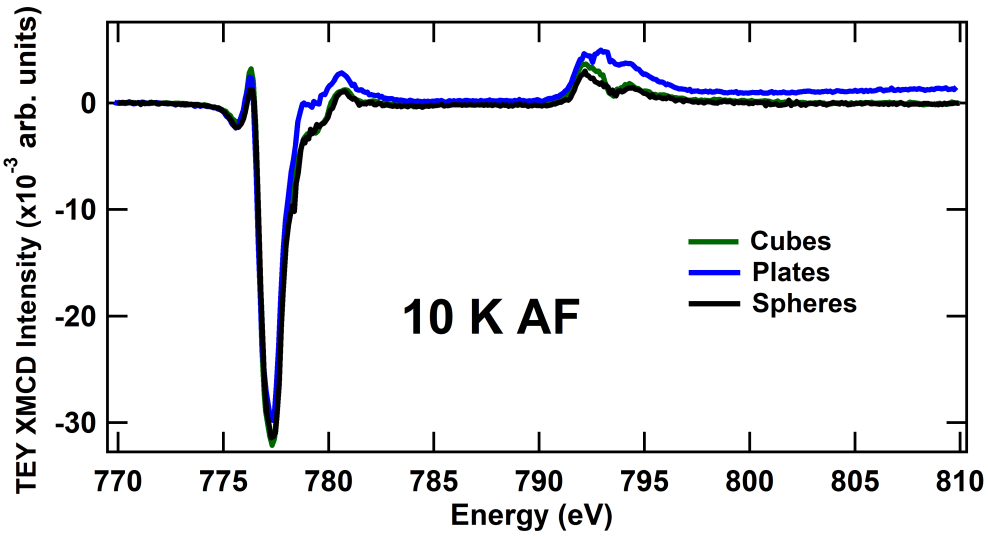

Figure 3.7: Co L edge XAS, normalized XMCD for all three shapes obtained at 10 K under applied fields of ±5 T using TEY detection. Small changes to the L_3 and L_2 edges are due to different Co^{3+} environments on the exposed surface planes.

the plates[1] have a higher number of available e_g/t_{2g} states on the Co^{3+} ion caused by the concomitant decrease in coordination at the surface.

The variation of I_2/I_1 vs the Co^{3+}/Co^{2+} ratio shown in Fig. 3.6 b) identifies the differences between the shapes, from the majority of oxygen ions at the surface; each Co ion is coordinated to three O ions resulting in a range of Co-O bond combinations. The changes in the O K edge XAS above 535 eV are correlated to the changes in the O $2p$ metal $4s$ hybridization. This is a result of the change in the bonding at the different surfaces. We find that the cubes show more defined peaks in the energy range of 537 eV to 545 eV indicating the stability of the (100) consistent with highly coordinated transition metal ions[8].

X-ray magnetic circular dichroism (XMCD) uses right and left circularly polarized

[1]Normalizing the XAS to the edge-jump changes the intensities of I_1 and I_2, but the trends remain the same between the shapes.

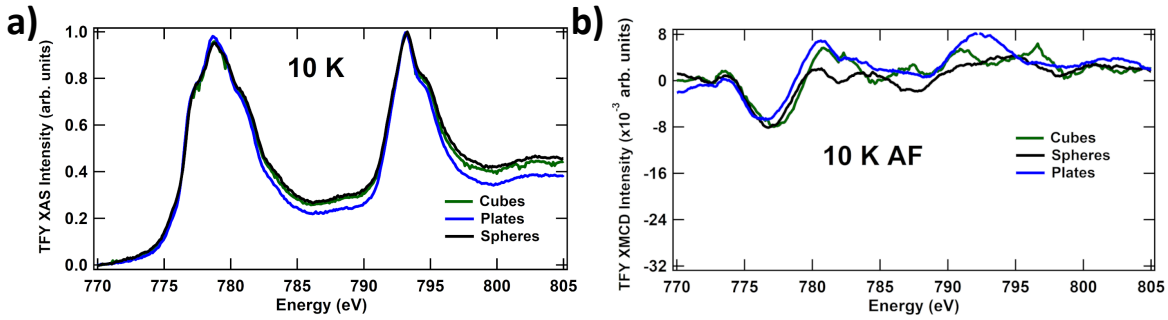

Figure 3.8: a) XAS and b) XMCD over the Co L edges for the different shapes obtained at 10 K using TFY detection. Where the XMCD shows no discernible signal.

light to measure both spin up and spin down populations, thus, an XMCD signal is not observable for antiferromagnets. The artefact-free (AF, see section 2.4.1) XMCD for the shapes are shown in Fig. 3.7 provides strong evidence for the presence of ferromagnetic behaviour at the surface of the nanoshapes. The differences of the XMCD spectra over the $L_{3,2}$ edges are due to the different Co^{3+} environments at the respective surfaces. A decrease in the coordination at the surface causes a change in the crystal field environments resulting in an additional magnetic moment on the surface of the (111) plane ascribed to the Co^{3+} ion. It should be noted that the XMCD signal only occurs for the TEY probe measurements. Total fluorescence yield (TFY) detection is bulk-sensitive and presents no observable XMCD signal. Fig. 3.8 a) and b) show the XAS and XMCD for the different shapes using TFY detection.

3.3 Magnetism of the Surface Terminations

To further explore the magnetic properties of the surface we can quantify the surroundings for the Co ions of the respective surface terminations using the differences

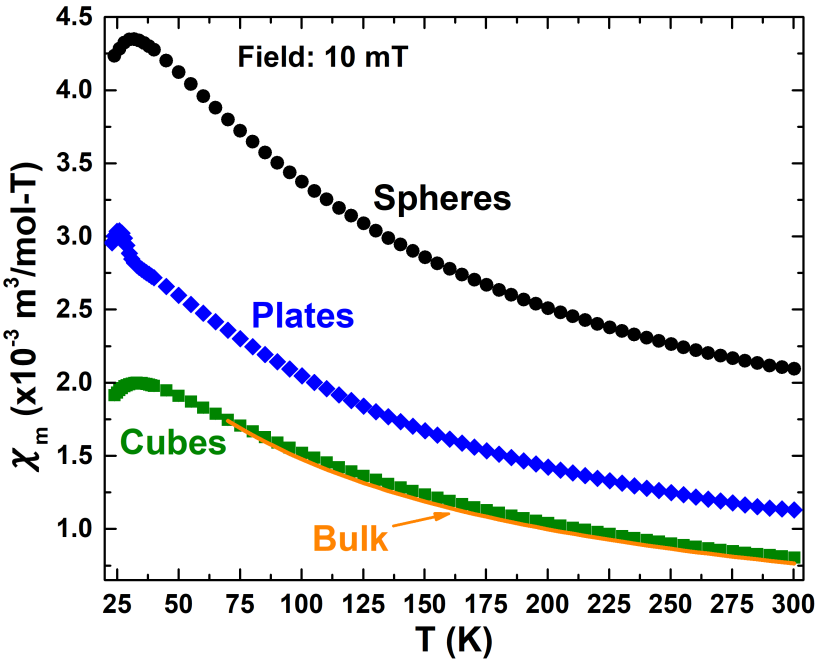

Figure 3.9: Molar susceptibility of the shapes from 20-300 K. The cubes show a susceptibility very similar to that of bulk, while the spheres and cubes display a much larger susceptibility.

in the overall magnetism. For example, the low-field susceptibility $\chi_{DC}(T)$ in Fig. 3.9 gives the ordering temperature and the magnetic moment per formula unit, which are both related to the exchange constant J_{ij} from equation 1.24. Bulk Co_3O_4 has an ordering (Néel) temperature of $T_N = 40$ K[20], where the shapes show variations in T_N; the spheres and cubes have a Néel temperatures of 31(1) K and 33(1) K, respectively, while the plates have $T_N = 25(1)$ K. T_N for the different shapes is obtained from the peak in the susceptibility, or when $d(\chi_{DC})/dT = 0$ (Fig. 3.11). Susceptibility of bulk Co_3O_4 is also shown in the figure to emphasize the similarity between the cubes.

Quantification of the magnetic moment is obtained through analysis of the inverse susceptibility $1/\chi_{DC}(T)$, where $\chi_{DC}(T)$ is represented by the modified Curie-Weiss

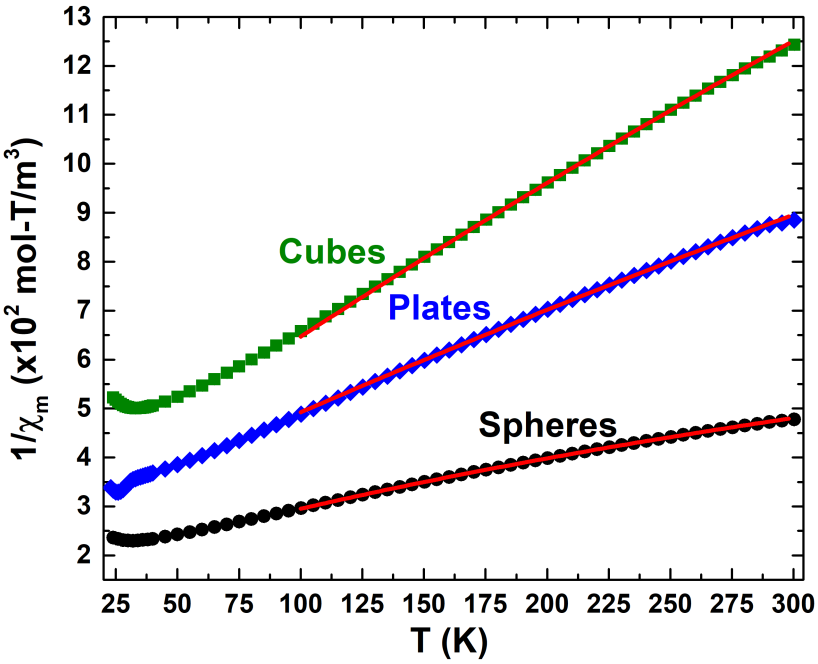

Figure 3.10: Inverse susceptibility for the different shapes with the fit shown in red. $1/\chi_{DC}(T)$ was fit in the high-temperature region of 170-280 K.

law described by equation 1.25, which includes the temperature independent component χ_0 (van Vleck paramgnetism) to the susceptibility. Fits of $1/\chi_{DC}(T)$ for the shapes are shown in Fig. 3.10, where values for the Curie constant C, the Weiss temperature θ, and the temperature independent component χ_0 are given in Table 3.3. Both Co^{2+} and Co^{3+} contribute to the temperature independent component χ_0 through van Vleck paramagnetism. It was found by Cossee that Co_3O_4 has a χ_0 of $\chi_0 = 0.9 \times 10^{-4}$ m^3/mol-T[17]. The different shapes show values close to the bulk value, and other reports[17; 70; 71].

θ the Weiss temperature is related to the exchange interactions within the shapes, where bulk values for θ range from -53 K to 110 K, and all three shapes have values of θ consistent with bulk values[20; 70–72]. μ_{eff} gives a quantitative measure of

the overall magnetic moment per formula unit. The effective magnetic moment is obtained through the Curie constant C:

$$\mu_{eff} = \sqrt{\frac{3k_B C}{n\mu_0}} \approx 2.83 \times \sqrt{C_{mol}} \tag{3.2}$$

where C_{mol} is the Curie constant in terms of moles of Co_3O_4 in CGS units i.e. $[C_{mol}] = \frac{\text{emu-K}}{\text{Oe-mol}}$. Both C and μ_{eff} are related to the surface terminations for the different shapes, C (and μ_{eff}) for the spheres is largest, followed by the plates then cubes. The effective moment at the (111) surface of the plates is larger than that of the (100) surface of the cubes, even though the latter is found to have a larger per particle surface area the cubes have a magnetic moment identical to the bulk value. The spheres expose the (100), (110) and (111) planes and it is through the correlation of the exposure of the (111) plane that the spheres obtain such a large effective moment, i.e. they have the largest surface area, leading to the largest exposure of the (111) plane.

T_N and μ_{eff} determined from DC susceptibility provide a quantitative measure of the exchange interactions J_{ij} from the surface (equation 1.24). For bulk Co_3O_4, with $T_N = 40$ K, four nearest neighbours ($z = 4$), and using the spin only value ($j = s = \frac{3}{2}$) for the total angular momentum, we obtain a value for the exchange $J_{ij} = 4.0$ K$/k_B$[20]. Due to the large crystal field splitting and small atomic number, the Co ions have quenched orbital angular momenta $l = 0$. For the shapes we do not use the spin-only value for $j(j+1)$, instead we obtain the total angular momentum from the effective magnetic moment using equation 1.12. This is to account for μ_{eff} shown to describe contributions from the surface spin magnetism[73]. Broken symmetry and low coordination at the surface provide the mechanism for unquenched

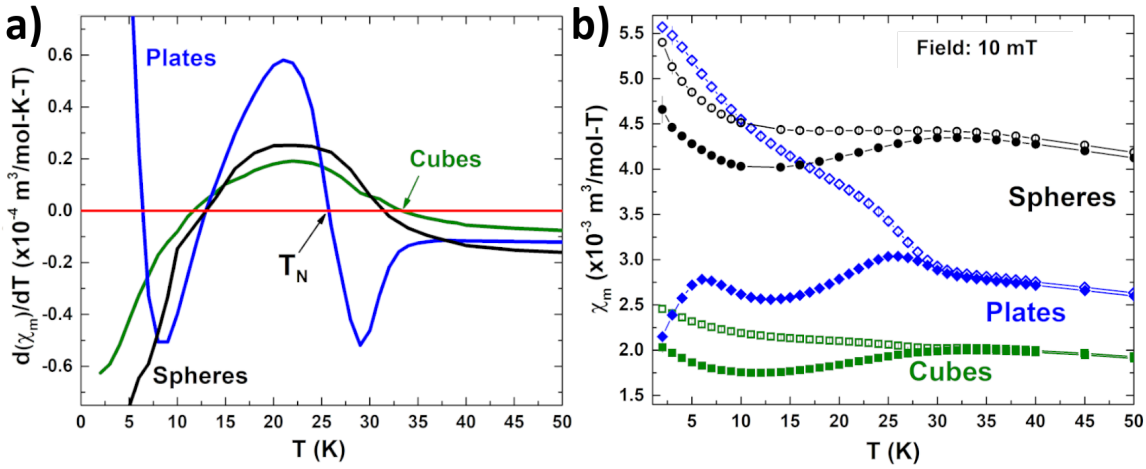

Figure 3.11: a) $d(\chi_{DC})/dT$ as a function of temperature for the different shapes. The Néel temperature T_N is given when $d(\chi_{DC})/dT = 0$. b) ZFC (closed symbols) and FC (open symbols) susceptibilities of the shapes from 2-50 K. The plates show the largest bifurcation, representative of weak ferro-/ferrimagnetic behaviour.

orbital angular momentum and the possibility of a small magnetic moment on the Co^{3+} ions[34; 74]. Values of the exchange constants for the different shapes are shown in Table 3.3. The exchange constant for the cubes is most similar to that of bulk Co_3O_4, while the plates have a smaller J_{ij} due to the larger value for the effective magnetic moment, and lower value for T_N. The spheres show the smallest overall exchange (largest magnetic moment) due to the large surface area, and (111) plane exposure. Interestingly, the value of C between the shapes correlates with the surface area for the (111) plane only. The (110) plane for the spheres contributes no magnetic moment, displaying behaviour similar to the (100) plane and bulk Co_3O_4.

Returning to the molar susceptibilities in Fig. 3.11 b) we can examine characteristics in the magnetism below T_N. The spheres and cubes display very similar behaviour

[2]Obtained by using $T_N = 40$ K and the spin-only value for the total angular momentum ($j = s = 3/2$).

Table 3.3: χ_{DC} Magnetic Properties

Shape	χ_0 (m^3/mol-T^{-1})	C (m^3-K/mol-T^{-1})	θ (K)	μ_{eff} (μ_B)	J_{ij} (K/k_B)
Spheres	$8(3)\times10^{-4}$	0.50(1)	-93(5)	5.7(2)	1.5(2)
Plates	$2(1)\times10^{-4}$	0.39(1)	-107(5)	5.0(2)	1.6(1)
Cubes	$1(1)\times10^{-4}$	0.26(5)	-83(5)	4.1(2)	3.0(1)
Bulk[70]-[72]	0.9×10^{-4}	0.26	-85	4.1	4.0[2]

in both zero field cooled ($\chi_{ZFC}(T)$) and field cooled ($\chi_{FC}(T)$) susceptibilities, both begin to increase below 12 K. This is a result of a reconfiguration of the spins at the surface of the particles. It is characteristic behaviour in other systems that display an antiferromagnetic spin-flop[5; 75–78]. For the hexagonal plates, the strong response with cooling in $\chi_{FC}(T)$ below T_N is representative of ferro-/ferrimagnetic behaviour at the surface of the particles.

Magnetization as a function of applied magnetic field $M(\mu_0 H)$ clearly show the shape dependent magnetism of the surfaces. M vs $\mu_0 H$ quarter loops at 10 K for the cubes and plates are shown in Fig. 3.12. All of the nanoshapes display a very clear paramagnetic component to the magnetization which arises from the cores of each of the shapes. An additional paramagnetic component is present for both the cubes and spheres above an applied field of 1 T arising from the surface spin-flop[5; 75–78]. The core's magnetic behaviour is identified by the high-field M vs $\mu_0 H$ behaviour, which can be represented as a susceptibility $\chi = M/\mu_0 H$ known as the high-field susceptibility $\chi_{HF}(T)$. M vs $\mu_0 H$ loops are fit with a linear function at fields > 3 T

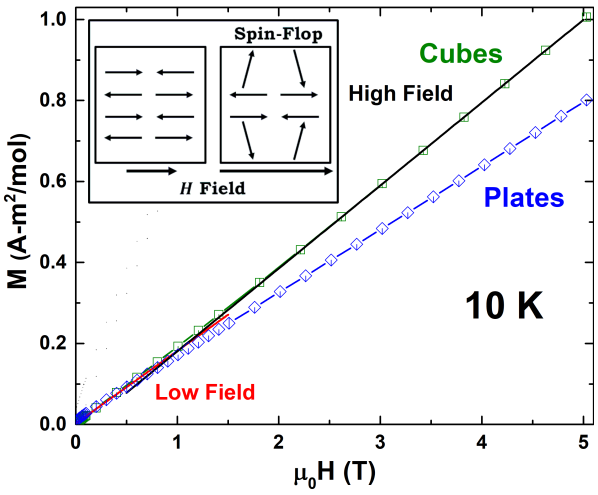

Figure 3.12: Unsubtracted M vs $\mu_0 H$ (quarter) loops for the cubes and plates at 10 K. Spheres display similar behaviour to that of the cubes (not shown). Extrapolation of the low and high field susceptibility are shown with red and black lines, respectively. The inset shows a cube shaped particle that undergoes a spin-flop at the surface.

to obtain χ_{HF} for a given temperature.

The temperature dependence of the high-field susceptibility is shown for all shapes in Fig. 3.13. $\chi_{HF}(T)$ is nearly identical for all three shapes above 30 K, an indication of similar core behaviour between the shapes. Additionally, we find that the plates display an ordering temperature $T_N = 30\ K$, closer to the bulk value for Co_3O_4. Performing the same inverse susceptibility analysis that was done on $\chi_{DC}(T)$ for the high-field susceptibility, we find that the values for χ_0, θ and μ_{eff} all have values very close to bulk (Table 3.4). This leads to similar exchange constants J_{ij} for the cores of each of the shapes, further evidence that the core orders differently than the surface. Since the high-field, and low-field susceptibilities show such different behaviour, this lends credence to our previous interpretation that χ_{DC} is indeed, representative of the magnetism at the surface.

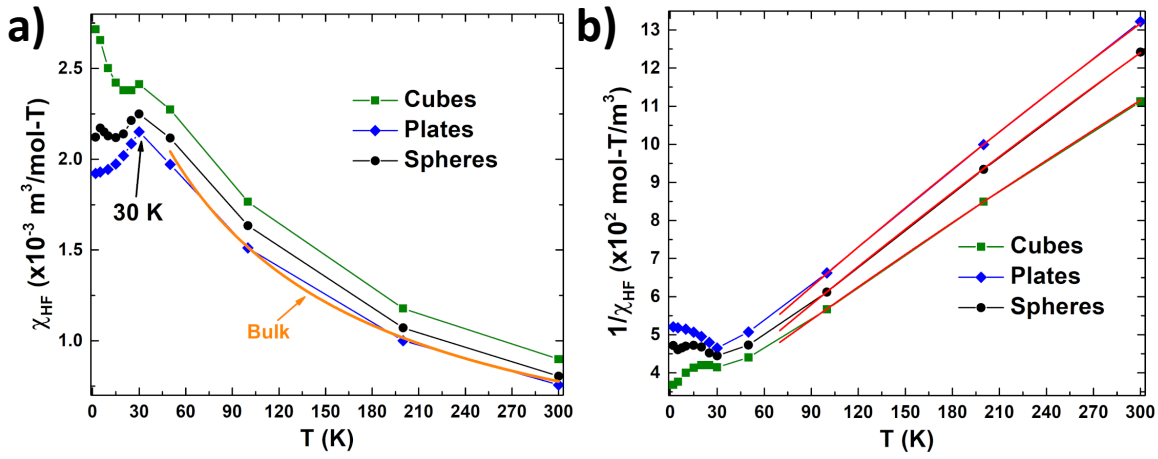

Figure 3.13: χ_{HF} vs T is shown for all three shapes. The high-field susceptibility arises from the core of the nanoshapes; above 30 K all shapes display similar behaviour to bulk (orange) and the plates show an ordering temperature of 30 K, different than the value obtained from DC susceptibility ($T_N = 25\ K$).

Table 3.4: χ_{HF} Magnetic Properties

Shape	χ_0 (m^3/mol-T^{-1})[3]	C (m^3-K/mol-T^{-1})	θ (K)	μ_{eff} (μ_B)
Spheres	0.9×10^{-4}	0.27(1)	-73(5)	4.1(2)
Plates	0.9×10^{-4}	0.25(1)	-77(5)	4.0(2)
Cubes	0.9×10^{-4}	0.31(5)	-86(5)	4.4(2)

To further quantify the magnetism we can subtract the high field susceptibility ($\chi_{HF}\mu_0 H$) from the measured M vs $\mu_0 H$ data. Because the high-field susceptibility is representative of the core the overall magnetization can be represented by:

$$M = M_{surf} + M_{core} = M_{surf} + \chi_{HF}\mu_0 H \tag{3.3}$$

where M_{surf} and M_{core} are the surface and core contributions to the magnetization,

[3] χ_0 is fixed to the bulk value for fits of the high-field susceptibility.

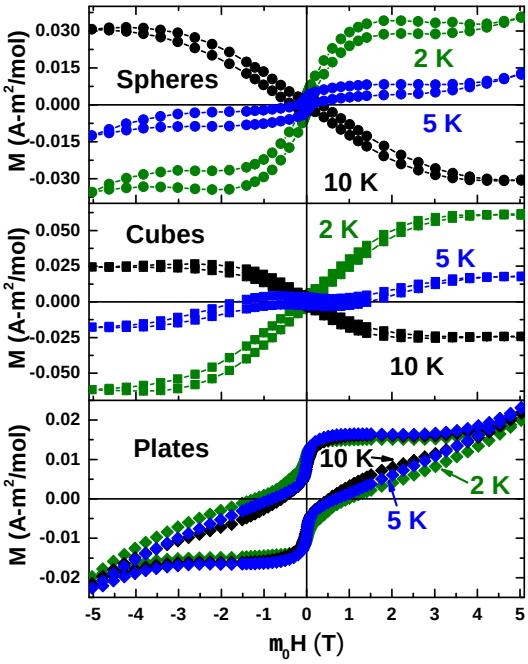

Figure 3.14: Subtracted M vs $\mu_0 H$ loops for the different shapes at 2, 5, and 10 K. The cubes and spheres show characteristic behaviour for an antiferromagnetic spin-flop, while the plates show ferromagnetic behaviour.

respectively. For the different shapes the surface M vs $\mu_0 H$ behaviour at 2, 5, and 10 K are shown in Fig. 3.14. The spheres and cubes both display "inverted" hysteresis loops for temperatures between 10-25 K. This is the clearest indication that a surface spin-flop has occurred and antiferromagnetic interactions are still dominant at the surface[5; 75–78]. The extra linear component that occurs at high magnetic fields (> 1 T) causes an overcompensation in the subtraction for the surface magnetization ($M - \chi_{HF}\mu_0 H$), leading to the inverted loops.

The spin-flop of the surface layer occurs at a much lower field required for bulk Co_3O_4 due to the competition between ferromagnetic and antiferromagnetic exchange[20]. The transition from negative magnetic saturation to positive saturation (as the tem-

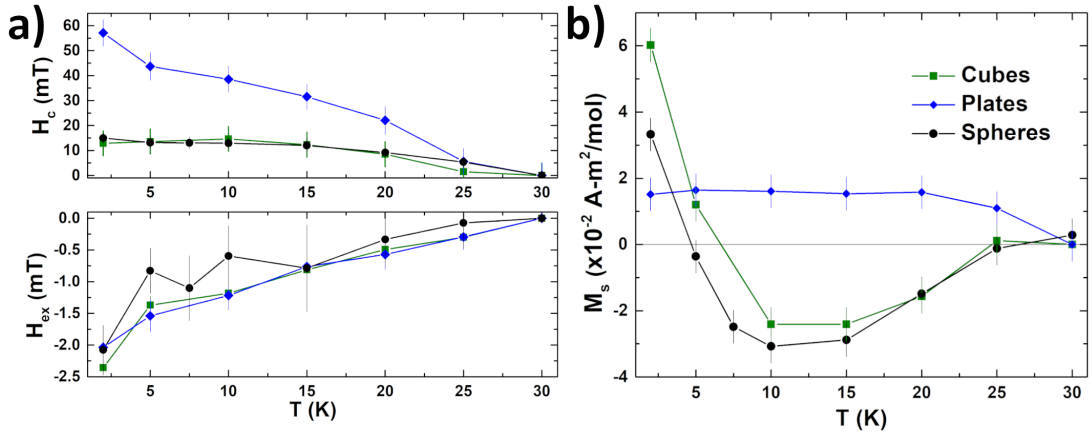

Figure 3.15: a) Coercivity $H_c(T)$ and exchange bias $H_{ex}(T)$ as a function of temperature for each of the shapes. Due to the ferromagnetic interactions at the surface, the plates show a much larger coercivity. b) The magnetic saturation $M_s(T)$ as a function of temperature for all shapes. Shows the very different caused by the different surface terminations.

perature is decreased) occurs due to the temperature dependence of the spin-flop field, and saturation of the spin-flop layer. As the temperature decreases thermal activation energy decreases leading to stronger competition at the surface layer, lowering the field at which the spin-flop can occur. By 2 K the spin-flop occurs at such a small field that the magnetization of the surface spin-flop layer saturates.

Due to the core-shell nature of the spheres and cubes coupling between the surface spin-flop layer and the antiferromagnetic core can occur, resulting in a coercivity (H_c, in an overall antiferromagnet) and exchange bias (H_{ex}). H_c and H_{ex} are shown in Fig. 3.15 for the M vs $\mu_0 H$ loops taken below 30 K. The spheres and cubes show roughly equal behaviour in the coercivity, exchange bias and saturation.

The surface magnetization in Fig. 3.14 that occurs for the plates is very different than the other shapes. Magnetic saturation remains positive and constant through-

out the region below T_N, and the plates also have a larger (4-5x larger) monotonically increasing coercivity below the ordering temperature. This indicates the strong ferromagnetic interactions (relative to the other shapes) and magnetic anisotropy that are occurring at the surface of the plates. Thus, ferromagnetic interactions are dominant at the (111) surface of the plates.

Chapter 4

Cu-Doped Co_3O_4 ($Cu_xCo_{3-x}O_4$)

4.1 Introduction

In CuO copper is in the Cu^{2+} oxidation state and in Cu_2O it has the Cu^{1+} oxidation state. Cu has the electronic structure $4s^1 3d^{10}$ and thus Cu^{1+} has the electronic structure $3d^{10}$ (removing the outer $4s$ electron) containing no unpaired electrons in the d orbitals and resulting in diamagnetism. For Cu^{2+} one electron is removed from the d orbitals and we obtain the structure $3d^9$ which contains a single unpaired electron undergoing superexchange interactions in oxide compounds such as CuO, instigating antiferromagnetic order. Cu^{3+} is much more elusive[79]. Originally, it was thought that the superconducting cuprates, or hole-doped cuprates may contain Cu^{3+}. But, as a substitute for the holes occupying Cu^{2+} ($Cu^{2+} + e^+ \rightarrow Cu^{3+}$ where e^+ indicates an electron hole) creating a mixed valence structure of Cu^{2+}/Cu^{3+}, Cu prefers to remain Cu^{2+} forming a $3d^9$ ligand hole on the oxygen ions ($Cu^{3+} \rightarrow Cu^{2+} + 3d^9\underline{L}$, where $\underline{L}$ signifies a ligand hole)[80–83].

Cu-doped Co_3O_4 ($Cu_xCo_{3-x}O_4$) is a spinel with both Cu and Co ions occupying

Table 4.1: Cu-doped Co_3O_4 XRD Refinements

Nominal Doping	Size (nm)	Lattice Constant (Å)	Total Cu	Cu_{Oh}:Cu_{Td} Occupancies	CuO %	Chemical Formula from XRD
$x = 0$	26(1)	8.084(1)	0	0% : 0%	0%	$(Co)[Co_2]O_4$
$x = 0.1$	22(1)	8.084(1)	0.08	66% : 34%	0%	$(Cu_{0.03}Co_{0.97})[Cu_{0.05}Co_{1.95}]O_4$
$x = 0.2$	21(1)	8.087(1)	0.20	59% : 41%	0%	$(Cu_{0.08}Co_{0.92})[Cu_{0.12}Co_{1.88}]O_4$
$x = 0.25$	18(1)	8.088(1)	0.30	62% : 38%	0%	$(Cu_{0.11}Co_{0.89})[Cu_{0.19}Co_{1.81}]O_4$
$x = 0.3$	20(1)	8.087(1)	0.31	48% : 52%	0%	$(Cu_{0.16}Co_{0.84})[Cu_{0.15}Co_{1.85}]O_4$
$x = 0.4$	17(1)	8.088(1)	0.50	44% : 56%	1%	$(Cu_{0.23}Co_{0.77})[Cu_{0.22}Co_{1.78}]O_4$
$x = 0.5$	16(1)	8.090(1)	0.48	56% : 44%	3%	$(Cu_{0.21}Co_{0.79})[Cu_{0.27}Co_{1.73}]O_4$

octahedral and tetrahedral sites. Analogous to the hole-doped cuprates, instead of Cu^{3+} occupying the O_h sites, Cu^{2+} resides at the octahedral interstices with a $3d^9\underline{L}$. Both $Cu^{2+}(T_d)$ and $Cu^{2+}(O_h)$ can both undergo Jahn-Teller distortions (requiring a degenerate crystal field ground state).

Due to the nature of $Cu^{2+}(O_h)$ creating a ligand hole, exchange interactions and the magnetism can be drastically affected. Re-examining the exchange in the core of the $Cu_xCo_{3-x}O_4$ presents the possibility of new ferro- and antiferromagnetic interactions. This allows us to investigate the ferromagnetic exchange between $Co^{2+}(T_d)$ and $Cu^{2+}(O_h)$ that results in the ferrimagnetic behaviour in the core of the particles.

4.2 Crystal Structure and Ligand Holes in $Cu_xCo_{3-x}O_4$

XRD for the Cu-doped samples are presented in Fig. 4.1. Rietveld refinements were performed using FullProf[84]. Along with pattern fits, residuals for the undoped ($x = 0$) sample are shown in Fig. 4.1. The rest of the samples display residuals

nearly identical to the one shown. Most of the patterns are phase pure (by relative volume) with the exception of $x = 0.4$ and 0.5 that present an additional CuO phase of 1% and 3%, respectively. The primary phase consists of the expected spinel-type structure with space group $Fd\bar{3}m$. From the refinements, there is an increase in the lattice constant (8.084 - 8.090 Å) and decrease in the crystallite size (26 - 16 nm) as the doping (x) for Cu increases (shown in Fig. 4.2 a)). The secondary phase phase found in dopings $x \geq 0.4$, is tenorite (CuO) with space group $C2/c$[85].

Both lattice constant and crystallite size show a roughly linear increase with doping. The decrease in crystallite size is consistent with increased strain in the nanoparticles as Cu enters the structure. As discussed in section 1.3.2, both Cu^{2+} tetrahedral (T_d) and octahedral (O_h) can undergo localized Jahn-Teller distortions. The increase

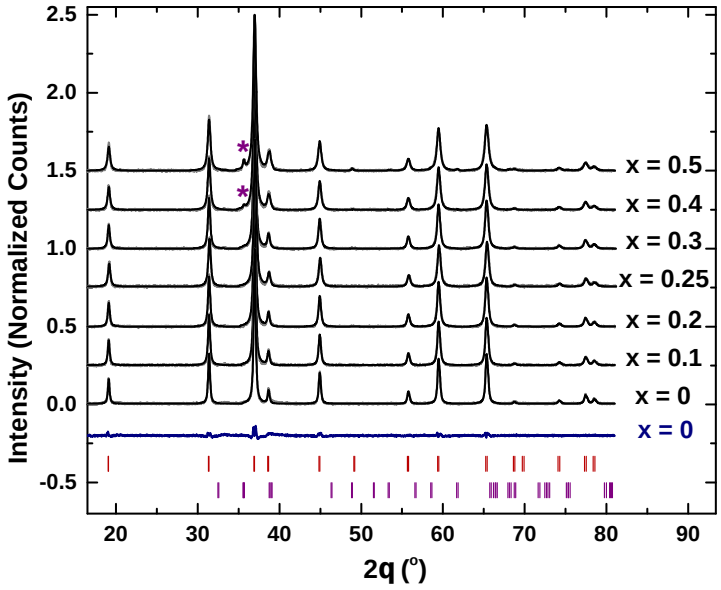

Figure 4.1: XRD patterns for all the Cu doped Co_3O_4 samples. Pattern fits (solid black lines) are shown along with residuals for the $x = 0$ sample (blue line), and peak markers for the primary (red ticks) and secondary CuO phase (*, and purple ticks) obtained from Rietveld refinement.

in lattice constant is a result of Cu^{2+} occupying the O_h site. $Cu^{2+}(O_h)$ has an ionic radii (0.73 Å) much larger than $Co^{3+}(O_h)$ (0.55 Å).

Using XRD, we are able to characterize changes in the occupancy of the cationic sites due to differences in the x-ray scattering cross-section for Co and Cu ions. The occupancies obtained from XRD refinement are roughly as expected from previous reports of $Cu_xCo_{3-x}O_4$ (Fig. 4.2 b)[86]. It is found that Cu occupies both tetrahedral and octahedral sites with a T_d:O_h ratio of roughly 50%:50%. The results from the fits are given in table 4.1.

TEM images were obtained to confirm the overall size and size distributions for the particles. Fig. 4.3 a) and b) shows typical images for the samples, obtained for the $x = 0$ and $x = 0.5$ samples, respectively. Size distributions for all imaged samples shown in Fig. 4.4 were fit with a lognormal function, showing large variation in the

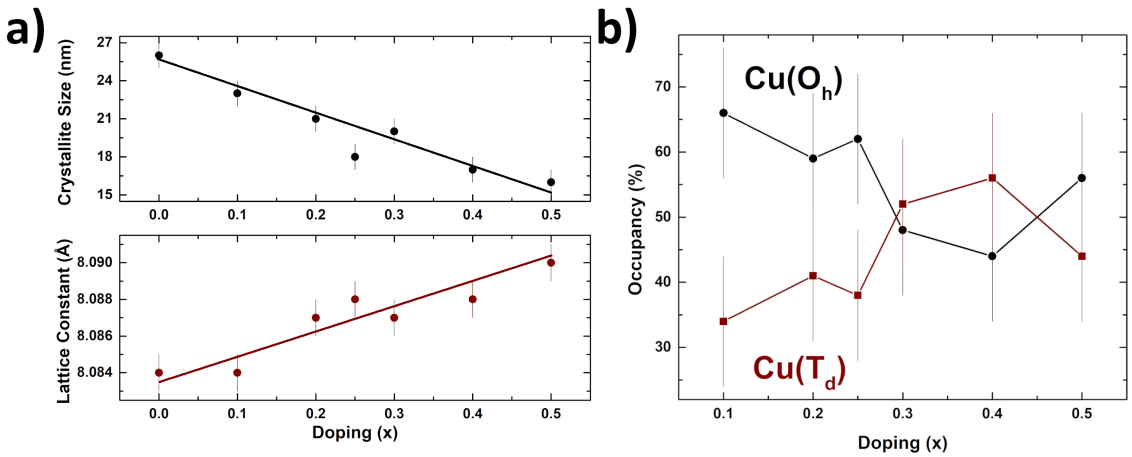

Figure 4.2: a) Crystallite size and lattice constant as a function of doping, obtained from XRD refinements. A linear decrease in the crystallite size and increase in the lattice constant occurs as Cu enters the structure. b) Cu occupancies obtained from XRD refinements show large uncertainty, with values of a occupancy ratio at roughly 50%:50% (O_h:T_d).

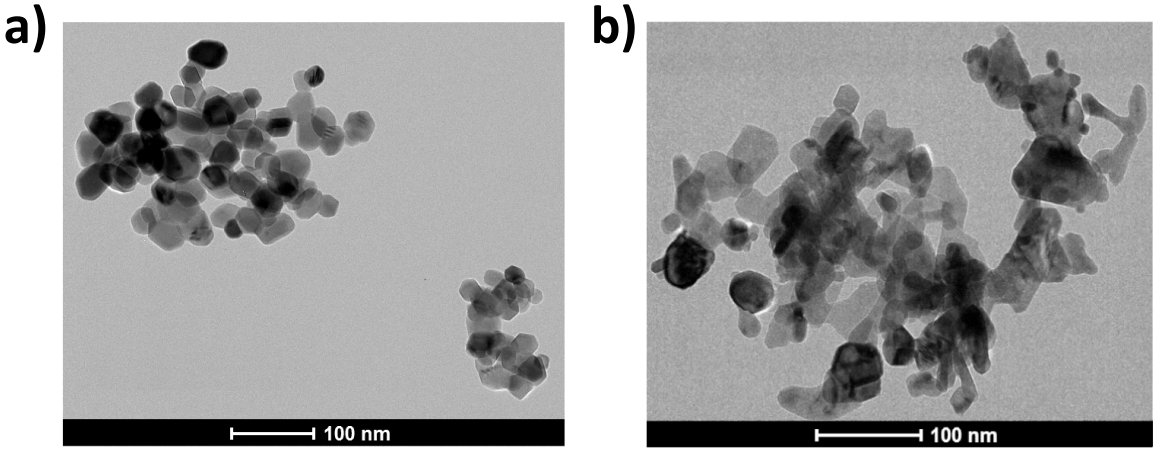

Figure 4.3: TEM images of a) the undoped ($x = 0$) sample, and b) the $x = 0.5$ sample.

Table 4.2: TEM Size Analysis

Nominal Doping	Particle Diameter (nm)
$x = 0$	31(4)
$x = 0.1$	34(8)
$x = 0.2$	22(4)
$x = 0.3$	23(4)
$x = 0.4$	19(5)
$x = 0.5$	19(6)

uncertainty for the size of the particles (table 4.2). TEM was obtained for all samples excluding the $x = 0.25$ doping. Samples are mostly single crystallites, with the sizes roughly matching the crystallite size obtained from XRD. Larger particles, most likely formed from multiple crystallites, are more abundant for the Cu doped samples. This results in large and occasionally bimodal distributions.

XAS measurements were performed over the Co (7.5 - 8.5 keV) and Cu (8.8 - 9.8 keV) K-edges. The near-edge portion of the spectrum, XANES, allows us to obtain information concerning the composition, relative oxidation states of the metal

ions, and $3d$-$4p$ hybridization. Fig. 4.5 a) shows the Co K edge XANES spectra for all of the samples collected at 300 K. We find that all the samples show similar spectra; small changes in the edge energy indicate a slight change in the Co^{2+}:Co^{3+} ratios between the dopings. The Co edge has a well-defined pre-edge structure, with roughly two-thirds of the contribution arising from the $1s$ to $3d$ transition for the $Co^{3+}(O_h)$ sites[59; 87]. The Cu K edge XANES spectra are shown in Fig. 4.5 b) for all the samples. With virtually no change in the edge energy we find that the Cu has a similar overall oxidation state for all of the samples. The pre-edge feature for the Cu K edge is much less defined since the $3d^9$ structure of Cu^{2+} only allows for one transition to a $3d$ orbital per Cu^{2+} (O_h or T_d).

The extended x-ray absorption fine structure (EXAFS) portion of the XAS spectrum identifies the local changes to the structure around the absorbing atom. Allowing

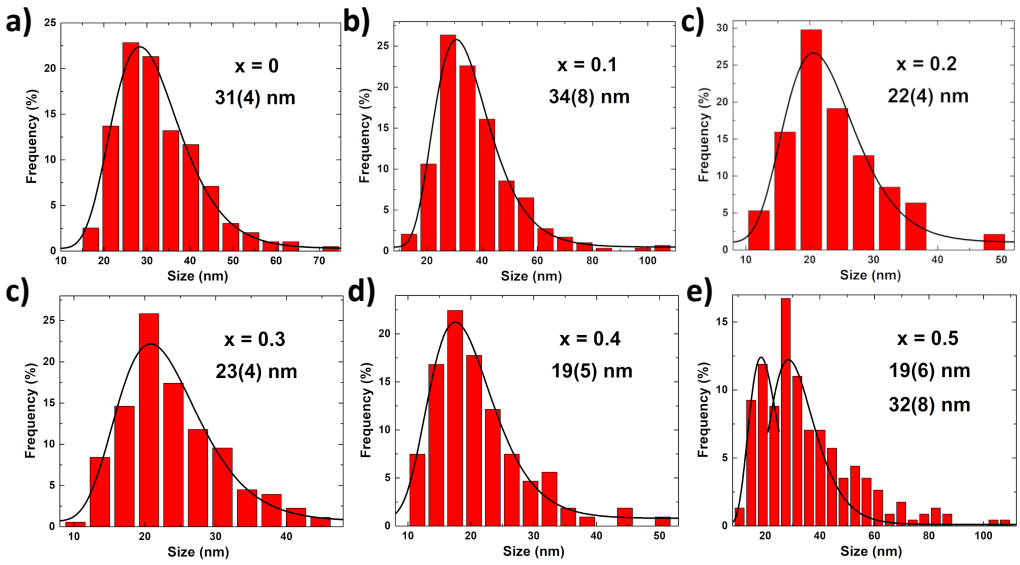

Figure 4.4: a) - e) Size distributions for the $x = 0$-0.5 samples, excluding $x = 0.25$.

Table 4.3: Cu-doped Co_3O_4 EXAFS Cu Results

Nominal Doping	Total Cu (±0.05)	Cu(O_h) : Cu(T_d) Occupancies (±10%)	CuO %	Chemical Formula from XRD (±0.05)
$x = 0$	0	0% : 0%	0%	$(Co)[Co_2]O_4$
$x = 0.1$	0.1	70% : 30%	0%	$(Cu_{0.03}Co_{0.97})[Cu_{0.07}Co_{1.93}]O_4$
$x = 0.2$	0.2	24% : 76%	0%	$(Cu_{0.15}Co_{0.85})[Cu_{0.05}Co_{1.95}]O_4$
$x = 0.25$	0.3	55% : 45%	0%	$(Cu_{0.13}Co_{0.87})[Cu_{0.17}Co_{1.83}]O_4$
$x = 0.3$	0.3	45% : 55%	0%	$(Cu_{0.17}Co_{0.83})[Cu_{0.13}Co_{1.87}]O_4$
$x = 0.4$	0.4	36% : 64%	0%	$(Cu_{0.26}Co_{0.74})[Cu_{0.14}Co_{1.86}]O_4$
$x = 0.5$	0.4	60% : 40%	10(5)%	$(Cu_{0.16}Co_{0.84})[Cu_{0.24}Co_{1.76}]O_4$

us to quantify the coordination, interionic distances, bond disorder and specifically the occupation of the different absorbers (such as O_h and T_d). Spectra were taken over the Co and Cu K edges at 300 K to obtain information on how Cu is incorporated into the structure, along with changes to the environments of the Co ions. The fitted

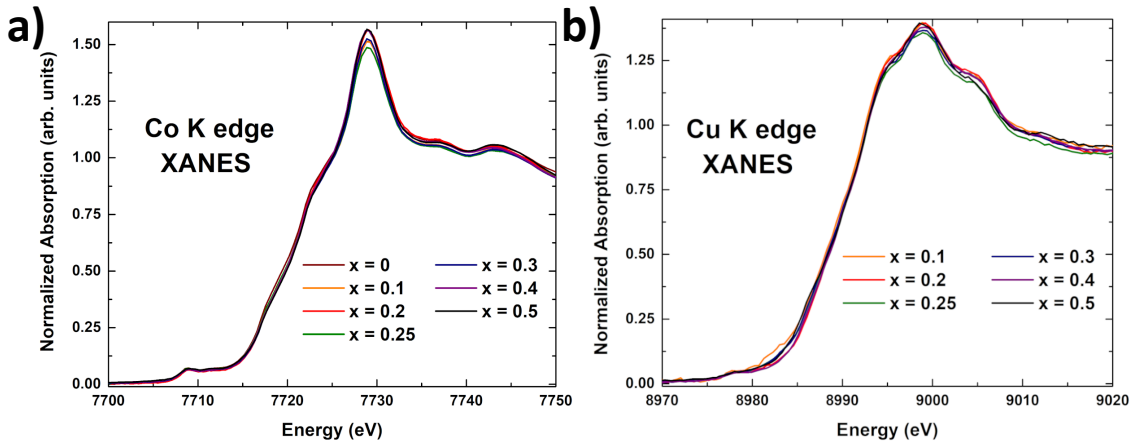

Figure 4.5: XANES spectra for the a) Co K edge and b) Cu K edge, obtained at 300 K. The small pre-edge region (7710 eV and 8980 eV for Co and Cu, respectively) shows hybridization between the metal 3*d* and 4*p* states.

spectra are shown in Fig. 4.6 a) and b) with the tabulated results of the fit in table 4.3. Fits for each of the samples were performed using the Artemis: EXAFS Data Analysis software[60].

Fits for the Co K edge show the characteristic peaks of a spinel structure[88; 89]. That of the first oxygen coordination shell at 1.5 Å (for both Co(O_h) and Co(T_d) as absorbers), one that arises from scattering between Co(O_h) (absorber) and other O_h sites (Co(O_h) - (O_h); 2.4 Å), and one from scattering between Co(T_d) absorbers and other T_d sites (Co(T_d) - (T_d); 3.0 Å). The peaks at 2.4 and 3.0 Å contain small contributions from other second-order scattering paths such as, paths that reach past first coordination shells or scattering events that involve multiple different ions for example, the Co$(O_h)_0$ - O - Co$(O_h)_1$ - Co$(O_h)_0$ scattering paths (the subscript 0 denotes absorber and subscript 1 represents the first coordination shell). These paths

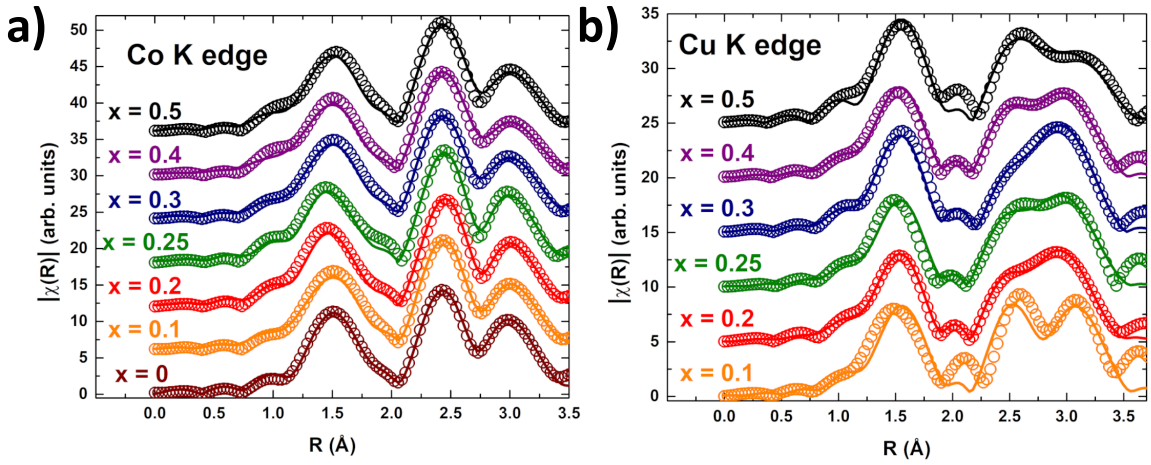

Figure 4.6: EXAFS spectra for the a) Co K edge and b) Cu K edge, obtained at 300 K. For the Co K edge spectrum, peaks at 2.4 Å and 3.0 Å are primarily due to the scattering paths of Co(O_h) - (O_h) and Co(T_d) - (T_d). Likewise for Cu K edge, the peaks at 2.6 Å and 3.2 Å denote the paths Cu(O_h) - (O_h) and Cu(T_d) - (T_d).

only account for a very small percentage of the overall intensity observed, and thus, the peaks provide a good estimate for the occupancies of the O_h and T_d absorbers. With the peak at 3.0 Å decreasing as a function of doping this characterizes larger decrease in the Co(T_d) occupancy.

To characterize undoped Co_3O_4 we use two sets of scattering paths, one for Co(T_d) as an absorber and one with Co(O_h) as the absorber. Each set of paths contain three single scattering paths, Absorber - O, Absorber - O_h site, and Absorber - T_d site (with either Co(O_h) or Co(T_d) as the absorber). When fitting undoped Co_3O_4 (only the Co K edge) in Artemis the occupancy portion of the amplitude parameter S_0^2 will be 0.333 for all of the Co(T_d) absorber scattering paths and 0.666 for all of the Co(O_h) absorber scattering paths. This is obtained from the overall occupancy of the different Co atoms (1:2, T_d:O_h). From XRD measurements, we know Cu is occupying both O_h and T_d sites in a ratio different from that of the 1:2 (T_d:O_h) for normal spinel

Table 4.4: Co(O_h) - O and Co(T_d) - O

$Cu_xCo_{3-x}O_4$	Absorber	N	E_0 (eV)	R (Å)	σ^2 (Å^2)
x=0	Co(O_h) Co(T_d)	6 4	-5.6(6)	1.93(1) 1.94(1)	0.001(1)
x=0.1	Co(O_h) Co(T_d)	6 4	-6.1(7)	1.92(1) 1.94(1)	0.004(1)
x=0.2	Co(O_h) Co(T_d)	6.0(3) 4.0(2)	-6.4(7)	1.92(1) 1.94(1)	0.004(1)
x=0.25	Co(O_h) Co(T_d)	6 4	-7.1(7)	1.92(1) 1.94(1)	0.004(1)
x=0.3	Co(O_h) Co(T_d)	6 4	-6.5(7)	1.92(1) 1.94(1)	0.004(1)
x=0.4	Co(O_h) Co(T_d)	6 4	-6.8(8)	1.92(1) 1.94(1)	0.004(1)
x=0.5	Co(O_h) Co(T_d)	6 4	-6.5(8)	1.92(1) 1.94(1)	0.003(1)

Table 4.5: Co(O_h) - (O_h) and Co(T_d) - (T_d)

$Cu_xCo_{3-x}O_4$	Absorber	N	E_0 (eV)	R (Å)	σ^2 (Å^2)
x=0	Co(O_h)	6	-5.6(6)	2.87(1)	0.004(1)
	Co(T_d)	4		3.51(1)	0.005(1)
x=0.1	Co(O_h)	6	-6.1(7)	2.86(1)	0.003(1)
	Co(T_d)	4		3.51(1)	0.005(1)
x=0.2	Co(O_h)	6.0(3)	-6.4(7)	2.86(1)	0.004(1)
	Co(T_d)	4.0(2)		3.51(1)	0.006(1)
x=0.25	Co(O_h)	6	-7.1(7)	2.86(1)	0.003(1)
	Co(T_d)	4		3.50(1)	0.006(1)
x=0.3	Co(O_h)	6	-6.5(7)	2.86(1)	0.004(1)
	Co(T_d)	4		3.51(1)	0.006(1)
x=0.4	Co(O_h)	6	-6.8(8)	2.86(1)	0.004(1)
	Co(T_d)	4		3.50(1)	0.006(1)
x=0.5	Co(O_h)	6	-6.5(8)	2.86(1)	0.004(1)
	Co(T_d)	4		3.50(1)	0.006(1)

Table 4.6: Co(O_h) - (T_d) and Co(T_d) - (O_h)

$Cu_xCo_{3-x}O_4$	Absorber	N	E_0 (eV)	R (Å)	σ^2 (Å^2)
x=0	Co(O_h)	6	-5.6(6)	3.36(1)	0.005(1)
	Co(T_d)	12			
x=0.1	Co(O_h)	6	-6.1(7)	3.36(1)	0.005(1)
	Co(T_d)	12			
x=0.2	Co(O_h)	6.0(3)	-6.4(7)	3.36(1)	0.006(1)
	Co(T_d)	11.9(6)			
x=0.25	Co(O_h)	6	-7.1(7)	3.35(1)	0.006(1)
	Co(T_d)	12			
x=0.3	Co(O_h)	6	-6.5(7)	3.36(1)	0.006(1)
	Co(T_d)	12			
x=0.4	Co(O_h)	6	-6.8(8)	3.35(1)	0.006(1)
	Co(T_d)	12			
x=0.5	Co(O_h)	6	-6.5(8)	3.35(1)	0.006(1)
	Co(T_d)	12			

structures. In other words, due to the fact that we have varying copper occupancies (i.e. we can have 70% tetrahedral Cu and 30% octahedral Cu), our fitted EXAFS spectra must reflect this.

For pure Co_3O_4 if we consider a Co tetrahedral absorber that emits a photo-electron that scatters off another tetrahedral site there is a 100% chance that the photo-electron scatters off cobalt. But if we consider $x = 0.2$ in the Cu-doped structure ($Cu_{0.2}Co_{2.8}O_4$) that has 70% of the Cu in T_d sites and 30% of Cu in O_h sites. This means that:

$$\text{Cu } (T_d/O_h) \text{ Occupancy} \times \text{Total Cu} = \text{Total Cu in } (T_d/O_h) \text{ Site}$$

$$0.7 \times 0.2 = 0.14 \text{ Amount Cu in } T_d \text{ sites}$$

$$0.3 \times 0.2 = 0.06 \text{ Amount Cu in } O_h \text{ sites}$$

The real stoichiometry is written as: $(Cu_{0.14}Co_{0.86})[Cu_{0.06}Co_{1.94}]O_4$. Where (A) indicates a tetrahedral site and [B] indicates an octahedral site. Now consider the same Co(T_d) absorber with a photo-electron scattering off of a neighbouring tetrahedral site, we find that 14% of the scattering events will be a Cu ion and not Co ion (86% of scattering events are from Co). Now if we examine the Co(T_d) - Co(O_h) and Co(T_d) - Cu(O_h) for the same tetrahedral Co absorber, consider what percentage of the scatterers are Cu(O_h) instead of Co(O_h). We find that:

$$\frac{[\text{amount Cu}(O_h)]}{[\text{Total } (O_h) \text{ occupancy}]} = \frac{0.06}{2} = 0.03 \tag{4.1}$$

or 3% of the scatterings will be off Cu(O_h) and 97% off Co(O_h).

Thus, scattering paths for a given absorber like Co(T_d) now have different S_0^2 amplitudes. This requires a robust method of using the right occupancy factors for each of the paths for different absorbers. In a Cu-doped Co_3O_4 sample we have four absorbers for each edge to characterize the difference in Co and Cu neighbours.

Table 4.7: Cu(O_h) - O and Cu(T_d) - O

$Cu_xCo_{3-x}O_4$	Absorber	N	E_0 (eV)	R (Å)	σ^2 (Å^2)
x=0.1	Cu(O_h) Cu(T_d)	8(7) 5(4)	3(7)	1.96(4) 1.98(4)	0.004(1)
x=0.2	Cu(O_h) Cu(T_d)	6 4	0(1)	1.94(1) 1.95(1)	0.004(1)
x=0.25	Cu(O_h) Cu(T_d)	6(1) 4(1)	1(2)	1.95(1) 1.94(1)	0.004(1)
x=0.3	Co(O_h) Cu(T_d)	8(2) 5(1)	1(5)	1.96(4) 1.95(4)	0.004(1)
x=0.4	Cu(O_h) Cu(T_d)	7(1) 5(1)	0(1)	1.95(1) 1.95(1)	0.004(1)
x=0.5	Cu(O_h) Cu(T_d)	8(2) 5(1)	2(5)	1.96(6) 1.96(6)	0.003(1)

To obtain structures with Cu and Co neighbours, crystallographic information files (CIF) files from XRD refinements are modified to obtain the appropriate neighbouring atoms.

To obtain a proper parameterization of the paths we must examine the occupancies for the different sites. To start, we fix the total Cu (this can be varied manually), the total Co is then obtained along with Cu and Co occupancies. From the occupancies we can obtain individual scale factors for the scattering paths that reflect the fraction of Co and Cu neighbours. The Cu(T_d) occupancy is then varied while all other parameters compensate accordingly.

To obtain the individual scale factors we look at an example of a scattering event between a Cu(O_h) absorber and a Cu(O_h) scatterer. The occupancy of the absorber (e.g. $Cu_{Oh}Occ$ denotes the occupation of the Cu(O_h) sites) multiplied by the proportional fraction of the given neighbouring site $\left(\frac{[amount\ Cu(O_h)]}{[total\ (O_h)\ occupancy]} = \frac{totCu_{Oh}}{2}\right)$ gives us

Table 4.8: Cu(O_h) - (O_h) and Cu(T_d) - (T_d)

$Cu_xCo_{3-x}O_4$	Absorber	N	E_0 (eV)	R (Å)	σ^2 (Å^2)
x=0.1	Cu(O_h)	8(7)	3(7)	2.92(6)	0.007(10)
	Cu(T_d)	5(4)		3.58(8)	0.006(10)
x=0.2	Cu(O_h)	6	0(1)	2.89(1)	0.006(5)
	Cu(T_d)	4		3.52(1)	0.010(1)
x=0.25	Cu(O_h)	6(1)	1(2)	2.91(2)	0.011(2)
	Cu(T_d)	4(1)		3.51(3)	0.009(1)
x=0.3	Co(O_h)	8(2)	1(5)	2.92(5)	0.007(7)
	Cu(T_d)	5(1)		3.52(6)	0.006(4)
x=0.4	Cu(O_h)	7(1)	0(1)	2.90(2)	0.005(2)
	Cu(T_d)	5(1)		3.52(2)	0.008(1)
x=0.5	Cu(O_h)	8(2)	2(5)	2.93(8)	0.008(6)
	Cu(T_d)	5(1)		3.54(9)	0.008(5)

the fraction (Cu_{Oh}-Cu_{Oh}) of the scattering events:

$$\text{[Fraction of Scattering]} = \text{[Absorber Occupancy]} \times \text{[Fraction of scatterer]}$$

$$Cu_{Oh}\text{-}Cu_{Oh} = Cu_{Oh}Occ \times totCu_{Oh}/2$$

Where Cu_{Oh}-Cu_{Oh} is the scale factor for the Cu(O_h) absorber with Cu(O_h) neighbours and $totCu_{Oh}$ is the total Cu in the O_h sites. All of the associated scale factors for the individual scattering paths are obtained in this way.

Information about the fitting model and parameters:

- S_0^2: Controls the amplitude of the total spectra. Includes parametrization of Cu occupancies and coordination (N).

- E_0: Energy shift to line up the experimental data to the theoretical energy values. Co and Cu absorbers typically have different values for E_0.

- δR: Is a change in the distance for the individual path under consideration. For a cubic crystal this can be parametrized by using a variable say α for all the

Table 4.9: Cu(O_h) - (T_d) and Cu(T_d) - (O_h)

$Cu_xCo_{3-x}O_4$	Absorber	N	E_0 (eV)	R (Å)	σ^2 (Å^2)
x=0.1	Cu(O_h) Cu(T_d)	8(7) 16(14)	3(7)	3.43(7)	0.006(10)
x=0.2	Cu(O_h) Cu(T_d)	6 12	0(1)	3.38(1)	0.010(1)
x=0.25	Cu(O_h) Cu(T_d)	6(1) 12(2)	1(2)	3.41(2)	0.009(1)
x=0.3	Co(O_h) Cu(T_d)	8(2) 15(4)	1(5)	3.43(6)	0.006(4)
x=0.4	Cu(O_h) Cu(T_d)	7(1) 15(3)	0(1)	3.40(2)	0.008(1)
x=0.5	Cu(O_h) Cu(T_d)	8(2) 15(4)	2(5)	3.44(9)	0.008(5)

paths, multiplied by R_{eff}, the original distance of the given scattering path.

$$\delta R = \alpha \times R_{eff}$$

This allows us to characterize a change in the path distance based on how long the path is (longer paths undergo larger changes). The crystal is cubic so isotropic expansion or contraction is how changes in the path lengths are dealt with. This parameter should be equivalent for the different Co and Cu atoms in the same structure but are allowed to vary independently to help characterize finite size effects and strain within the particles. The scattering paths that contain Cu(O_h) as an absorber or scatterer receive their own independent fit parameter (α_{CuOh}) for δR. This is to account for the distortion to the structure caused specifically by the ligand hole mentioned in regard to the Cu(O_h) site. The true scattering path distance is then given by: $R = R_{eff} + \delta R$.

- σ^2: Is a positive parameter that controls the disorder of the bond, in other

words, how strongly those two atoms (absorber and scatterer) are bound to one another. σ^2 is typically of the order of $\sigma^2 \leq 0.01$. Because we are fitting over 24 paths over two separate edges it is required to find relations between the σ^2 for the different paths. All scattering paths to O ions have the same σ^2. O_h absorber to O_h neighbour, and T_d absorber to T_d neighbour have the same σ^2 values (different for Cu – Cu and Co – Co). And, all O_h absorber to T_d neighbour and T_d absorber to O_h neighbour all have the same σ^2 (different for Cu – Cu and Co – Co).

Table 4.4 shows the fit parameters (coordination N, energy shift E_0, scattering path distance R, and bond disorder σ^2) obtained from the Co K edge fit for the scattering path to the first oxygen coordination shell for both Co O_h and T_d sites, e.g. Co(O_h) - O and Co(T_d) - O. The tables 4.5 and 4.6 represent the scattering paths to the first shell of octahedral and tetrahedral sites. Table 4.5 shows the fit parameters for the respective site-to-site Co(O_h) - (O_h) and Co(T_d) - (T_d) scattering paths, while table 4.6 shows the parameters for the opposite site-to-site Co(O_h) - (T_d) and Co(T_d) - (O_h) scattering paths. Because of the distinction made by α_{CuOh} (the parameter used to incorporate distortion into the O_h site) there are two separate σ^2 values for the Co(O_h) - (O_h) and Co(T_d) - (T_d) paths in table 4.5.

Tables 4.7 - 4.9 show the same fit parameters but for the Cu K edge, which contains Cu sites as absorbers. The coordination for the $x = 0.2$ doping was varied for the Co K edge fit, but held constant for the Cu K edge fit. This was done to obtain an accurate value of the S_0^2 amplitude for the Co K edge that we can fix for the rest of the samples. This allows us to obtain proper parameterization of the S_0^2 amplitude

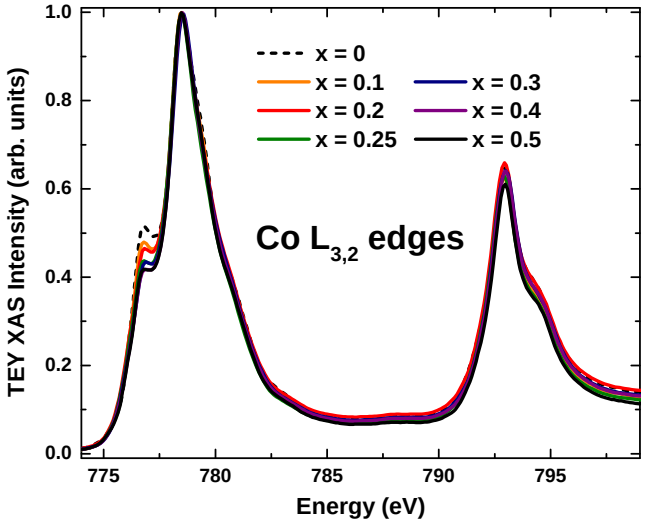

Figure 4.7: Co $L_{3,2}$ edge XAS obtained at 10 K for all the samples. The peak at 777 eV located at the start of the L_3 edge, shows a decrease as Cu enters the structure.

for the Cu K edge and allowing us to extract the coordination and occupation for the remainder of the samples.

The Cu K edge EXAFS clearly identify the presence of both Cu(O_h) and Cu(T_d) as absorbers due to the peaks located at 2.6 Åand 3.2 Å, respectively (Fig. 4.6). For both Co and Cu edges we find the coordination is as expected for a spinel structure. The scattering path length decreases (as doping increases) for the Co edge, and increases for the Cu edge. The Jahn-Teller distortion that Cu experiences causes a change in the oxygen positions along the z (c) axis, changing the oxygen position between the Co - O - Cu configuration. Intuitively the disorder parameter follows the same tendency as scattering path length; doping increases local disorder (from the Debye-Waller term of the fits shown in section 2.4.2) around the Co ions (σ^2_{Co}) increases, while σ^2_{Cu} decreases (or stays the same). This is all further evidence for a distortion caused by the Cu ions.

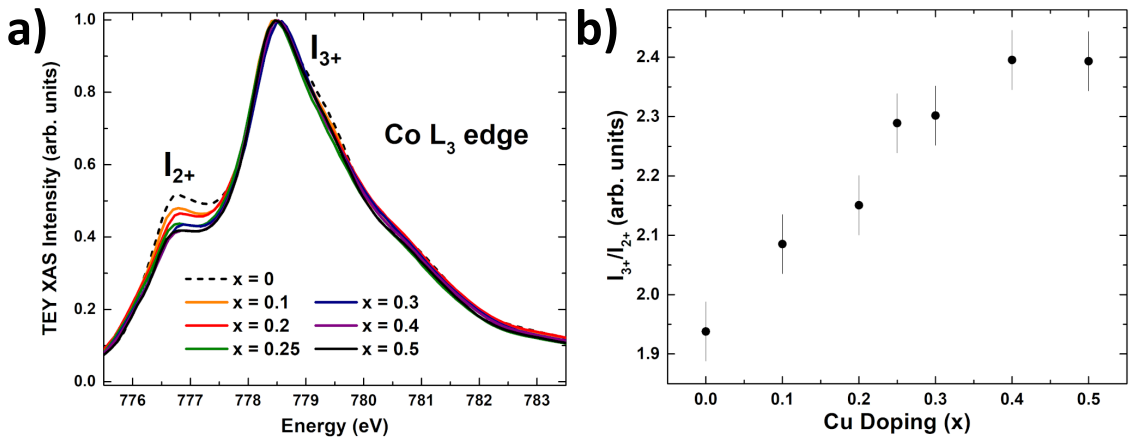

Figure 4.8: a) Shows a close-up for the Co L_3 edge XAS, with I_{2+} and I_{3+} indicating the main contributions from $Co^{2+}(T_d)$ and $Co^{3+}(O_h)$ ions. b) shows I_{3+}/I_{2+} as a function of doping.

From EXAFS we have been able to confirm the presence of both $Cu(O_h)$ and $Cu(T_d)$ within the spinel structure, where the total Cu conforms to what was obtained from XRD. We were also able to identify the presence of the secondary CuO phase of roughly 10% for the $x = 0.5$ sample.

L edge XAS allows us to obtain more specific information on the oxidation state and environment of the cations and surrounding oxygen atoms. Fig. 4.7 shows the XAS spectra for the Co $L_{3,2}$ edges at 10 K for all the samples. The Co L edge spectra are typical of Co_3O_4 spinel-type material[68]. The decrease in the shoulder peak at 777 eV indicates a decrease in the relative occupations of the Co^{2+} and Co^{3+} ions. The peak at 777 eV is dominated by $Co^{2+}(T_d)$ but small contributions from $Co^{3+}(O_h)$ are also present. Fig. 4.8 a) shows a close-up of the Co L_3 edge, where I_{2+} and I_{3+} indicate the intensities of the peaks corresponding to Co^{2+} and Co^{3+}, respectively. Fig. 4.8 b) shows the ratio of I_3/I_2 with an increase as a function of doping indicating

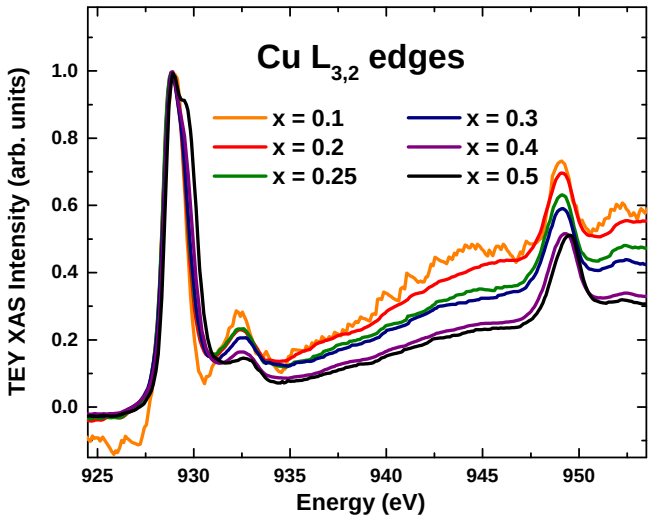

Figure 4.9: Cu $L_{3,2}$ XAS obtained at 10 K for all samples. Cu L edge spectra are all very similar. The absorption at 932.5 eV is a result of ligand holes on the O ions.

the variation in occupation of the Co sites, i.e. Co^{2+}:Co^{3+} ratio.

The Cu $L_{3,2}$ edge obtained at 10 K for the Cu doped samples (Fig. 4.9) are indicative of Cu^{2+} ions[90–93]. The small shoulder peak at 932.5 eV is due to the existence of a ligand hole (transition: $2p3d^9\underline{L} \rightarrow 2p^53d^9$) on the oxygen ions[94; 95]. The ligand hole is a direct result of Cu^{2+} occupying the octahedral sites: $Cu^{3+}(O_h) \rightarrow Cu^{2+}(O_h) + 3d^9\underline{L}$ as Cu prefers a 2+ oxidation state over a 3+ oxidation state[80–83]. The $3d^9\underline{L}$ mediates charge balance in the structure allowing Cu^{2+} to exist in both T_d and O_h sites without Co^{3+} entering the T_d sites. This is clear from the Co L edge spectra where there are no large changes from the undoped sample (other than the peak at 777 eV) which would indicate a change to a partially inverse spinel structure.

It is known that the separation between the $Cu^{2+}(T_d)$ and $Cu^{2+}(O_h)$ absorptions is only 0.7 eV[96]. Thus, to further examine the Cu spectra, a peak deconvolution is performed on the main absorption of the Cu L_3 edge. This allows us to obtain a more

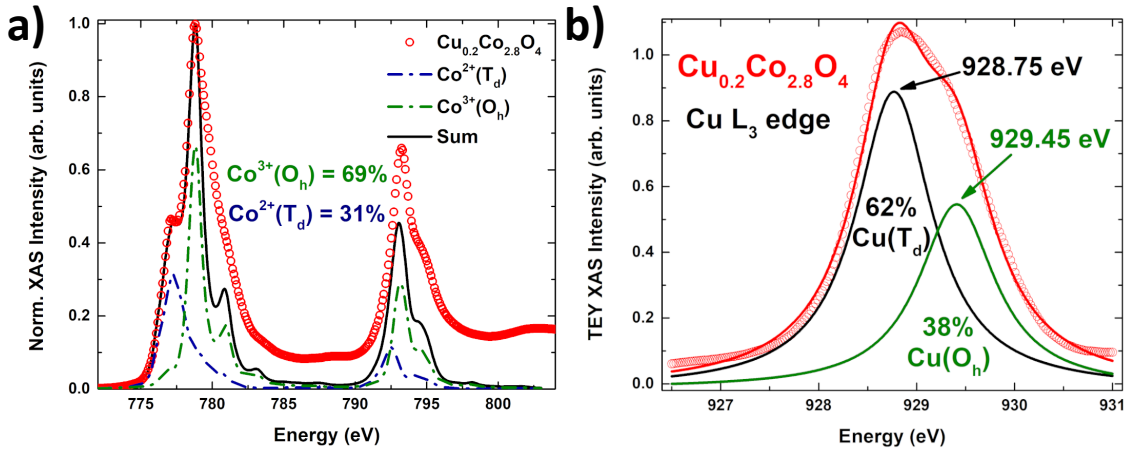

Figure 4.10: a) Fit of the Co $L_{3,2}$ edge spectrum for the $x = 0.2$ sample using CTM4XAS[3]. The spectrum shows that $Co^{2+}(T_d)$ dominates the peak at 777 eV, but contains small contributions from $Co^{3+}(O_h)$. b) Fit of the Cu L_3 edge for the $x = 0.2$ sample. From a peak deconvolution, it is found that 62% of the Cu occupies the T_d sites, and 38% occupies the O_h sites.

accurate estimate of the $Cu^{2+}(T_d)$ and $Cu^{2+}(O_h)$ occupations. Fig. 4.10 b) shows the deconvolution performed on the $x = 0.2$ sample. We find that the T_d occupation is larger than the O_h occupation of ~65%:35% (T_d:O_h). Peak deconvolutions performed

Table 4.10: Cu-doped Co_3O_4 L edge XAS Results

Nominal Doping	Co L edge fit(±3%): $Co^{3+}(O_h) : Co^{2+}(T_d)$	Cu L edge fit(±3%): $Cu^{2+}(O_h) : Cu^{2+}(T_d)$	Total Cu	Chemical Formula from XAS (±0.03)
$x = 0$	66% : 34%	0% : 0%	0	$(Co)[Co_2]O_4$
$x = 0.1$	68% : 32%	58% : 42%	0.37(10)	$(Cu_{0.15}Co_{0.85})[Cu_{0.21}Co_{1.79}]O_4$
$x = 0.2$	69% : 31%	38% : 62%	0.18(5)	$(Cu_{0.11}Co_{0.89})[Cu_{0.07}Co_{1.93}]O_4$
$x = 0.25$	70% : 30%	39% : 61%	0.36(5)	$(Cu_{0.22}Co_{0.78})[Cu_{0.14}Co_{1.86}]O_4$
$x = 0.3$	71% : 29%	38% : 62%	0.36(5)	$(Cu_{0.22}Co_{0.78})[Cu_{0.14}Co_{1.86}]O_4$
$x = 0.4$	72% : 28%	39% : 61%	0.46(5)	$(Cu_{0.28}Co_{0.72})[Cu_{0.18}Co_{1.82}]O_4$
$x = 0.5$	71% : 29%	42% : 58%	0.49(5)	$(Cu_{0.28}Co_{0.72})[Cu_{0.21}Co_{1.79}]O_4$

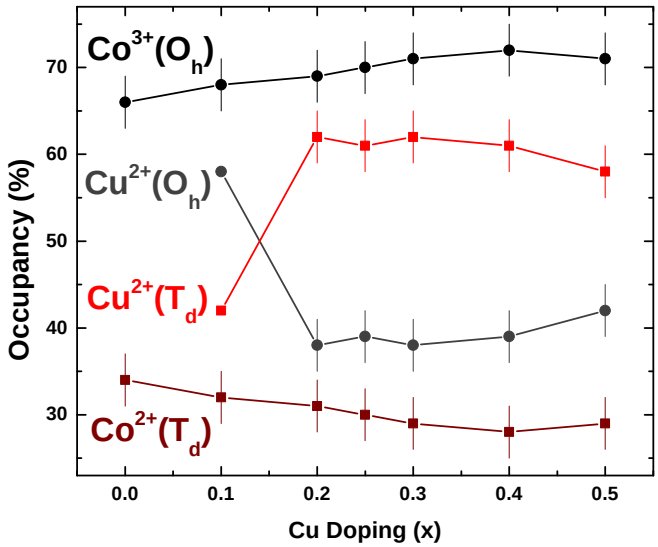

Figure 4.11: Occupancy of the four cationic sites ($Co^{2+}(T_d)$, $Co^{3+}(O_h)$, $Cu^{2+}(T_d)$, and $Cu^{2+}(O_h)$), obtained from analysis of the XAS fits. Cu^{2+} T_d:O_h ratio remains roughly the same at 60%:40%.

on all of the Cu L-edge spectra show similar shape and occupancy. As the doping increases ($x > 0.4$) the emergence of the third absorption becomes resolvable within the main L_3 absorption for the Cu edge. This peak is attributed to the formation of the CuO phase[92]. For $x = 0.5$ an impurity of roughly 7% was found. We were also able to perform fits for the Co L-edge spectra. Co L-edge fits were obtained by simulating both $Co^{2+}(T_d)$ and $Co^{3+}(O_h)$ contributions using CTM4XAS[3]. The fit for $x = 0.2$ is shown in Fig. 4.10, where the $Co^{3+}(O_h)$ and $Co^{2+}(T_d)$ occupations are 69% and 31% respectively.

The resultant occupancies obtained from the Co and Cu L edge XAS fits are shown in Fig. 4.11. We find that the $Cu^{2+}(T_d)$:$Cu^{2+}(O_h)$ remains the same at roughly 60%:40%. This is corroborated by the height of the $3d^9\underline{L}$ (Fig. 4.9) contribution. If the backgrounds are taken into account the height of the high-energy shoulder peak

Table 4.11: CTM4XAS Fit Parameters for $Co^{2+}(T_d)$ and $Co^{3+}(O_h)$

Parameter	$Co^{2+}(T_d)$	$Co^{3+}(O_h)$
Spin state; Symmetry	High spin; $^4A_2$	Low spin; $^1A_1$
SIR; S-O Reduction[1]	1.0; 1.0	1.0; 1.0
Crystal Field Splitting (10Dq)	-0.34	1.9
Δ[2]	7	4.5
$U_{pd} - U_{pp}$[3]	1.5	1.5
$T(e_g)/T(e)$[4]	0.9	2
$T(t_{2g})/T(t_2)$[4]	2	1

[1] Slater integral reduction (SIR) and spin-orbit (S-O) reduction are set to the default values.
[2] Charge transfer energy (Δ).
[3] Potential of the $2p$ core-hole and $3d$ valence electron (U_{pd}) and the potential of the $3d$-$3d$ valence electrons (U_{dd}). Only the difference of $U_{pd} - U_{dd}$ is relevant for XAS.
[4] Transfer integrals, $T(e_g)/T(e)$ and $T(t_{2g})/T(t_2)$, for the e_g/e and t_{2g}/t_2 orbitals, respectively.

is nearly identical throughout the series. Since we obtain the same ratio of ligand core holes that arise from $Cu^{2+}(O_h)$, we obtain the same ratio of $Cu^{2+}(T_d)$:$Cu^{2+}(O_h)$. Cu occupancies and total Cu are in agreement with those obtained from XRD and EXAFS analysis. The tabulated results obtained from the L edge XAS fits are given in table 4.10 along with fit parameters in table 4.11[68].

O K-edge XAS allows us to probe the differences in hybridization between the O $2p$ and metal $3d$ and $4s$ states directly. Oxygen K edge spectra shown in Fig. 4.12 were taken at 10 K for all samples. The peak at 531.5 eV allow us to quantify the $3d$ e_g and t_{2g} orbital occupations for the O_h ions in the structure[58]. With Cu replacing Co in the O_h site, the change from electronic structure ($3d^6 \rightarrow 3d^9$) results in a higher $3d$ occupation, i.e. less vacancies, and we see that the intensity of the peak at 531.5 eV decreases, thus confirming the presence of Cu in the O_h site. There is a decrease in the absorption above 537 eV. This is due to the decrease in hybridization between O $2p$ to metal $4s$ hybridization due to Cu occupying the structure. While $Cu^{2+}(O_h)$ still undergoes hybridization with the oxygen ligands (e.g. the ligand hole), $Cu^{2+}(T_d)$

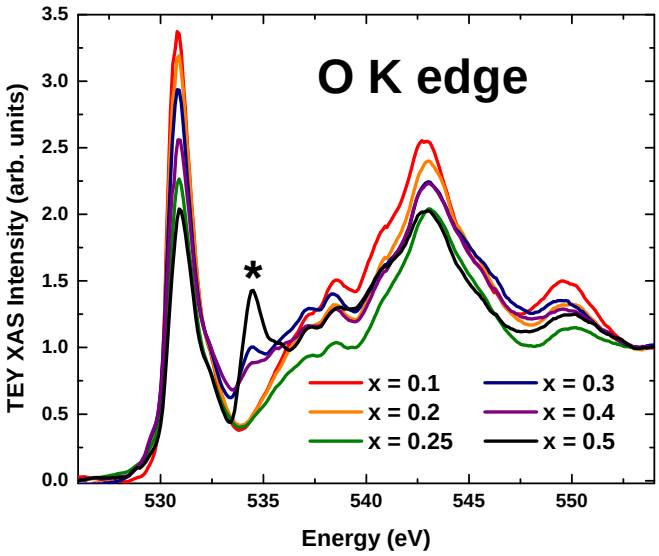

Figure 4.12: XAS obtained over the O K edge at 10 K for all samples. Changes in the $3d$ occupation between the samples is indicated by the decrease in the peak at 532 eV. The asterisk marks the position from vicinal oxygen[2].

undergoes minimal hybridization.

From XAS we have been able to identify the oxidation states and obtained accurate estimates of the O_h and T_d occupancies of the cations. All samples show very similar spectra with a $Cu^{2+}(T_d)$ occupancy larger than the $Cu^{2+}(O_h)$ occupancy. XAS and EXAFS can both be used to verify that the Cu enters the entire structure and not simply a surface substitution. EXAFS was performed in both transmission and fluorescence geometry, where the transmission set-up is a great probe for the core of the particles. Cu K-edge spectra are presented using fluorescence yield, but showed the same features using transmission detection. A much steeper background subtraction must be used for transmission detection while backgrounds for fluorescence yield are much more consistent between the samples. Likewise, L-edge XAS was performed using both total electron yield (TEY) and total fluorescence yield (TFY) detection

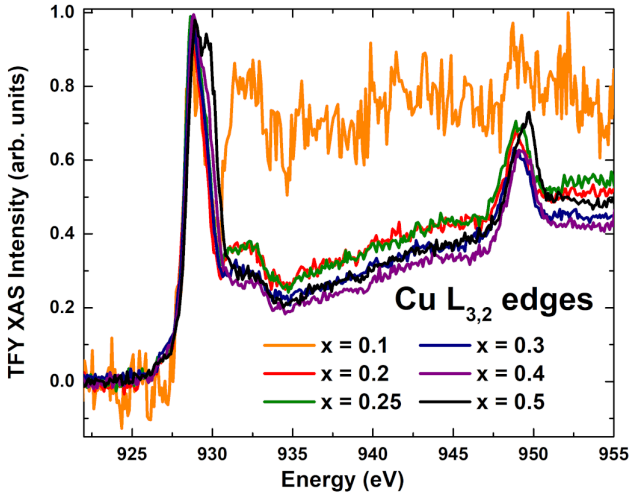

Figure 4.13: TFY XAS spectrum of the Cu $L_{3,2}$ edge for all samples. Since TFY measurements are bulk-sensitive, this is good evidence for Cu doping the entire structure.

techniques. Where TEY is known to probe only the first few nm, TFY measurements are bulk-sensitive[69]. As electrons are promoted to higher energy levels, electrons flow from the sample holder onto the surface of the sample. This is electron yield detection. When electrons repopulate lower energy levels, they fluoresce characteristic x-rays which are then detected via fluorescence detectors. Fluorescence arises primarily from the core but suffers more extensive broadening due to the self-absorption (e.g. the detected x-rays go through multiple scattering events before they are detected). These techniques provide a method to confirm the presence of Cu within the core of the particle. Fig. 4.13 shows the TFY XAS for each of the samples where the additional broadening from self-absorption is evident.

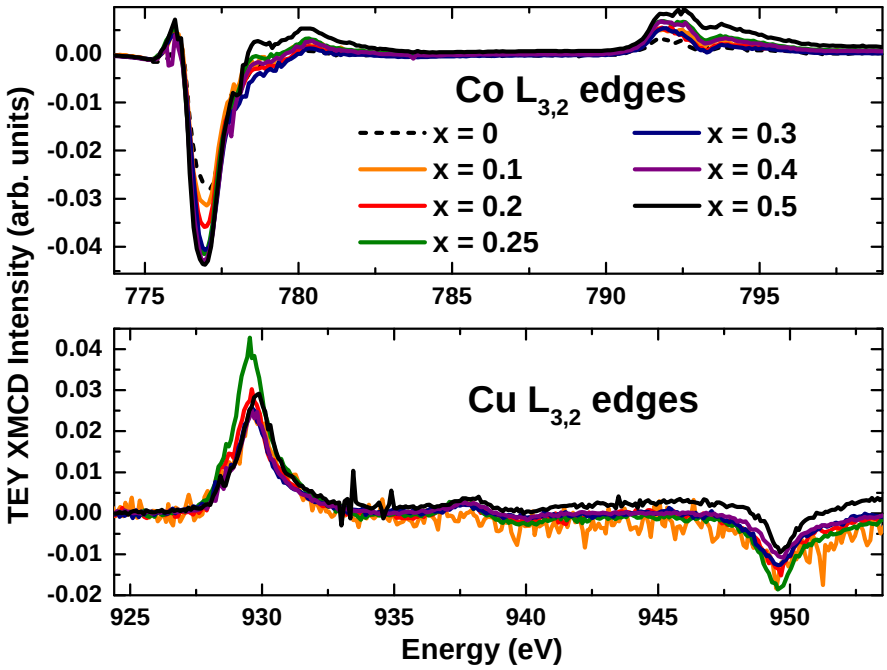

Figure 4.14: Co and Cu L edge XMCD obtained at 10 K for all of the samples. The Co L edge shows an increase in the magnetic moment due to the weakening of antiferromagnetic interactions. The Cu L edge XMCD shows an unchanging magnetic moment present only for the $Cu^{2+}(O_h)$ sites.

4.3 Ferrimagnetism of Cu-Doped Co_3O_4

XMCD probes the atomic level, local magnetic structure and provides the most straight-forward evidence of ferromagnetic interactions occurring in the Cu doped samples. Artefact-free (AF) XMCD spectra shown in Fig. 4.14 were obtained at 10 K under applied fields of ±5 T, as described in section 2.4.1. For the Co L edge XMCD we find an increase in the Co magnetic moment corresponding to the increase in the L_3 edge peak at 777 eV that arises from the $Co^{2+}(T_d)$.

Using CTM4XAS we can simulate the XMCD spectrum for the Co $L_{3,2}$ edge, the simulation of the $x = 0.2$ sample is shown in Fig. 4.15. The only contribution to

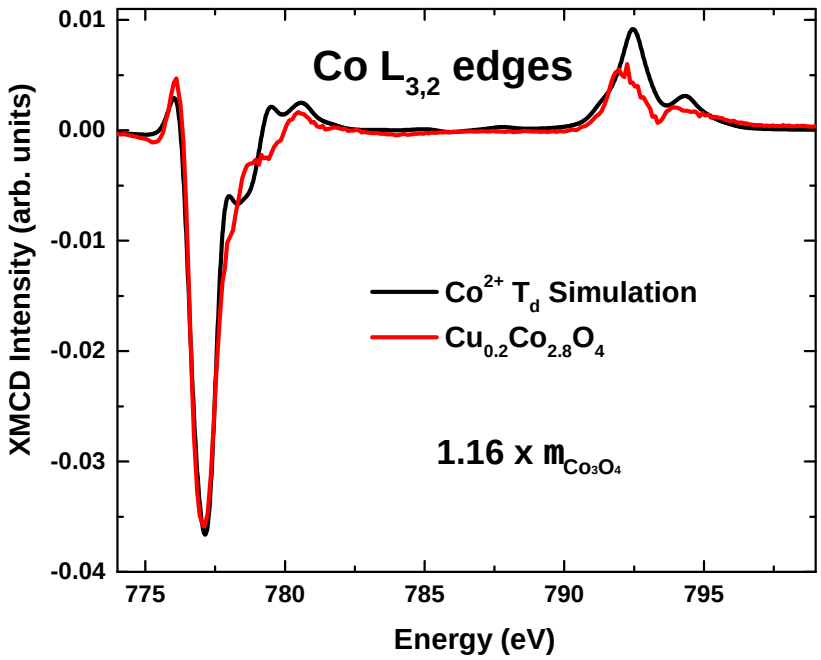

Figure 4.15: Co L edge XMCD fit using CTM4XAS of the $x = 0.2$ sample obtained at 10 K. $Co^{3+}(O_h)$ ions carry no unpaired spins, and thus, the only contribution to the magnetic moment arises from $Co^{2+}(T_d)$. For $x = 0.2$ the magnetic moment is $\sim$1.2 times larger than that of Co_3O_4.

the spectrum is from the $Co^{2+}(T_d)$ ions, and all fits agree well with what has been obtained experimentally. Due to the decrease in antiferromagnetic interactions in Cu-doped samples the magnetic moment of the $Co^{2+}(T_d)$ is $\sim$1.2 times larger than the magnetic moment of Co_3O_4 (for $x = 0.2$).

Expectedly in the Cu $L_{3,2}$ edge XMCD, we find a magnetic moment present on the Cu ions. With the position of the Cu L_3 edge peak in the XMCD at 929.5 eV and referring back to Fig. 4.9, we find it represents a ferro/ferrimagnetic contribution from the $Cu^{2+}(O_h)$ ions. This contribution arises due to the new exchange interactions present in the Cu doped Co_3O_4. As discussed previously, the reason for the stronger antiferromagnetic order in pure (bulk) Co_3O_4 is a result of the large number

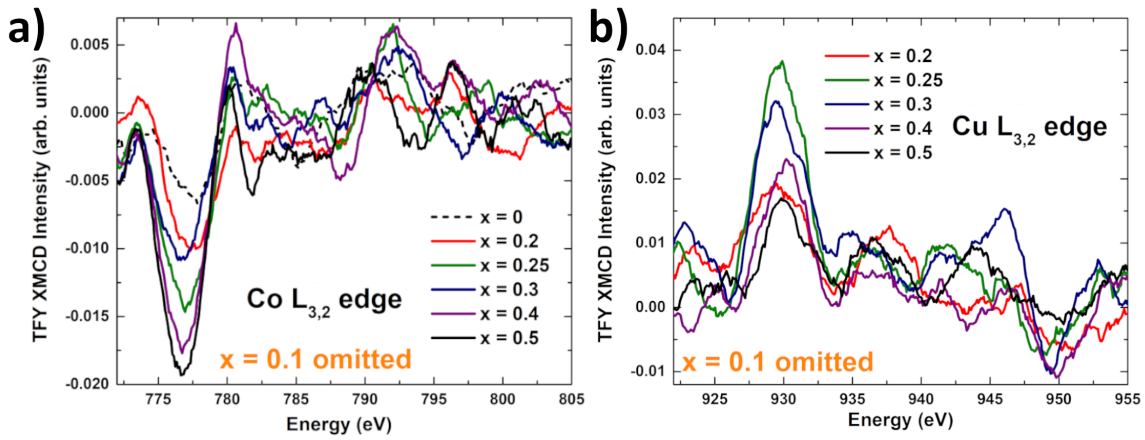

Figure 4.16: a) Co and b) Cu L edge XMCD obtained at 10 K for all of the samples using TFY detection. The Co L edge shows a decrease in the magnetic moment relative to TEY, while the Cu edge shows almost no change between the magnetic moment from TEY and TFY.

of extended superexchange interactions that are possible. These will be examined in detail (in section 5.3) in the context of $Cu_xCo_{3-x}O_4$. Briefly examining TFY XMCD we find further evidence of ferro/ferrimagnetic behaviour in the core of the particles. The magnitude of the TEY XMCD signals for the Co and Cu edge are roughly equal at 3-4% (Fig. 4.14). TFY XMCD for both the Co and Cu $L_{3,2}$ is shown in Fig. 4.16 a) and b), respectively. The TFY measurements shows a drastic decrease in the XMCD magnetic moment for the Co edge, but a similar sized moment for the Cu edge. Indicating the ferromagnetic interactions associated with the $Cu^{2+}(O_h)$ site within the core of the particles. The sample $x = 0.1$ was omitted due to the poor quality of the spectrum for both Co and Cu L edge XMCD using TFY detection, this can also be seen in the Cu L edge XAS and XMCD using TEY detection.

As mentioned previously, for antiferromagnetic materials such as Co_3O_4 the ordering temperature (T_N) can be obtained from the maximum in the DC susceptibility,

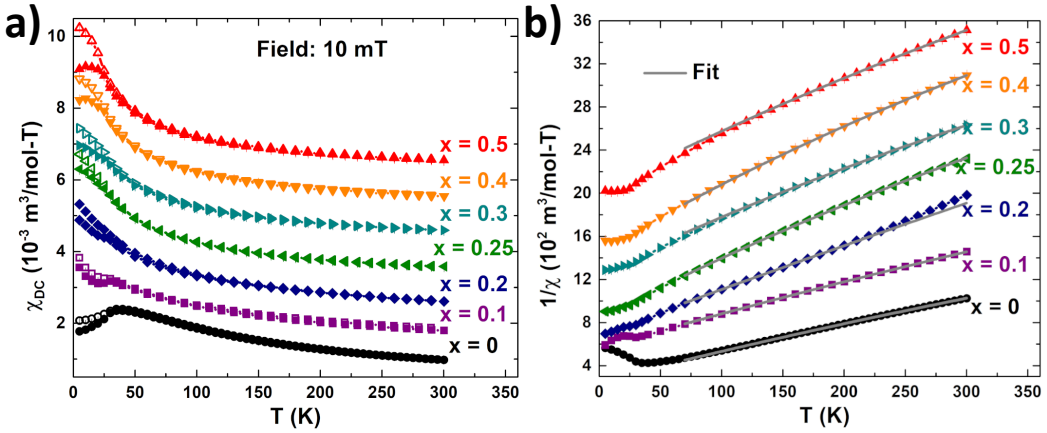

Figure 4.17: a) $\chi_{DC}(T)$ for all samples shows a decrease in the ordering temperature with increasing Cu doping. Below the ordering temperature we find evidence for a weak ferromagnetic behaviour as the doping increases. b) $1/\chi_{DC}$ is fit for each sample (solid grey lines) between 160 - 280 K, with the exception of $x = 0.2$.

$\chi_{DC}(T)$. Further, examination of the susceptibility above and below T_N can give us an idea of the exchange interactions present. The low-field (10 mT) DC susceptibility is shown in Fig. 4.17 a) for all samples. As the doping of Cu increases, we observe a decrease in the Néel temperature. Undoped Co_3O_4 ($x = 0$) has the largest ordering temperature of $T_N = 39(2)$ K, and decreases to $T_N = 23(2)$ K for the $x = 0.5$ sample (Fig. 4.18). This is a result of the complicated nature of exchange interactions in Co_3O_4 discussed previously. The non-interacting nature of the $Cu^{2+}(T_d)$ ions result in a decrease in the strength of the antiferromagnetic interactions. This is also shown qualitatively in $\chi_{DC}(T)$ by the more abrupt rise in susceptibility as temperature decreases for the Cu doped samples, e.g. $\chi_{DC}(T)$ for the undoped sample is flatter compared to samples doped with Cu.

To gain a more quantitative measure of the exchange interactions occurring we can once again represent the susceptibility above T_N using the modified Curie-Weiss

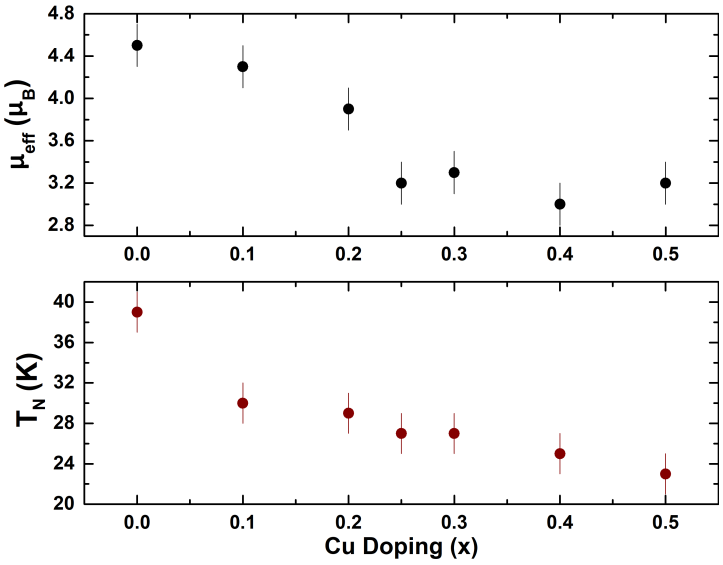

Figure 4.18: μ_{eff} and T_N as a function of doping obtained from the fits of $1/\chi_{DC}$. Both μ_{eff} and T_N show a decrease with increasing Cu doping.

law derived in section 1.1.2. Analysis was performed on the inverse susceptibility ($1/\chi_{DC}$), with the high-temperature fits for each of the samples shown in Fig. 4.17 b). In the absence of Jahn-Teller splitting, the crystal field ground states for the Cu $3d^9$ electronic structure in both octahedral and tetrahedral crystal fields are a doublet (^{2}E) and triplet (^{2}T) state, respectively[14]. In this situation Cu does not contribute to the van Vleck paramagnetic term.

By including Jahn-Teller distortions (tetragonal, $c > a$) the ground state for Cu in the O_h site becomes a singlet (^{2}A) with one unpaired spin in the upper $d_{x^2-y^2}$ orbital. Including the same type of distortion for the tetrahedral site we find that both d_{xz} and d_{yz} orbitals are farther away from the O ions than the d_{xy} orbitals (due to extension in the z direction) and thus lie lower in energy. This again creates a singlet state (^{2}A) with one unpaired electron in the upper d_{xy} orbital. For a contraction

Table 4.12: χ_{DC} Magnetic Properties

Nominal Doping	χ_0 ($\times 10^{-4}$ m^3/mol T^{-1})	C (m^3 K/mol T^{-1})	θ (K)	T_N (K)	μ_{eff} (μ_B)	J_{ij} (K/k_B)
$x = 0$	1.4(1)	0.32(1)	-85(5)	39(2)	4.5(2)	2.9(5)[5]
$x = 0.1$	1.0(1)	0.29(1)	-110(5)	30(2)	4.3(2)	2.4(5)
$x = 0.2$	0.3(1)	0.23(1)	-80(5)	29(2)	3.9(2)	2.9(5)
$x = 0.25$	1.1(1)	0.16(1)	-40(5)	27(2)	3.2(2)	4.0(5)
$x = 0.3$	1.2(1)	0.17(1)	-55(5)	26(2)	3.3(2)	3.6(5)
$x = 0.4$	1.1(1)	0.14(1)	-30(5)	26(2)	3.0(2)	4.3(5)
$x = 0.5$	0.9(1)	0.16(1)	-55(5)	21(2)	3.2(2)	3.1(5)

[5] Using the spin-only value ($J = S = 3/2$) to calculate the exchange constant J_{ij} gives a value of $J_{ij} = 3.9(2)$ K/k_B, nearly identical to the value of bulk Co_3O_4 $J_{ij} = 4.0(2)$ K/k_B quoted by Roth (reference 6 in the text).

in the z direction ($c < a$) we find that the $Cu^{2+}(T_d)$ contains a doublet ground state (^{2}E) and thus does not contribute to any van Vleck paramagnetism ($c < a$ produces the same singlet ground state for an O_h site). For a Cu ion that undergoes Jahn-Teller splitting the contributions to χ_0 are of the same order as the Co ions. Thus, we do not expect to find a large change in the values for χ_0 since all of the ions present in the spinel contribute to van Vleck paramagnetism (save perhaps the $Cu^{2+}(T_d)$ site which depends on the direction of the tetragonal distortion). Indeed, χ_0 remains relatively constant between 0.9-1.4$\times 10^{-4} m^3/mol - T$; the bulk value is $1.4\times 10^{-4} m^3/mol - T$[17].

The Curie constant C from the fits provides us with a quantitative measure of the effective magnetic moment μ_{eff} using equation 3.2. Fig. 4.18 shows the decrease in overall magnetic moment μ_{eff} as a function of doping. The decrease in magnetic moment is attributed to replacing $Co^{2+}(T_d)$ ($s = 3/2$) with $Cu^{2+}(T_d)$ ($s = 1/2$)

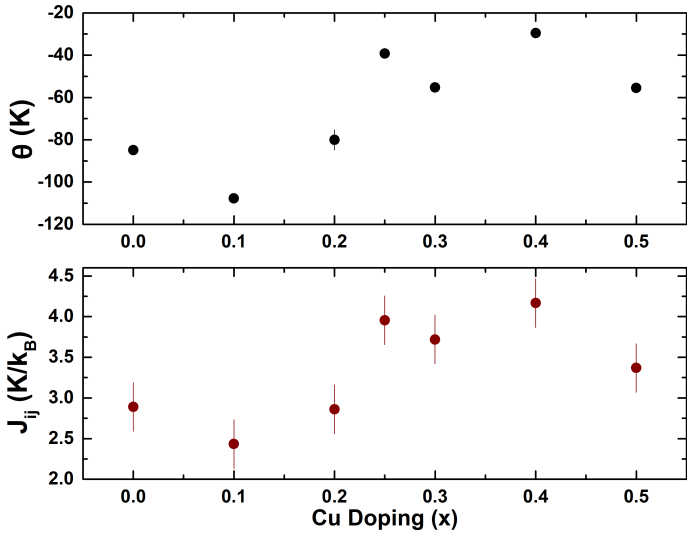

Figure 4.19: θ and J_{ij} as a function of doping obtained from magnetometry. Both θ and J_{ij} show very similar behaviour, increasing as doping increases. This is a result of the decrease in antiferromagnetic interactions.

causing a decrease in the overall spin moment per formula unit.

To gain further insight we can investigate both θ and J_{ij} as a function of doping. Where θ, the Weiss temperature, is largely a qualitative measure of the exchange occurring, with $\theta < 0$ indicating antiferromagnetic interactions and J_{ij} described by the ordering temperature T_N and the effective magnetic moment μ_{eff} (through equation 1.24). Both J_{ij} and θ are shown in Fig. 4.19 and display identical behaviour as a function of doping. The increase in J_{ij} and decrease in θ with doping is consistent with decreased antiferromagnetic interactions along with a smaller overall magnetic moment. The overall results from the analysis of $1/\chi_{DC}$ are given in table 4.12.

Examining the DC susceptibility below the magnetic ordering T_N we find evidence of weak ferro/ferrimagnetic behaviour as a result of Cu entering the structure. $Cu^{2+}(T_d)$ has a small ionic radius, and high electron occupation. This leads to de-

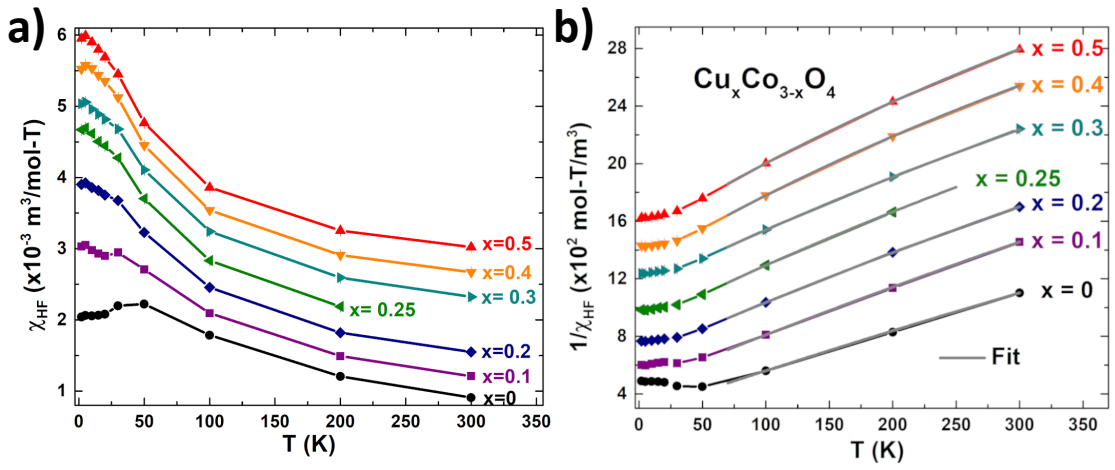

Figure 4.20: a) High-field susceptibility as a function of temperature ($\chi_{HF}(T)$), for each of the Cu dopings. Behaviour is similar to the field cooled DC susceptibility. b) Fits for the inverse high-field susceptibility ($1/\chi_{HF}$) show similar values for the fit parameters (χ_0, θ, and C) as in the DC susceptibility.

creased orbital overlap, and decreased multiplicity for exchange interactions. Thus, $Cu^{2+}(T_d)$ can be considered non-interacting relative to the $Cu^{2+}(O_h)$. Weak ferromagnetic interactions can occur between the $Co^{2+}(T_d)$ and the $Cu^{2+}(O_h)$ ions.

Magnetization as a function of field (M vs μ_0H) data was obtained for all samples for a range of temperatures between 2 and 300 K up to 5 T to ensure saturation. M vs μ_0H loops for the samples still display a paramagnetic/antiferromagnetic component to the magnetization, as in Co_3O_4. For Co_3O_4 we were able to obtain loops for the surface through the process described in section 3.3, by subtracting a high-field susceptibility (χ_{HF}) multiplied by the field ($\mu_0 H$) from the original magnetization data. As mentioned earlier, the high-field susceptibility as a function of temperature $\chi_{HF}(T)$ describes the magnetic interactions occurring in the core of the particles. $\chi_{HF}(T)$ is shown in Fig. 4.20 a), where each of the samples display similar behaviour to the field cooled low-field susceptibility. Performing the same Curie-Weiss analysis

Table 4.13: χ_{HF} Magnetic Properties

Nominal Doping	χ_0 ($\times 10^{-4}$ m^3/mol T^{-1})	C ($\times 10^{-3}$ m^3-K/mol T^{-1})	θ (K)	μ_{eff} (μ_B)
$x = 0$	0.9(1)	0.32(1)	-86(5)	4.5(2)
$x = 0.1$	0.8(1)	0.26(1)	-64(5)	4.1(2)
$x = 0.2$	1.0(1)	0.25(1)	-53(5)	4.0(2)
$x = 0.25$	1.3(1)	0.22(2)	-39(5)	3.7(2)
$x = 0.3$	1.3(1)	0.22(1)	-40(5)	3.7(2)
$x = 0.4$	1.6(1)	0.18(1)	-27(5)	3.4(2)
$x = 0.5$	1.6(1)	0.17(1)	-27(5)	3.3(2)

on the inverse high-field susceptibility ($1/\chi_{HF}$, Fig. 4.20 b), we find identical fit values (χ_0, θ, C) as was found in the low-field analysis. This leads to the same values for the effective magnetic moment, which provides further evidence for Cu doping the entire structure. Results from the analysis of $1/\chi_{HF}$ are given in table 4.13.

Subtracted M vs μ_0H loops (as described in section 3.3) are shown in Fig. 4.21 a) and b), samples are shown for 2 K and 15 K, respectively. Immediately we recognize the behaviour of the $x = 0$ sample where we can identify the results of weakened antiferromagnetic interactions at the surface through the characteristic behaviour of the spin-flop[5; 75–78]. The antiferromagnetic interactions at the surface of the undoped sample are stronger than previously characterized for the shapes resulting from the larger size of the particles (i.e. less surface-to-volume ratio). The rest of the samples display small ferro/ferrimagnetic interactions throughout the whole particle, showing a large increase in the magnetic saturation. Unlike the previous characterization of the shapes (and the $x = 0$ sample) which are ideal antiferromagnets in

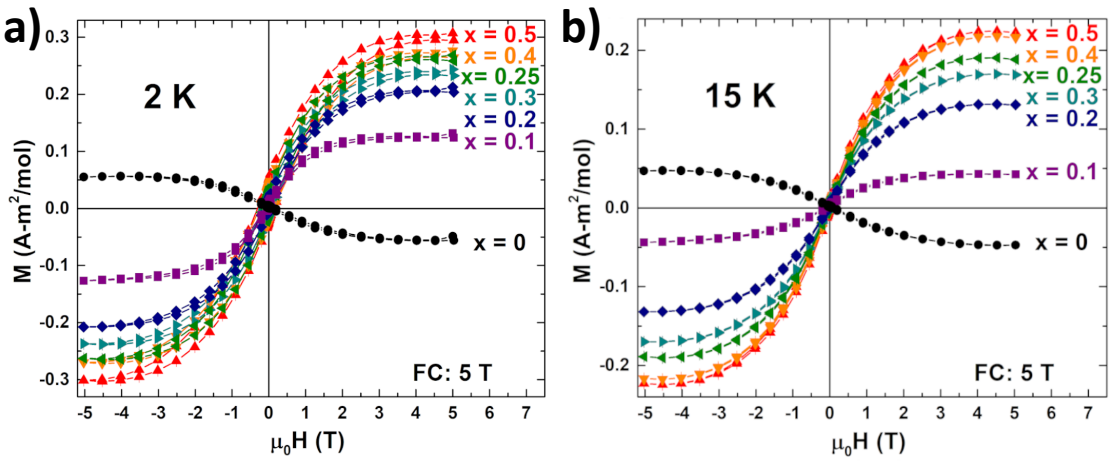

Figure 4.21: Subtracted M vs H loops at a) 2 K and b) 15 K for all samples. Undoped Co_3O_4 shows a characteristic spin-flop that occurs at the surface of the particles, while the Cu doped Co_3O_4 show a large increase in magnetic saturation.

the core, the subtracted M vs μ_0H loops for the Cu doped samples can also present ferro/ferrimagnetic contributions from the core. M_s for all of the Co_3O_4 samples ($x = 0$, and the shapes) show a constant coercivity between 2 - 15 K, while the Cu doped samples show a continual increase with x.

For Co_3O_4, there are stronger antiferromagnetic interactions in the core, with a spin-flop like surface layer that can still display the same ferromagnetic characteristics, such as, coercivity, exchange bias, etc. This is a result of the coupling between the surface layer and the antiferromagnetic core. For the case of the Cu doped samples, the antiferromagnetic interactions are decreasing, and there is evidence of an increase in ferro/ferrimagnetic behaviour at very low temperature ($\leq$ 10 K). Fig. 4.22 a) shows the coercivity (H_c), b) the exchange bias (H_{ex}), and c) shows the magnetic saturation (M_s) for all samples between 2 K and 30 K. It is found that in the region of 10 - 30 K that the coercivity of the Cu doped samples is smaller than the undoped

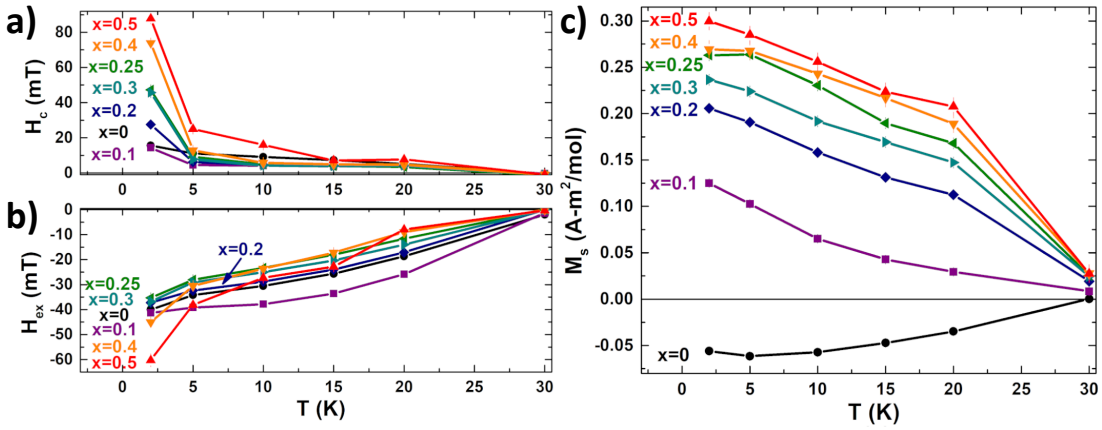

Figure 4.22: a) Coercivity as a function of temperature (H_c) shows a drastic increase below 10 K when Cu is present in the structure. b) Exchange bias (H_{ex}) decreases as doping increases (excluding the $x = 0$ and 0.5 sample). c) Magnetic saturation M_s is shown for each of the samples between 2 - 30 K.

($x = 0$) sample (except for $x = 0.5$ which presents the largest CuO impurity, bulk CuO: $T_N = 230\ K$[97]), but abruptly increases at very low temperatures ($\leq$ 10 K). This indicates the presence of a weak ferromagnetic exchange that orders at low temperatures. The exchange bias, H_{ex}, for all Cu doped samples is smaller than the H_{ex} for the undoped sample (with the exception of $x = 0.1$ and $x = 0.5$). This is a result of the decreased antiferromagnetic interactions throughout the particle which cause a weaker coupling to the surface.

Chapter 5

Exchange at the Surface (Shapes) and in the Core (Doping)

5.1 Introduction

Exchange interactions are able to describe the magnetic order associated with the behaviour of the Co_3O_4 nanoshapes, and $Cu_xCo_{3-x}O_4$ nanoparticles. The complicated nature of the exchange interactions are a result of the non-magnetic Co^{3+} ion that is intermediate in the exchange. The large crystal field associated with Co in the O_h site provides the means for the pairing of spins, violating Hund's rule. At the surface of the nanoparticles changes to the associated crystal fields can induce a small magnetic moment present on low-coordinated Co^{3+} ions.

Through competition of the magnetic interactions at the surface we can explain the differences in magnetic order associated with the shapes. Dominant antiferromagnetic behaviour induces a spinflop in the cube shaped particles, while the extra magnetic moment and related ferromagentic interactions can be linked directly to the exposure

of the (111) plane of the plates[34; 74]. This leads to a description of the magnetism based on the exposed interactions at the surface.

For the $Cu_xCo_{3-x}O_4$ system, the magnetization is dominated by the larger ferrimagnetic behaviour in the core of the particles. The ferrimagnetic behaviour arises from the weak ferromagnetic exchange interactions between Cu^{2+} ions located at the octahedral site and Co^{2+} in the tetrahedral site. This is enabled by the large size of the $Cu^{2+}(O_h)$ ionic radii and the ligand hole arising on the intermediate oxygen ions.

5.2 Implications of the Surface on the Magnetic Properties and Exchange

As described in section 1.4, the superexchange interaction is the dominant mechanism for exchange between the magnetic Co^{2+} ions in Co_3O_4. The more direct interaction of Co^{2+}- O - Co^{2+} accounts for only a small (∼10%) portion of the total exchange strength. The three extended superexchange pathways in the form of Co^{2+}- O - Co^{3+}- O - Co^{2+}, are the reason for the strong magnetic order present in bulk Co_3O_4[20; 44]. Returning to the convention of $\uparrow\downarrow_{180}$, $\uparrow\downarrow_{90}$, and $\uparrow\uparrow_{90}$ for the three different paths shown in Fig. 5.1, the different surface terminations can now be discussed in terms of these exchange pathways.

It was noted in section 1.4 that the competing interactions $\uparrow\downarrow_{90}$ and $\uparrow\uparrow_{90}$ paths have identical bond distances, bond angles, and path multiplicities leading to their cancellation[20; 44]. It is found that the $\uparrow\downarrow_{180}$ is the only uncompensated exchange interaction pathway in bulk Co_3O_4. This is shown in the last column of Table 5.1. At the surface of the particles there can be uncompensated $\uparrow\downarrow_{90}$ and $\uparrow\uparrow_{90}$ interactions

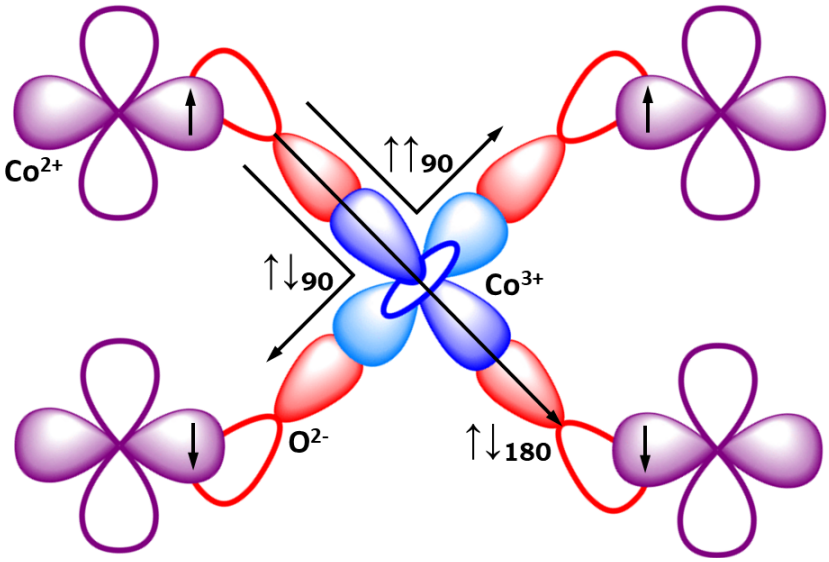

Figure 5.1: Different possible exchange pathways between Co^{2+} ions (purple) through an intervening Co^{3+} ion (blue) and two oxygen ions (red). In the $\uparrow\downarrow_{180}$ Co^{2+} ions are connected through the same d-orbital on Co^{3+} producing an antiferromagnetic interaction. $\uparrow\uparrow_{90}$ and $\uparrow\downarrow_{90}$ are connected through the same d-orbital resulting in one ferromagnetic and one antiferromagnetic interaction, due to the Pauli exclusion principle.

resulting from broken symmetry and imperfect cancellation of the exchange. Thus, we can quantify these uncompensated interactions at the surface using the parameter δ given by:

$$\delta = \frac{1 + M_{\uparrow\uparrow_{90}} - M_{\uparrow\downarrow_{90}}}{M_{\uparrow\downarrow_{180}}} \tag{5.1}$$

where M is the multiplicity of the path given in the subscript. Thus, if there are more ferromagnetic ($\uparrow\uparrow_{90}$) paths then antiferromagnetic ($\uparrow\downarrow_{90}$ and $\uparrow\downarrow_{180}$) paths, $\delta > 1.1$, and ferromagnetic order is predicted at the surface. Likewise, $\delta < 1.1$ indicates that antiferromagnetic order is present at the surface.

Using the multiplicities given in Table 5.1 we find that the cubes have a value of $\delta_{100} = 0.83$. With a value less than $\delta = 1.1$ we find that antiferromagnetic in-

teractions are dominant at the surface of the particles. This in accordance with the previous characterization of the antiferromagnetic spin-flop that occurs at the surface of the Co_3O_4 cubes. The cubes display the smallest value for δ ($\delta_{100} = 0.83$, nearest to bulk $\delta = 1/12$) and it was found they displayed behaviour very close to bulk Co_3O_4 with an exchange constant of $J_{ij} = 3.0$ K$/k_B$. The plates have a much larger value of $\delta_{111} = 2.17$. Re-examining the surface of the (111) plane in Fig. 3.4 b) we find that the zig-zag like structure promotes the ferromagnetic 'W'-shaped exchange interaction ($\uparrow\uparrow_{90}$) resulting in the observed ferromagnetic behaviour at the surface. The increased magnetic moment associated with the (111) plane is a result of the decreased coordination/broken symmetry at the surface of the (111) plane. The low coordination lowers the crystal field associated with d orbital splitting, which allows a small magnetic moment on the Co^{3+} ion.

On the other hand, for the spheres it is necessary to perform an average over the planes at the surface of the spheres, this gives a value of $\delta_{\text{spheres}} = 0.92$. The spheres display similar behaviour to both the cubes and the plates, where below T_N the spheres showed evidence of an antiferromagnetic spin-flop at the surface, as found in the cubes. But display a highly enhanced magnetic moment that was found to be

Table 5.1: Co_3O_4 Surface Exchange Pathways

Multiplicity	(111) Plane	(110) Plane	(100) Plane	Bulk
$\uparrow\downarrow_{180}$	6	7	6	12
$\uparrow\downarrow_{90}$	6	12	12	24
$\uparrow\uparrow_{90}$	18	12	16	24

related to the exposure of the (111) plane at the surface[34; 74].

We have been able to show that competition at the surface can explain the differences in antiferro- and ferromagnetic order shown to originate from the surfaces of the (100) plane of the cubes and the (111) plane of the plates, respectively. The behaviour of the spheres can be addressed by consideration of a combination of planes at the surface including the {100}, {110}, and {111} families of planes. The spheres clearly show intermediate behaviour between the two shapes involving the different exposed planes that occur at the surfaces. Consideration of the surface can also explain the presence of the enhanced magnetic moment of the (111) plane, arising from the usually non-magnetic Co^{3+} ions at the surface. This idea also addresses the weakened antiferromagnetic interactions occurring at the surface of the cubes and spheres, resulting in an antiferromagnetic spin-flop where the spin-flop layer is shown to saturate at much lower fields than required for bulk Co_3O_4[20]. Thus, the idea of surface environments and exchange have provided mechanisms to explain the very fundamental behaviour exhibited by the nanoparticles. Moreover, the idea of surface exchange is shown to be directly responsible for the magnetism observed.

5.3 Role of Ligand Holes on the Magnetism of $Cu_xCo_{3-x}O_4$

Introducing Cu^{2+} in the structure increases the number of possible exchange interactions that can occur leading to a more complicated magnetic structure than Co_3O_4. The usual extended superexchange interactions that occur in Co_3O_4 are still present in Cu doped Co_3O_4, but weakened due to the incorporation of Cu^{2+} into the T_d sites. $Cu^{2+}(T_d)$ causes a decrease in the overall magnetic moment for the doped samples as

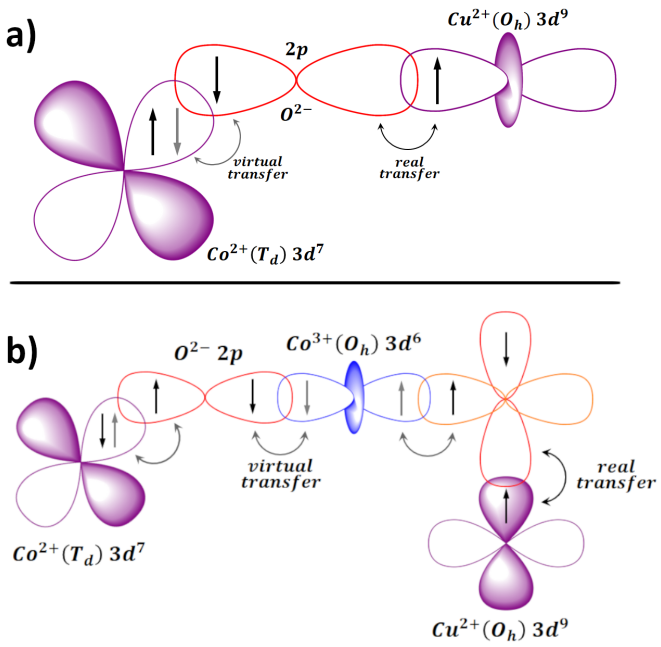

Figure 5.2: a) Ferromagnetic exchange interaction between $Co^{2+}(T_d)$ and $Cu^{2+}(O_h)$ through a single intermediate oxygen ion, resembling a conventional superexchange interaction but involving both real and virtual transfers of electrons. b) An antiferromagnetic extended superexchange interaction between $Co^{2+}(T_d)$ and $Cu^{2+}(O_h)$ occurs through three intermediate ions (as in Co_3O_4).

discussed previously, but the weakened exchange between $Co^{2+}(T_d)$ ions arises from the decreased multiplicity for the extended interactions. This results in the observed decrease in the magnetic ordering (T_N) of the different samples.

Cu^{2+} in the octahedral sites introduces new exchange interactions between magnetic ions in the structure. In part, the Cu-doped structure resembles that of certain superconducting cuprates which contain $Cu^{2+}(O_h)$ forming CuO_2 planes (in the a-b plane) with oxygen that contain ligand holes[94; 95]. A more conventional superexchange-like interaction can occur between $Cu^{2+}(O_h)$ and $Co^{2+}(T_d)$ through a single oxygen ion. This interaction resembles a combination of double exchange, and

superexchange involving a real transfer of an electron from the ligand ($Cu^{3+}(O_h) \rightarrow Cu^{2+}(O_h) + 3d^9\underline{L}$) and virtual transfer of an electron between the O and $Co^{2+}(T_d)$ (Fig. 5.2 a). We know the second part of the interaction does not involve real transfer since no $Co^{3+}(T_d)$ was found through spectroscopy (XAS and XMCD). This interaction is found to be ferromagnetic in nature. In addition to the more conventional exchange interaction we also expect a new extended superexchange interaction that occurs with $Cu^{2+}(O_h)$.

Because $Cu^{2+}(O_h)$ is magnetic it cannot be the intermediary ion for interactions between $Co^{2+}(T_d)$. But, $Cu^{2+}(O_h)$ can be incorporated into the interactions with the form: $Co^{2+}(T_d)$ - O - $Co^{3+}(O_h)$ - O - $Cu^{2+}(O_h)$ (Fig. 5.2 b). Like the extended exchange interactions that occur between $Co^{2+}(T_d)$ ions this interaction is antiferromagnetic. With a tetragonal distortion ($c > a$) it was found that $Cu^{2+}(O_h)$ only has one unpaired electron in the $d_{x^2-y^2}$ orbital, and thus, exchange does not occur through the d_{z^2} orbital in the c direction, minimizing the amount of exchange that Cu can undergo. The competition between the possible ferromagnetic and antiferromagnetic exchange interactions explains the very weak nature of the ferro/ferrimagnetic exchange at low temperatures (<30 K). Doping the structure with Cu allows us to investigate ferromagnetic exchange interactions in the core that result from differences in the structural nature of the cations.

Chapter 6

Conclusions and Future Work

The exchange interactions of cobalt oxide have been investigated through consideration of the surface exchange in Co_3O_4 nanoshapes and Cu doping. The non-magnetic Co^{3+} ion located at the octahedral sites is crucial to the propagation of interactions between magnetic ions in the structure. This leads to a wide range of possible behaviour when considering the interactions directly at the surface, or new interactions that arise from Cu doping.

Understanding the overall magnetic order for the different Co_3O_4 systems comes in large part from understanding of the nature of magnetic interactions that occur in bulk cobalt oxide, e.g. extended superexchange interactions. These extended superexchange interactions have many possible paths between magnetic neighbours due to the intermediate Co^{3+} ion involved in the exchange. When considering the dominant interactions of the Co_3O_4 nanoshapes a crucial step is characterization of the core. For an antiferromagnet this is beautifully identified through the high-field susceptibility with identical behaviour the shapes contain identical magnetism in the cores. Thus

the changes between the shapes can be characterized by direct consideration of the surface terminations. For Cu-doped Co_3O_4 we find new exchange interactions, both of the form of regular superexchange but also new extended superexchange interactions.

The cube shaped particles expose the (100) plane which displays bulk-like structuring that leads to a bulk-like behaviour in the magnetism observed. An antiferromagnetic spin-flop that occurs only at the surface indicates a decrease in the strength of the antiferromagnetic interactions. Where coupling to the stronger antiferromagnetic core results in a coercivity and exchange bias for an overall antiferromagnet. Very different behaviour is found in the hexagonal plates that expose the (111) plane. It is found that low coordination and strong ferromagnetic interactions result in ferromagnetism at the surface of the plates. Positive saturation and much larger coercivities indicate the stronger ferromagnetic interactions. The spheres are shown to be a combination of many different planes, using the {100}, {110}, and {111} families of planes. We have shown that the spheres display characteristics from both the cubes and the plates, displaying an antiferromagnetic spin-flop with inverted hysteresis loops. But, the exposed (111) plane results in a significant increase to the magnetic moment at the surface of the spheres. To characterize the exchange interactions at the surface of the shapes, a parameter delta was used, which illustrates the dominant exchange interactions, conforming to the results observed in the magnetism.

In $Cu_xCo_{3-x}O_4$, the new extended superexchange interactions are antiferromagnetic while the regular superexchange interactions that occur through a single oxygen ion are ferromagnetic. This leads to competition, and a weakening of the ferromagnetic order for the Cu ions. Through the Jahn-Teller effect, a tetragonal distortion

causes a break in the degeneracies for the magnetically active $Cu^{2+}(O_h)$ ion. Exchange then only occurs through the $a-b$ planes of the O_h ions. While $Cu^{2+}(T_d)$ is shown to be nearly paramagnetic, i.e the drop in T_N roughly coincides with Cu entering the T_d site. $Cu^{2+}(T_d)$ has a much smaller ionic radii than $Cu^{2+}(O_h)$ leading to much weaker exchange between $Cu^{2+}(T_d)$ and $Co^{2+}(T_d)$ ions.

Compositional and site-specific characterization undertaken using XAS was vital in obtaining information about the Cu ions. EXAFS provided a way to ensure that Cu indeed occupies both O_h and T_d sites. With the ability to see the contributions from each site directly, this provides a robust starting point to the characterization of the Cu L-edge XAS leading to the identification of the magnetic interactions through $Cu^{2+}(O_h)$ ions. The Cu^{2+} ions at octahedral sites in the structure $Cu_xCo_3O_4$ forms an analogous structure to that of the hole doped cuprates which form the basis for high temperature superconductivity. The holes that form in the Cu-O structure provide a way for exchange interactions to propagate, while between two $Cu^{2+}(O_h)$ ions, a charge transfer effect may occur leading to the higher conduction of the parent compounds of the hole doped cuprates.

The fundamental nature of the characterization performed on the Co_3O_4 shapes shows the importance of the surface when considering the overall magnetism of nanoparticles and allows us to explore the idea of ferromagnetic surface layers in a nominally antiferromagnetic compound. Cu-doped Co_3O_4 shows the importance of Co^{3+} in propagating the antiferromagnetic interactions in Co_3O_4, and further allows us to investigate dominant ferromagnetic interactions in the core of the particles. This is revealed by the ferrimagnetic behaviour as Cu enters the particle.

The logical next step is to further dope Co_3O_4 and $Cu_xCo_3O_4$ with other first row transition metal ions such as Mn and Zn. Additionally, synthesizing more shapes of Co_3O_4 to further investigate the properties of the exposed surface terminations of for nanoparticles. Synthesizing shapes such as rods, octopods, and triangles would enable one to test the limits of the model developed in regard to the exchange interactions occurring at the surface. Likewise, adding ions such as Mn into the structure should provide major changes to the overall electronic and magnetic structure. An attempt to create an inverted spinel structure of Co_3O_4 is of interest, as it seems the structure is opposed to forming a structure with charge transfer on the Co ions. The filled t_{2g} orbitals of the Co^{3+} ion may provide a much more stable and energetically favourable configuration rather than form Co^{2+} in the octahedral sites. Once again, by applying both spectroscopy techniques and overall magnetic characterizations we can gain a great understanding of the overall structure and magnetic interactions.

Bibliography

[1] M. McElfresh. *Fundamentals Magnetism and Magnetic Measurements Featuring Quantum Design's Magnetic Property Measurement System.* Quantum Design, 2010.

[2] Lin, Feng and Nordlund, Dennis and Pan, Taijun and Markus, Isaac M. and Weng, Tsu-Chien and Xin, Huolin L. and Doeff, Marca M. Influence of synthesis conditions on the surface passivation and electrochemical behavior of layered cathode materials. *J. Mater. Chem. A*, 2:19833–19840, 2014.

[3] E. Stavitski and F. M. F. de Groot. The CTM4XAS program for EELS and XAS spectral shape analysis of transition metal L edges. *Micron*, 41(7):687—694, October 2010.

[4] Y. Ichiyanagi and S. Yamada. The size-dependent magnetic properties of Co_3O_4 nanoparticles. *Polyhedron*, 24(16):2813 – 2816, 2005. Proceedings of the 9th International Conference on Molecule-based Magnets (ICMM 2004).

[5] D. Tobia, E. Winkler, R. D. Zysler, M. Granada, and H. E. Troiani. Size dependence of the magnetic properties of antiferromagnetic Cr_2O_3 nanoparticles. *Phys. Rev. B*, 78:104412, Sep 2008.

[6] D. Patil, P. Patil, V. Subramanian, P. A. Joy, and H. S. Potdar. Highly Sensitive and Fast Responding CO Sensor Based on Co_3O_4 Nanorods. *Talanta*, 81(1):37 – 43, 2010.

[7] J. Xu and J. Cheng. The Advances of Co_3O_4 as Gas Sensing Materials: A Review. *Journal of Alloys and Compounds*, 686(Supplement C):753 – 768, 2016.

[8] D. Su, S. Dou, and G. Wang. Single Crystalline Co_3O_4 Nanocrystals Exposed with Different Crystal Planes for LiO_2 Batteries. *Scientific reports*, 4:5767, 08 2014.

[9] D. Su, X. Xie, P. Munroe, S. Dou, and G. Wang. Mesoporous hexagonal Co_3O_4 for high performance lithium ion batteries. *Scientific reports*, 4:6519, 10 2014.

[10] F. Liu, B. Zhang, H. Su, H. Zhang, L. Zhang, and W. Yang. Controllable synthesis of self-assembly Co_3O_4 nanoflake microspheres for electrochemical performance. *Nanotechnology*, 27(35):355603, 2016.

[11] T. Tatarchuk, B. Al-Najar, M. Bououdina, and M. A. A. Ahmed. *Catalytic and Photocatalytic Properties of Oxide Spinels*, pages 1–50. Springer International Publishing, Cham, 2018. ISBN 978-3-319-48281-1.

[12] F. Kapteijn, J. Rodriguez-Mirasol, and J. A. Moulijn. Heterogeneous catalytic decomposition of nitrous oxide. *Applied Catalysis B: Environmental*, 9(1):25 – 64, 1996.

[13] R. Jing, A. Shan, R. Wang, and C. Chen. Phase Formations, Magnetic and

Catalytic Properties of Co_3O_4 Hexagonal Micro-Boxes with One-Dimensional Nanotubes. *CrystEngComm*, 15:3587–3592, 2013.

[14] G. Dionne. *Magnetic Oxides*. Springer, 01 2009.

[15] S. Blundell. *Magnetism in Condensed Matter*. Oxford Master Series in Condensed Matter Physics. OUP Oxford, 2001. ISBN 9780198505914.

[16] J. Van Vleck. *The Theory of Electric and Magnetic Susceptibilities*. International series of monographs on physics. Oxford University Press, 1965.

[17] P. Cossee. Magnetic properties of cobalt in oxide lattices. *J. Inorg. Nucl. Chem.*, 8:483 – 488, 1958. Proceedings International Symposium on the Chemistry of the Co-ordination Compounds.

[18] U. Guelph. Paramagnetism. http://www.chemistry.uoguelph.ca/educmat/chm710/files/5_3_Paramagnetism.pdf. [Online, accessed 01-June-2020].

[19] M. Scheffler, A. Tkatchenko, and P. Rinke. Theoretical material science. 2012.

[20] W. Roth. The Magnetic Structure of Co_3O_4. *J. Phys. Chem. Solids*, 25(1):1 – 10, 1964.

[21] W. Heitler and F. London. Wechselwirkung neutraler Atome und homöopolare Bindung nach der Quantenmechanik. *Zeitschrift für Physik*, 44(6-7):455–472, 1927.

[22] H. Kramers. L'interaction Entre les Atomes Magnétogènes dans un Cristal Paramagnétique. *Physica*, 1(1):182 – 192, 1934.

[23] P. W. Anderson. Antiferromagnetism. Theory of Superexchange Interaction. *Phys. Rev.*, 79:350–356, Jul 1950.

[24] P. W. Anderson. New Approach to the Theory of Superexchange Interactions. *Phys. Rev.*, 115:2–13, Jul 1959.

[25] J. B. Goodenough and A. L. Loeb. Theory of Ionic Ordering, Crystal Distortion, and Magnetic Exchange Due to Covalent Forces in Spinels. *Phys. Rev.*, 98: 391–408, Apr 1955.

[26] J. B. Goodenough. Theory of the Role of Covalence in the Perovskite-Type Manganites $[\mathrm{La}, M(\mathrm{II})]\mathrm{MnO}_3$. *Phys. Rev.*, 100:564–573, Oct 1955.

[27] J. Kanamori. Superexchange interaction and symmetry properties of electron orbitals. *J. Phys. Chem. Solids*, 10(2):87 – 98, 1959.

[28] J. Hubbard. Electron correlations in narrow energy bands. *Proc. R. Soc. London, Ser. A*, 276(1365):238–257, 1963.

[29] J. Stöhr and H. Siegmann. *Magnetism: From Fundamentals to Nanoscale Dynamics*. Springer Series in Solid-State Sciences. Springer, 2006. ISBN 9783540302827.

[30] C. Zener. Interaction between the d-Shells in the Transition Metals. II. Ferromagnetic Compounds of Manganese with Perovskite Structure. *Physical Review*, 82(3):403–405, May 1951.

[31] S. I. Popkov, A. A. Krasikov, A. A. Dubrovskiy, M. N. Volochaev, V. L. Kirillov, O. N. Martyanov, and D. A. Balaev. Size effects in the formation of an

uncompensated ferromagnetic moment in NiO nanoparticles. *Journal of Applied Physics*, 126(10):103904, 2019.

[32] M. A. Ballem, M. M. Blaow, and F. Söderlind. Magnetic Behavior of Size-Controlled Co_3O_4 Nanoparticles Synthesized in the Pores of Functionalized Silica. *IJEIT*, 1(1), 2014.

[33] Y. A. Koksharov. *Magnetism of Nanoparticles: Effects of Size, Shape, and Interactions*, pages 197–254. Wiley-VCH Verlag GmbH & Co., 2009. ISBN 9783527627561.

[34] J. M. D. Coey. *Magnetism and Magnetic Materials*. Cambridge University Press, 2010.

[35] M. E. Smith. Book Review of Magnetism and magnetic resonance in solids, A. P. Guimaraes. *Magnetic Resonance in Chemistry*, 39(1):53–54, 2001.

[36] W. F. Brown Jr. THE FUNDAMENTAL THEOREM OF THE THEORY OF FINE FERROMAGNETIC PARTICLES*. *Annals of the New York Academy of Sciences*, 147(12):463–488, 1969.

[37] E. C. Stoner and E. P. Wohlfarth. A mechanism of magnetic hysteresis in heterogeneous alloys. *Philosophical Transactions of the Royal Society of London. Series A, Mathematical and Physical Sciences*, 240(826):599–642, 1948.

[38] W. H. Meiklejohn and C. P. Bean. New Magnetic Anisotropy. *Phys. Rev.*, 102: 1413–1414, Jun 1956.

[39] J. Nogués and I. K. Schuller. Exchange bias. *Journal of Magnetism and Magnetic Materials*, 192(2):203 – 232, 1999.

[40] Ò. Iglesias, X. Batlle, and A. Labarta. Modelling exchange bias in core/shell nanoparticles. *Journal of Physics: Condensed Matter*, 19(40):406232, sep 2007.

[41] S. Chandra, H. Khurshid, M.-H. Phan, and H. Srikanth. Asymmetric hysteresis loops and its dependence on magnetic anisotropy in exchange biased Co/CoO core-shell nanoparticles. *Applied Physics Letters*, 101(23):232405, 2012.

[42] X.-H. Wei, R. Skomski, Z.-G. Sun, and D. J. Sellmyer. Proteresis in Co:CoO core-shell nanoclusters. *Journal of Applied Physics*, 103(7):07D514, 2008.

[43] X. Z. Li, X. H. Wei, R. Skomski, and D. J. Sellmyer. Structure and magnetism of Co:CoO core–shell nanoclusters. *Journal of Nanoparticle Research*, 12(3): 789–794, Mar 2010.

[44] W. Roth. Magnetic Properties of Normal Spinels with only A-A Interactions. *J. Phys. France*, 1964.

[45] V. F. Puntes, K. M. Krishnan, and A. P. Alivisatos. Colloidal Nanocrystal Shape and Size Control: The Case of Cobalt. *Science*, 291(5511):2115–2117, 2001.

[46] S. Rani, Y. Sharma, and G. D. Varma. Mixed magnetic phases in Co_3O_4 nanoparticles synthesized by co-precipitation method. *AIP Conference Proceedings*, 1591 (1):526–528, 2014.

[47] Y. Chen, J. Zhou, D. Mullarkey, R. O'Connell, W. Schmitt, D. M. Venkatesan,

M. Coey, and H. Zhang. Synthesis, characterization and magnetic properties of ultrafine Co_3O_4 octahedra. *AIP Advances*, 5:087122, 08 2015.

[48] R. Ma, Z. Liu, K. Takada, K. Fukuda, Y. Ebina, Y. Bando, and T. Sasaki. Tetrahedral Co(II) Coordination in α-Type Cobalt Hydroxide: Rietveld Refinement and X-ray Absorption Spectroscopy. *Inorg. Chem.*, 45(10):3964–3969, 2006.

[49] Deng, T. et al. Atomic-level energy storage mechanism of cobalt hydroxide electrode for pseudocapacitors. *Nat. Commun.*, 8(15194), (2017).

[50] Z. Huang, Y. Zhao, Y. Song, Y. Li, G. Wu, H. Tang, and J. Zhao. Study on the oxidation process of cobalt hydroxide to cobalt oxides at low temperatures. *RSC Adv.*, 6:80059–80064, 2016.

[51] P. Scherrer. Bestimmung der Größe und der inneren Struktur von Kolloidteilchen mittels Röntgenstrahlen. *Nachrichten von der Gesellschaft der Wissenschaften zu Göttingen, Mathematisch-Physikalische Klasse*, 1918:98–100, 1918.

[52] A. L. Patterson. The Scherrer Formula for X-Ray Particle Size Determination. *Phys. Rev.*, 56:978–982, Nov 1939.

[53] C. F. Holder and R. E. Schaak. Tutorial on Powder X-ray Diffraction for Characterizing Nanoscale Materials. *ACS Nano*, 13(7):7359–7365, 2019. PMID: 31336433.

[54] R. Egerton. *Physical Principles of Electron Microscopy: An Introduction to TEM, SEM, and AEM.* Springer International Publishing, 2016. ISBN 9783319398778.

[55] C. T. Rueden, J. Schindelin, M. C. Hiner, B. E. DeZonia, A. E. Walter, E. T. Arena, and K. W. Eliceiri. ImageJ2: ImageJ for the next generation of scientific image data. *arXiv e-prints*, January 2017.

[56] F. de Groot and A. Kotani. *Core Level Spectroscopy of Solids*. Advances in Condensed Matter Science. CRC Press, 2008. ISBN 9781420008425.

[57] F. Hippert, E. Geissler, J. Hodeau, E. Lelièvre-Berna, and J. Regnard. *Neutron and X-ray Spectroscopy*. Grenoble sciences. Springer Netherlands, 2006. ISBN 9781402033377.

[58] F. M. F. de Groot, M. Grioni, J. C. Fuggle, J. Ghijsen, G. A. Sawatzky, and H. Petersen. Oxygen 1s x-ray-absorption edges of transition-metal oxides. *Phys. Rev. B*, 40:5715–5723, Sep 1989.

[59] C. H. M. van Oversteeg, H. Q. Doan, F. M. F. de Groot, and T. Cuk. In situ X-ray absorption spectroscopy of transition metal based water oxidation catalysts. *Chem. Soc. Rev.*, 46:102–125, 2017.

[60] B. Ravel and M. Newville. ATHENA, ARTEMIS, HEPHAESTUS: data analysis for X-ray absorption spectroscopy using IFEFFIT. *Journal of Synchrotron Radiation*, 12(4):537–541, 2005.

[61] J. J. Rehr and R. C. Albers. Theoretical approaches to x-ray absorption fine structure. *Rev. Mod. Phys.*, 72:621–654, Jul 2000.

[62] A. Morello, W. Angenent, G. Frossati, and L. J. Jongh. Automated and versatile

SQUID magnetometer for the measurement of materials properties at millikelvin temperatures. *The Review of scientific instruments*, 76:023902, 01 2005.

[63] K. Tsukiyama, M. Takasaki, Y. Oaki, and H. Imai. Evolution of Co_3O_4 Nanocubes through Stepwise Oriented Attachment. *Langmuir*, 35(24):8025–8030, 2019. PMID: 31145617.

[64] Yu, X.Y. et al. Facet-dependent electrochemical properties of Co_3O_4 nanocrystals toward heavy metal ions. *Sci. Rep.*, 3(2886), 2013.

[65] H. Sun, H. M. Ang, M. O. Tadé, and S. Wang. Co_3O_4 nanocrystals with predominantly exposed facets: synthesis, environmental and energy applications. *J. Mater. Chem. A*, 1:14427–14442, 2013.

[66] B. H. Toby and R. B. Von Dreele. GSAS-II: the genesis of a modern open-source all purpose crystallography software package. *Journal of Applied Crystallography*, 46(2):544–549, 2013.

[67] K. Momma and F. Izumi. VESTA: a three-dimensional visualization system for electronic and structural analysis. *Journal of Applied Crystallography*, 41(3): 653–658, 2008.

[68] F. Morales, F. M. F. de Groot, P. Glatzel, E. Kleimenov, H. Bluhm, M. Hävecker, A. Knop-Gericke, and B. M. Weckhuysen. In Situ X-ray Absorption of Co/Mn/TiO_2 Catalysts for Fischer-Tropsch Synthesis. *The Journal of Physical Chemistry B*, 108(41):16201–16207, 2004.

[69] R. Nakajima, J. Stöhr, and Y. U. Idzerda. Electron-yield saturation effects in

L-edge x-ray magnetic circular dichroism spectra of Fe, Co, and Ni. *Phys. Rev. B*, 59:6421–6429, Mar 1999.

[70] P. Dutta, M. S. Seehra, S. Thota, and J. Kumar. A comparative study of the magnetic properties of bulk and nanocrystalline Co_3O_4. *Journal of Physics: Condensed Matter*, 20(1):015218, dec 2007.

[71] O. Madelung, U. Rössler, and M. Schulz. Co_3O_4: magnetic properties: Datasheet from Landolt-Börnstein - Group III Condensed Matter · Volume 41D: "Non-Tetrahedrally Bonded Binary Compounds II", .

[72] S. A. Makhlouf. Magnetic properties of Co_3O_4 nanoparticles. *Journal of Magnetism and Magnetic Materials*, 246(1):184 – 190, 2002.

[73] T. Ueno, J. Sinha, N. Inami, Y. Takeichi, S. Mitani, K. Ono, and M. Hayashi. Enhanced orbital magnetic moments in magnetic heterostructures with interface perpendicular magnetic anisotropy. *Scientific Reports*, 5:14858, 10 2015.

[74] J. Chen and A. Selloni. Electronic states and magnetic structure at the Co_3O_4 (110) surface: A first-principles study. *Phys. Rev. B*, 85:085306, Feb 2012.

[75] H. Zhu, J. Luo, J. Liang, G. Rao, J. Li, J. Zhang, and Z. Du. Synthesis and magnetic properties of antiferromagnetic Co_3O_4 nanoparticles. *Physica B: Condens Matter*, 403(18):3141 – 3145, 2008.

[76] C. Díaz, M. L. Valenzuela, M. A. Laguna-Bercero, A. Orera, D. Bobadilla, S. Abarca, and O. Peña. Synthesis and magnetic properties of nanostruc-

tured metallic Co, Mn and Ni oxide materials obtained from solid-state metal-macromolecular complex precursors. *RSC Adv.*, 7:27729–27736, 2017.

[77] G. Wang, X. Shen, J. Horvat, B. Wang, H. Liu, D. Wexler, and J. Yao. Hydrothermal Synthesis and Optical, Magnetic, and Supercapacitance Properties of Nanoporous Cobalt Oxide Nanorods. *J. Phys. Chem. C*, 113(11):4357–4361, 2009.

[78] D. Li, Z. Han, J. G. Zheng, X. L. Wang, D. Y. Geng, J. Li, and Z. D. Zhang. Spin canting and spin-flop transition in antiferromagnetic Cr_2O_3 nanocrystals. *J. Appl. Phys.*, 106(5):053913, 2009.

[79] I. M. DiMucci, J. T. Lukens, S. Chatterjee, K. M. Carsch, C. J. Titus, S. J. Lee, D. Nordlund, T. A. Betley, S. N. MacMillan, and K. M. Lancaster. The Myth of d8 Copper(III). *Journal of the American Chemical Society*, 141(46): 18508–18520, 2019. PMID: 31710466.

[80] G. Sawatzky and R. Green. *Quantum Materials: Experiments and Theory*. Autumn School on Correlated Electrons, 09 2016. ISBN 978-3-95806-159-0.

[81] J. A. Yarmoff, D. R. Clarke, W. Drube, U. O. Karlsson, A. Taleb-Ibrahimi, and F. J. Himpsel. Valence electronic structure of $Y_1Ba_2Cu_3O_7$. *Phys. Rev. B*, 36: 3967–3970, Sep 1987.

[82] N. Nücker, J. Fink, J. C. Fuggle, P. J. Durham, and W. M. Temmerman. Evidence for holes on oxygen sites in the high-T_c superconductors $La_{2-x}Sr_xCuO_4$ and $YBa_2Cu_3O_{7-y}$. *Phys. Rev. B*, 37:5158–5163, Apr 1988.

[83] C. T. Chen, F. Sette, Y. Ma, M. S. Hybertsen, E. B. Stechel, W. M. C. Foulkes, M. Schulter, S.-W. Cheong, A. S. Cooper, L. W. Rupp, B. Batlogg, Y. L. Soo, Z. H. Ming, A. Krol, and Y. H. Kao. Electronic states in $La_{2-x}Sr_xCuO_{4+\delta}$ probed by soft-x-ray absorption. *Phys. Rev. Lett.*, 66:104–107, Jan 1991.

[84] J. Rodríguez-Carvajal. Recent advances in magnetic structure determination by neutron powder diffraction. *Physica B: Condensed Matter*, 192(1):55 – 69, 1993.

[85] Y. Raydugin, V. Naish, and E. Turov. On the magnetic structure of cupric oxide (CuO): 1. The antiferromagnetism in the low-temperature phase. *Journal of Magnetism and Magnetic Materials*, 102(3):331 – 338, 1991.

[86] K. Krezhov, K. Petrov, and T. Karamaneva. Neutron diffraction study on the spinel cu0.72co2.28o4. *Journal of Solid State Chemistry*, 48(1):33 – 39, 1983.

[87] M. L. Baker, M. W. Mara, J. J. Yan, K. O. Hodgson, B. Hedman, and E. I. Solomon. K- and L-edge X-ray absorption spectroscopy (XAS) and resonant inelastic X-ray scattering (RIXS) determination of differential orbital covalency (DOC) of transition metal sites. *Coordination Chemistry Reviews*, 345:182 – 208, 2017.

[88] A. Bergmann, E. Martinez-Moreno, D. Teschner, P. Chernev, M. Gliech, J. F. De Araújo, T. Reier, H. Dau, and P. Strasser. Reversible amorphization and the catalytically active state of crystalline Co_3O_4 during oxygen evolution. *Nature communications*, 6:8625, 2015.

[89] D. C. Bock, C. J. Pelliccione, W. Zhang, J. Timoshenko, K. W. Knehr, A. C.

West, F. Wang, Y. Li, A. I. Frenkel, E. S. Takeuchi, K. J. Takeuchi, and A. C. Marschilok. Size dependent behavior of Fe_3O_4 crystals during electrochemical (de)lithiation: an in situ X-ray diffraction, ex situ X-ray absorption spectroscopy, transmission electron microscopy and theoretical investigation. *Phys. Chem. Chem. Phys.*, 19:20867–20880, 2017.

[90] P. Zhang, L. Li, and D. Nordlund et al. Dendritic core-shell nickel-iron-copper metal/metal oxide electrode for efficient electrocatalytic water oxidation. *Nat Commun*, 9, 2018.

[91] A. Sharma, M. Varshney, J. Park, T.-K. Ha, K.-H. Chae, and H.-J. Shin. XANES, EXAFS and photocatalytic investigations on copper oxide nanoparticles and nanocomposites. *RSC Adv.*, 5:21762–21771, 2015.

[92] P. Jiang, D. Prendergast, F. Borondics, S. Porsgaard, L. Giovanetti, E. Pach, J. Newberg, H. Bluhm, F. Besenbacher, and M. Salmeron. Experimental and theoretical investigation of the electronic structure of Cu_2O and CuO thin films on Cu(110) using x-ray photoelectron and absorption spectroscopy. *The Journal of Chemical Physics*, 138(2):024704, 2013.

[93] C. Prajapat, S. Singh, and D. e. a. Bhattacharya. Proximity effects across oxide-interfaces of superconductor-insulator-ferromagnet hybrid heterostructure. *Sci Rep*, 8, 2018.

[94] D. Meyers, S. Mukherjee, J.-G. Cheng, S. Middey, J.-S. Zhou, J. Goodenough, B. Gray, J. Freeland, T. Saha-Dasgupta, and J. Chakhalian. Zhang-Rice physics

and anomalous copper states in A-site ordered perovskites. *Scientific reports*, 3: 1834, 05 2013.

[95] M. Magnuson, T. Schmitt, V. N. Strocov, J. Schlappa, A. S. Kalabukhov, and L. C. Duda. Self-doping processes between planes and chains in the metal-to-superconductor transition of $YBa_2Cu_3O_{6.9}$. *Scientific reports*, 3:7017, Nov. 2014.

[96] K. Shimizu, H. Maeshima, H. Yoshida, A. Satsuma, and T. Hattori. Deconvolution Analysis of Cu L-edge XANES for Quantification of Copper (II) Coordinations in Copper-aluminate Catalysts. *Japanese Journal of Applied Physics*, 38 (S1):44, jan 1999.

[97] O. Madelung, U. Rössler, and M. Schulz. Cupric oxide (CuO) magnetic properties, heat capacity, density: Datasheet from Landolt-Börnstein - Group III Condensed Matter · Volume 41C: "Non-Tetrahedrally Bonded Elements and Binary Compounds I" in springermaterials (https://doi.org/10.1007/10681727_55), .